Computational Characterization of Drag Reduction for Platooning Heavy Vehicles

by

Andrew Watts

A thesis submitted to the Graduate Faculty of
Auburn University
in partial fulfillment of the
requirements for the Degree of
Master of Science

Auburn, Alabama
May 10, 2015

Keywords: Aerodynamics, Heavy Vehicle, Drag Reduction, Fuel Savings, Platooning, Trucking

Approved by

Joseph Majdalani, Chair, Professor of Aerospace Engineering
Joshua Batterson, Assisstant Research Professor
David Bevly, Professor of Mechanical Engineering

Abstract

This study uses Computational Fluid Dynamics to analyze the aerodynamic properties of multiple heavy vehicle groups in leader-follower configurations, referred to as platoons. The primary metric of interest is the resistive aerodynamic force experienced in the freestream direction, commonly known as drag. The computational model first was validated using a simplified car body for both single and multiple body simulations. After validation, three platooning topics were examined: two vehicle platoons, three vehicle platoons, and multiple geometry two vehicle platoons. It was discovered that at close distances the follower vehicle interferes with the formation of the leader vehicle wake, offering significant drag reduction for both vehicles. At larger distances, it was found that the follower vehicle experiences near constant benefit until the end of the lead vehicle slipstream, at which point the drag rapidly transitions to the single vehicle value. Upon analysis of three vehicle platoons, it was observed that the interior vehicle drag could be reduced below that of the outer vehicles at small spacings and thus larger platoons can offer more benefit per vehicle than their smaller counterparts. Upon investigation of platoons with multiple geometries, it was discovered that placing the least aerodynamic vehicle follow position offers the most potential for overall platoon drag reduction.

Acknowledgments

The author would like to thank Dr. Joshua Batterson for the many hours given in assistance towards the completion of this research.

Table of Contents

List of Figures

List of Tables

Chapter 1

Introduction

This chapter provides an introduction to the problem of heavy vehicle platooning and aerodynamic modeling. Platooning, also known as drafting or slipstreaming, is when a group of two or more vehicles group into a leader-follower formation. The objective of platooning, in a highway environment, is primarily to reduce the overall drag and consume less fuel than if the vehicles were traveling individually. Aspects such as motivation and background are presented and discussed to shed light on this problem. Existing literature and an overview of the current work being performed are also provided for a context of the history (or lack thereof) and the modern state of tractor-trailer platoons on the highway.

1.1 Motivation

In 2012, spending in the logistics and transportation industry in the United States totaled \$1.33 trillion and accounted for 8.5 percent of the annual gross domestic product. Within this industry, the American Trucking Association reports that trucking accounted for 68.5 percent of domestic freight tonnage moved and generated \$642 billion of revenue [1]. Because of the expansiveness and competitive nature of the trucking industry, fleet owners are constantly looking for ways to decrease operating cost, improve profit, and expand their businesses.

One of the most effective cost savings methods is improvement in fuel economy. Therefore, trucking companies continually invest in technologies that reduce fuel usage. The focus on improved gas mileage extends beyond the trucking industry, to the global economy as a whole. Recently, reduced fuel usage has received additional attention as a result from a variety of factors and developments. Stricter carbon emission regulations, such as those imposed by the Department of Transportation (DOT) and Environmental Protection Agency (EPA) [2], and improved understanding of vehicle aerodynamics (via use of simulation tools such as Computational Fluid Dynamics) are just two examples of the factors that have increased the focus on improved fuel economy.

Fuel economy is an extremely important metric in trucking for several reasons. Firstly, fuel consumption by and large accounts for the largest non-employee expense per mile of a heavy vehicle [3]. Secondly, fuel cost is what is known as a variable cost in that the cost associated with fuel used increases with miles driven: more miles driven equates to more fuel consumed. Lastly, because crude oil is a finite commodity and the market is highly variable, the cost of diesel fuel is often uncertain and continually rising. All of these factors strongly affect goods transportation companies' financial bottom line, but are unfortunately beyond their control. Thus the only options for many companies is to increase consumer costs to absorb variance or improve the number of miles a loaded truck can go on a single gallon.

Consider for example, an average truck driver in the United States. A typical driver travels between 2,000 – 3,000 miles per week, based on the 70 hour per 8 days maximum imposed by the Federal Motor Carrier Safety Administration [4]. This represents an average of approximately 130,000 miles driven per truck per year. The typical miles per gallon, or mpg, of a loaded Class 8 truck is between 4 and 7.5 [5]. According to the U.S. Energy Information Administration, the average price of diesel in the U.S. for 2013 was $3.96 U.S. Dollars (USD) per gallon. Assuming a slightly better than average fuel economy of 6.5 mpg and rounding to $4.00 USD/gallon, this equates to $80,000 of fuel expenses per year, per truck. Applying just a 0.5 mpg increase, or 7.5%, reduces costs by nearly $6,000 per year. If these fuel savings are then applied across an entire fleet, the cost reduction per truck quickly turns into significant cost savings for the company. For example, if the FedEx Corp. fleet of just over 25,000 tractors [6] increased the fuel economy of every tractor by only one percent, the cost savings would be nearly $20 million USD per year.

There are five categories that contribute to inefficient fuel use: aerodynamic drag, power train losses, grade changes, rolling resistance, and accessory losses (such as electrical systems). Of these, the main contributors determining the required horsepower are drag and rolling resistance. The resistive force generated by these factors scales with velocity, thus at higher speeds, more fuel is consumed. Rolling resistance scales at a much slower pace than drag force, which is proportional to velocity squared, meaning that at higher speeds the drag force rapidly outpaces the rolling resistance. Due to this, aerodynamic drag accounts for 65-70% of the fuel consumed by a tractor-trailer at highway speeds [7].

Because aerodynamic forces are the major contributor to fuel consumption, reduction of drag is extremely important to the highway-based shipping industry. By reducing the drag, a tractor-trailer experiences immediate fuel savings, which in turn translates directly to cost savings. The drag force is proportional not only to the vehicle speed, but also to the coefficient of drag, which is determined by physical vehicle properties, such as profile. A modified vehicle shape, such as a more streamlined tractor silhouette, can easily result in decreased drag. Because the aerodynamics of a vehicle have such a large influence on fuel consumption, investments in even slight drag reductions can generate measureable and significant cost savings.

The efforts of the trucking industry in recent years to produce larger profit margins through drag reduction can be seen on highways across the United States. From small modifications such as aerotails [8] and trailer side skirts to larger undertakings, such as complete redesigns of newer tractor models with more aerodynamic profiles, the industry, as a whole, has shown a concerted interest in the production of transportation systems that provide reduced drag force and fuel savings.

One low-cost and effective method of drag reduction that has not been formally utilized is vehicle drafting. Drafting, sometimes referred to as slipstreaming, is when a vehicle (or other moving object) aligns itself behind another vehicle to exploit the aerodynamic disturbance, or slipstream, created. The flow field behind the front vehicle is disrupted, being effectively “broken up,” thus providing significantly less air resistance for the follower vehicle. When discussed in terms of fluid dynamics, this results in a lower effective overall free stream velocity for the second vehicle.

Because drag force is proportional to the air speed squared, the consequence of the lower effective air speed is a reduced drag force for the second vehicle. A second, additional benefit that develops when the follower is very close to the leader vehicle is wake interference. This phenomenon is a higher order effect and occurs because the presence of the second vehicle prevents the characteristic wake from fully developing behind the lead vehicle. This interference acts to reduce the wake drag on the front vehicle, which reduces the overall drag force experienced by the leader. Thus it is possible for not only the trailing vehicle to experience improved fuel economy, but also for the lead vehicle to see enhanced gas mileage.

The benefits of drafting are well known and are often utilized in real world scenarios. Professional cyclists, for example, often use drafting to reduce the amount of energy they must expend during races. NASCAR drivers also utilize drafting to obtain greater speeds and better fuel economy during races, even migrating geese flying in a “V” formation are utilizing drafting to enable the flock to fly greater distances without rest.

Unfortunately, the advantages offered by drafting groups of heavy vehicles, or platooning, have not been exploited in highway environments in the past due to human limitations. Factors such as reaction time and severely limited visibility greatly affect the ability of a driver to safely follow another vehicle at a close distance. This is doubly true for tractor-trailers where braking distance and visibility are even more prohibitive. Additionally, many U.S. states have laws against close following, known colloquially as “tailgating,” precisely due to these dangers. Because driver safety is a paramount concern and greatly outweighs any gas mileage improvement, truck platooning has not been a viable cost saving option.

Considering driver reaction time for instance, the average time for a truck driver to respond to a sudden change in road conditions is 1.28 seconds (s) to release the throttle and an additional second to full brake depression [9]. In 1.28 seconds, a vehicle travelling at 70 miles per hour (mph) would travel approximately 130 feet (ft). This is before the brake has even been applied. One hundred and thirty feet is almost the length of two full length semi-trucks (approximately 70ft), a frighteningly large distance before the vehicle even begins to slow. Compound this with the fact that heavy vehicles can weigh up to 80000 pounds, [10] and stopping distances for fully loaded heavy vehicles can quickly become 400-500 ft. At 500 ft, the fuel savings are greatly reduced since the slipstream from the lead vehicle has diminished notably. Under these typical highway circumstances, even assuming optimal conditions, platooning driver-operated vehicles at safe distances likely has no significant benefit.

1.2 Current Work

Recent technological advancements in vehicle automation have removed the obstacle of human psychological boundaries. The Cooperative Adaptive Cruise Control (CACC) system being developed by Auburn University [11] allows a tractor-trailer to safely tail a lead vehicle at a very small separation distance. CACC partially automates the vehicle, minimizing driver input and increasing safety at close distances. The system uses a sensor package to determine and maintain the specified following distance from the lead vehicle using the throttle and brakes of the truck. Within the lead vehicle, the CACC system acts to observe the upcoming roadway and predict upcoming road conditions and velocity changes. The system then communicates this information between platoon vehicles via Dedicated Short Range Communication (DSRC). This allows a follower vehicle to not only actively and continuously monitor and correct separation distance but also be aware of impending changes. The CACC system therefore autonomously monitors not only the highway immediately in front of the tractor, but also the roadway ahead of the platoon. In addition, the measurement and system response to a sudden change in the highway conditions, such as a traffic jam, takes only a fraction of the time required for a human reaction. The communication and distance control between vehicles is completely automated and takes microseconds to complete, drastically improving system response time. At highway speeds, the difference in reaction time between the automated CACC system and a manually controlled truck can be the difference between a collision and a near miss.

Though it does not rely on driver interaction to adjust speed and separation distance, CACC boasts a video link between vehicles to enable drivers within the platoon to visually observe road conditions ahead of the leader vehicle. The only restriction to the automation offered by CACC is lateral control: the driver still manually operates the steering wheel and monitors the system via an informational monitor.

With the functionality offered by the CACC system, it is now possible to form platoons of heavy vehicles following at distances that provide the benefits of drafting but would otherwise be unsafe. Without the restrictions previously imposed upon separation distance by safety concerns, it becomes advantageous to analyze and test systems of heavy vehicles in a leader-follower configuration to determine, quantitatively, the challenges and overall cost benefit associated with platooning.

The Federal Highway Administration (FHWA) stated as part of the Exploratory Advanced Research Progrom (EARP) [12] that systems providing vehicle automation, such as CACC, are of high research interest and scientific value. Thus the team at Auburn University wrote and submitted a proposal to the FHWA and was awarded a contract to develop and investigate all aspects of the CACC, from the human-machine interface to electronic hardware reliability. The work to be performed by the contract awarded to Auburn University is described in [11] and is the major motivation for the research performed herein.

An important facet of [11] is quantitatively determining the drag reduction offered by platooning vehicles. Numerical simulation, such as computational fluid dynamics (CFD), is the method of choice for accomplishing this objective for a host of reasons. First and foremost, CFD provides detailed and accurate information regarding the aerodynamics of the vehicles and can be run in a variety of configurations. Secondly, CFD is far less resource intensive and prohibitive than track testing or even wind tunnel tests. A battery of configurations can be simulated, whereas a road test is limited by available materials and conditions. CFD is also significantly less costly from a financial perspective. The only cost associated with a simulation is the hardware utilized and simulation runtime. A road test, on the other hand, requires several components: vehicles, drivers, fuel, time, and additional resources.

Based on cost effectiveness, simulation is the preferred method of generating aerodynamic information regarding vehicle platoons. As part of the contract awarded to [11], road tests will be performed for a number of cases simulated, in both real world and controlled environments, to validate the predicted fuel savings and determine system reliability, though they are not discussed herein.

It is helpful to simulate generic models with well-known drag profiles to provide an understanding of the aerodynamics associated with multi-body systems. Though this does not give aerodynamic information about a tractor-trailer platoon, it can provide valuable insight into how the flow disturbances from each vehicle interact. In the absence of experimental tractor-trailer data, a well-researched simplified body can also provide an excellent validation case. The chosen body is a representative of a simplified car geometry and is commonly referred to as the Ahmed body. The Ahmed body's aerodynamic characteristics were established and tested via wind tunnel by Ahmed in 1984 [13]. This body was chosen as a generic baseline model not only for the simplicity of the geometry, but also because there is an abundance of research and validation work available for comparison of simulation results.

1.3 Existing Literature

Before the vehicle platoon models were developed and simulated, an in-depth literature search was performed for existing research and publications regarding the platooning of bluff bodies, in particular heavy ground vehicles such as the tractor-trailer configuration. While there exists an abundance of research, both numerical and experimental, on the aerodynamics of simplified ground vehicles and car bodies, such as the Ahmed body [13], there has been little work done regarding the aerodynamic interactions of large vehicle platoons. Much of the work that does exist on ground vehicle platooning was published by the Society of Automotive Engineers (SAE).

Hong *et al.* [14] performed full scale road tests and 1/8th scale wind tunnel tests of a vehicle platoon using Ford minivans as part of the SAE 1998 Technical Paper Series and produced useful results. However, there was an extreme amount of variance in the road test measurements and the data was gathered using a tow bar connecting the two vehicles. While this data is useful from qualitatively, it cannot be directly extrapolated to the research discussed here.

In August 2000, Bonnet and Fritz [15] discussed platoon tests performed using loaded tractor-trailers and measuring reduced fuel consumption. While these results provide key insight, the scope of the project was unfortunately limited to low speeds and not a large range of separation distances. There are also key differences in geometry: the trailers were not full length and the tractor model used was a DaimlerChrysler ACTROS, which is a flat-nosed, cab-over tractor with a significantly different flow profile than the Peterbilt 579 tractors used for experiments and simulations in this research. Due to these factors the overall usefulness of [15] is limited to solely providing qualitative results comparison, similar to [14]. There has also been work, such as that by Adarsh [16] and Chen [17], that is related to vehicle platooning but does not directly deal with the premises discussed here.

Conversely, a paper that is not directly related to tractor-trailer platooning that can be drawn upon for comparison is the SAE Technical Paper published by Pagliarella in 2007 [18]. Paglierella performed wind tunnel tests on Ahmed bodies with multiple slant angles in a tandem configuration and recorded the measured drag on each body. These results provide excellent simulation verification because the resultant drag is normalized by single body drag and produced as a function of body spacing– the primary parameter of interest in this research.

Chapter 2

Methodology and Theoretical Background

This chapter describes the methodology used to generate simulation results as well as the theoretical underpinning of the software and techniques used. The apparatus used for experimental testing is also discussed.

2.1 Modeling and Simulation Overview

The procedure for developing both the generic Ahmed model and the more complex tractor-trailer model was very similar. The modeling process began with geometric modeling of the physical bodies. The 3D geometry for each body was modeled using the Computer Aided Design (CAD) software package, SolidWorks. SolidWorks is developed by Dassault Systemes and is a common CAD software used in industry [19]. The primary reason that SolidWorks was chosen as the geometry modeling package is the geometry integration offered by ANSYS DesignModeler, along with its availability,.

ANSYS DesignModeler is the geometry design portion of the ANSYS Workbench tool management software. DesignModeler (DM) is a parametric geometry design software developed by the simulation tool development company ANSYS Inc. [20]. DM generates geometry files that can then be passed to other ANSYS software components, such as a structural analysis package or, in this case, a computational fluid dynamics package.

While geometry can be designed in DM, for configurations beyond simple geometric shapes it is often more cumbersome than a using a third party CAD software. Fortunately, ANSYS anticipated this and included the feature to automatically read and import geometry from several popular CAD softwares. Thus importing CAD developed in SolidWorks to the ANSYS system is extremely simple. The only modification made in DM was the addition of refinement regions to assist with meshing– regions defined in physical space, but not counted as solid objects, where local grid properties can be specified.

After the geometry was converted to a format readable by ANSYS and the refinement regions were added, the model was passed to ANSYS Meshing. ANSYS Meshing is an unstructured meshing program that is based on the ANSYS ICEM algorithm [21].

Unstructured meshes were chosen over structured meshes due to the known geometric complexity of the tractor-trailer model. A structured mesh could model the Ahmed body with relative ease, but would be extremely cumbersome to generate over the irregular surfaces encountered at the boundary of the tractor geometry. Thus to generate a mesh that has even a modicum of similarity between the physical geometry and resulting control volume, an unstructured mesh is required. For consistency, an unstructured mesh was chosen for the generic simplified body.

After a large amount of refinement (which is discussed in subsequent chapters), the mesh was passed to the numerical flow solver, ANSYS Fluent. Fluent is a robust, unstructured computational fluid dynamics solver capable of modeling several aspects of fluid flow, ranging from turbulence and heat transfer to chemical reactions [22]. Fluent can model a broad range of flows for complex geometries and includes a large number of turbulence models. Because the flow structures behind a tractor-trailer are highly turbulent, this aspect of Fluent is very appealing. The typical flow seen by a tractor-trailer, though very complex from a turbulence perspective, is low enough speed to be treated as incompressible, experiences no phase changes, sees little heat transfer, and is therefore relatively well defined. These reasons, among others, make Fluent an excellent overall choice for numerical flow simulation.

After a solution is computed by Fluent, the pressure and viscous drag forces on the body surface are non-dimensionalized by the traditional constants, freestream air density ρ_∞ and velocity V_∞ and projected frontal area A. This generates the desired numerical result: the coefficient of drag C_D. The drag coefficient is calculated by Eq. (2.1), where F_D is the sum of the pressure and viscous drag force on each surface of the body as calculated by Fluent.

$$C_D = \frac{F_D}{\frac{1}{2}\rho_\infty V_\infty A} \tag{2.1}$$

Drag is only one of a large number of factors that contribute to fuel consumption and this must be considered when determining reduced fuel usage, the ultimate benefit of platooning. Environmental components such as road grade and tire conditions as well as internal elements, such as engine revolutions per minute, are all significant factors that need to be taken into account when determining the fuel consumed. However, if these factors are assumed constant the fuel consumption-drag correlation can be accurately determined and used for comparison.

After a baseline drag was established for a single body, multiple bodies were added to the simulation using the same procedure outlined above. The resulting drag on each body was then compared to the single vehicle coefficient to conclude drag reduction and fuel savings. In addition to numerical analysis, the resulting flow was also examined from a qualitative perspective in Tecplot 360 to determine resulting flow structures and variable profiles. This included examining quantities such as pressure and velocity contours, streamlines, and vorticity magnitude.

2.2 Fluent Parameters and Solver Discretization

There are several factors within Fluent that can be modified to change the methodology and affect the solution generated; thus each parameter must be carefully examined and determined before one can proceed to comment on the validity of the solution. In setting these parameters, it is extremely useful to know the governing equations Fluent uses and how they are discretized so that the effects of each parameter can be better understood.

Governing Equations

As per the Fluent theoretical guide [20], the governing equations solved by Fluent, at a minimum, are conservation of mass and conservation of momentum, given by Eq. (2.2) and Eq. (2.3) respectively.

$$\frac{\partial \rho}{\partial t} + \nabla \cdot (\rho \vec{v}) = S_m \tag{2.2}$$

$$\frac{\partial}{\partial t} (\rho \vec{v}) + \nabla \cdot (\rho \vec{v}) \vec{v} = -\nabla p + \nabla \cdot (\bar{\tau}) + \rho \vec{g} + \vec{F} \tag{2.3}$$

Where:

t = time

ρ = density

$\vec{v}$ = velocity

p = pressure

$\vec{g}$ = gravitational acceleration

$\vec{F}$ = body forces

$\bar{\tau}$ = stress tensor

S_m is the mass added to the continuous phase inside the control volume, such as a phase change (i.e. vaporization of liquid droplets) or user-added sources.

Equation (2.2) and Eq. (2.3) are often referred to as the Navier-Stokes equations and, with an equation of state and conservation of energy, fully define the characteristics of any non-reacting fluid flow. Analytic solutions are only tractable for simplified flows after imposing limiting assumptions. In general, however, there is no known closed form solution to these equations in their entirety; one must resort to numeric approaches to discretize and approximate solutions to Eq. (2.2) and Eq. (2.3).

Additional equations, e.g. convective heat transfer, are added to the solver as needed. Because the flows analyzed for this research are low speed, incompressible air flows, the only addition equations required by the solver are those used in the turbulence model, which is discussed in Sec. 2.3.

Generalized Form

These equations, while independent and fundamental, can be expressed in the more generic form of the transport equation. Equation (2.4) shows the integral form of the transport equation for generic scalar quantity ϕ across an arbitrary volume V. ϕ represents the change of the transported quantity Φ with respect to mass, that is $\phi = d\Phi/dm$. To form the continuity equation, one would let set the transported quantity Φ to be equivalent to mass: $\Phi = m$, and accordingly $\phi = 1$. Similarly, to describe the transport of momentum, one would let $\Phi = mv, \phi = v$.

$$\int\limits_V \frac{\partial \rho\phi}{\partial t} + \oint \rho\phi\vec{v}\cdot d\vec{A} = \oint \Gamma_\phi \nabla_\phi \cdot d\vec{A} + \int\limits_V S_\phi dV \tag{2.4}$$

Where:

$\vec{A}$ = surface area vector

Γ_ϕ = diffusion coefficient for ϕ

∇_ϕ = gradient of ϕ

S_ϕ = source of ϕ per unit volume

Discretization of Eq. (2.4) across a mesh yields, for any given cell:

$$\frac{\partial \rho \phi}{\partial t} V + \sum_{f}^{N_{faces}} \rho_f \vec{v}_f \phi_f \cdot \vec{A}_f = \sum_{f}^{N_{faces}} \Gamma_\phi \nabla_{\phi_f} \cdot \vec{A}_f + S_\phi V \tag{2.5}$$

Where:

N_{faces} = number of faces on the cell

ϕ_f = value of ϕ convected through face f

$\rho_f \vec{v}_f$ = mass flux through face f

Γ_ϕ = the diffusion coefficient of ϕ

$\vec{A}_f$ = area of the face of interest

∇_{ϕ_f} = gradiant of ϕ at f

V = cell volume

There are traditionally two approaches to solving the momentum and continuity flavors of Eq. (2.5): density-based and pressure-based. Both methods use the momentum equation to obtain the velocity field, but differ in their use of continuity. A density-based approach uses the continuity equation to determine the density field, then uses the equation of state (e.g. ideal gas law) to determine pressure. A pressure-based approach, on the other hand, extracts the pressure field by solving a pressure or pressure correction equation obtained through manipulation of the continuity and momentum equations. A pressure-based solver eliminates the need for an equation of state, which can be erroneous or impossible if there are large variations in density. Thus historically, density-based solvers have been used for compressible flows and pressure-based for incompressible. Because all the flows considered herein are incompressible, using a pressure-based solver is a viable option, which allows for further simplification of the governing equations.

Applying the form of Eq. (2.5) to the momentum and continuity equations, assuming a pressure-based solver (incompressibility), and applying steady state for simplicity generates the following equations:

$$a_p\vec{v} = \sum_{nb} a_{nb}\vec{v}_{nb} + \sum p_f A\hat{n} \tag{2.6}$$

$$\sum_{f}^{N_{faces}} J_f A_f = 0 \tag{2.7}$$

Where a_p and a_nb are cell and neighbor momentum coefficients to be solved and J_f is the mass flux through a face f, which can be calculated by weighted average as shown in Eq. (2.8).

$$J_f = \rho_f \frac{a_{p,c0}\, v_{n,c0} + a_{p,c1}\, v_{n,c1}}{a_{p,c0} + a_{p,c1}} + d_f\left[(p_{c0} + (\nabla p)_{c0} \cdot \vec{r_0}) - (p_{c1} + (\nabla p)_{c1} \cdot \vec{r_1})\right] \tag{2.8}$$

Where v_n represents the normal velocity, ci refers to cell i, and d_f is a function of the average of the momentum coefficients $a_{p,c0}$ and $a_{p,c1}$.

Spatial Discretization of the Momentum Equation

Now that the momentum equation has been discretized, consideration must be given to discretization of the independent variables: space and time. Because Fluent, and most CFD solvers, store flow properties at cell centers and the location of interest is the cell faces, spatial discretization is required in all simulations. Though there are several methods of spatial discretization for flow variables available in the Fluent solver, the second order upwind approach was used in all simulation cases. The formulation of the second order upwind method in Fluent, again using the dummy variable ϕ, is as follows:

$$\phi_f = \phi + \Psi \nabla\phi \cdot \vec{r} \tag{2.9}$$

Where $\vec{r}$ is the vectorized distance between the upstream cell centroid and the face f centroid, Ψ is the scalar gradient limiter, determined by a Minmod-based [23] limiting function, and $\nabla\phi$ is the gradient of ϕ, which is calculated by a least squares approach.

The least squares approach to the calculation of the gradient is the default method in Fluent and is used for this analysis because the accuracy is comparable to node-based approaches such as Green-Gauss but is far less computationally expensive.

Imagine a cell $c0$, as shown in the diagram of Fig. 2.1, with $i = 1..n$ neighboring cells. To any cell ci, the gradient of ϕ, which is the change in ϕ over distance r_i, is given by Eq. (2.10), with $\Delta\phi$ representing the change in ϕ, $\phi_{ci} - \phi_{c0}$.

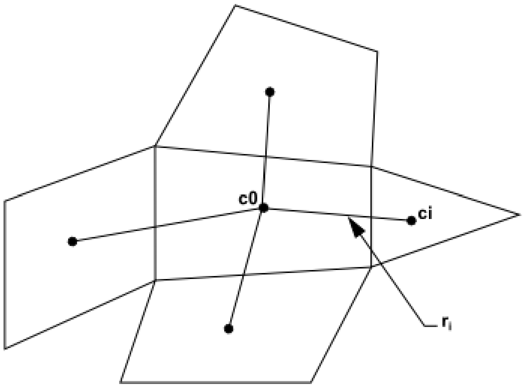

Figure 2.1: Least Squares Gradient Calculation

$$[J](\nabla\phi)_{c0} = \Delta\phi \tag{2.10}$$

The coefficient matrix $[J]$ is a pure function of geometry and can be easily calculated. For example, in a Cartesian grid if r_i were unidirectional, $[J]$ would equal r_i. This system is over-determined and is solved in Fluent by decomposing the coefficient matrix using Gram-Schmidt algorithm. This process generates three directional weight components for each cell, termed W_{i0}^{x}, W_{i0}^{y}, and W_{i0}^{z}. Thus for each face f and corresponding neighbor cell i the gradient is given by:

$$\phi_{x,c0} = \sum_{i=1}^{n} W_{i0}^{x} \cdot (\phi_{ci} - \phi_{c0}) \tag{2.11}$$

$$\phi_{y,c0} = \sum_{i=1}^{n} W_{i0}^{y} \cdot (\phi_{ci} - \phi_{c0}) \tag{2.12}$$

$$\phi_{z,c0} = \sum_{i=1}^{n} W_{i0}^{z} \cdot (\phi_{ci} - \phi_{c0}) \tag{2.13}$$

$$\nabla\phi = \phi_{x,c0}\,\hat{\imath} + \phi_{y,c0}\,\hat{\jmath} + \phi_{z,c0}\,\hat{k} \tag{2.14}$$

Spatial Discretization of the Continuity Equation

As alluded to above, incompressibility simplifies the continuity equation and thus special considerations can be given to the discretization of the density and pressure variables. Using a pressure-based solver does not require the traditional second order upwind approach for the continuity equation, which can be surmised from Eq. (2.8).

Because the fluid is incompressible, Fluent calculates the density variation between cell center and face simply using arithmetic averages. To calculate pressure at a face p_f, several methods are offered. The method used for this analysis is calculated with a weighted average, as described in Eq. (2.15).

$$p_f = \frac{\dfrac{1}{a_{p,c0}} p_{c0} + \dfrac{1}{a_{p,c1}} p_{c1}}{\dfrac{1}{a_{p,c0}} + \dfrac{1}{a_{p,c1}}} \tag{2.15}$$

Temporal Discretization

Steady state analysis was done for most of the test cases in this project, but transient formulation was required for the Detached Eddy Simulation turbulence model, which is discussed in Sec. 2.3.

Several schemes for temporal discretization are available in Fluent. For this work, a Bounded Second Order Implicit approach was selected. This approach is attractive since it is known to be numerically stable over a wide range of problems. This technique in implemented in Fluent, for any independent variable ϕ, as follows:

$$\frac{\partial \phi}{\partial t} = \frac{\phi_{n+1/2} - \phi_{n-1/2}}{\Delta t} \tag{2.16}$$

$$\phi_{n+1/2} = \phi_n + \frac{1}{2}\beta_{n+1/2}\left(\phi_n - \phi_{n-1}\right) \tag{2.17}$$

$$\phi_{n-1/2} = \phi_{n-1} + \frac{1}{2}\beta_{n-1/2}\left(\phi_{n-1} - \phi_{n-2}\right) \tag{2.18}$$

$$\tag{2.19}$$

Where n, $n-1$, and $n-2$ are discrete time levels and $n-1/2$ and $n+1/2$ are interpolated time levels. $\beta_{n+1/2}$ and $\beta_{n-1/2}$ are bounding factors determined by turbulent flow properties such as turbulent kinetic energy, dissipation rate, and specific dissipation rate.

System Solution

Making use of a pressure-based solver also allows for special modeling of the coupling between the continuity and momentum equations and Fluent offers multiple methods for accomplishing this via the “Pressure-Velocity Coupling” option. Using the “COUPLED” scheme effectively allows for a simultaneous solution to the continuity and momentum equations without applying a predictor-corrector approach; thus producing an accurate solution and lower computational time method. The one caveat to this method is that additional

Random Access Memory (RAM) is required by the solver, as it must store more information than with a predictor-corrector scheme.

The resultant discretized system is linear by design. After combining the momentum and continuity equations, the results can be expressed in the residual form shown in Eq. (2.20):

$$\sum_j [A]_{ij} \vec{X}_j = \vec{B}_i \tag{2.20}$$

Where $[A]_{ij}$ is a 4x4 coefficient matrix describing the influence cell i has on cell j. The unknown and residual vectors have the form:

$$\vec{X}_j = \begin{bmatrix} p'_i \\ u'_i \\ v'_i \\ w'_i \end{bmatrix} \qquad \vec{B}_i = \begin{bmatrix} -r_i^p \\ -r_i^u \\ -r_i^v \\ -r_i^w \end{bmatrix} \tag{2.21}$$

Equation (2.20) is then solved for every cell using the coupled algebraic multigrid (AMG) solver within Fluent. Algebraic multigrid is a numerical analysis method that solves linear systems in such a way that only depends on the coefficients of the underlying matrix [24]. AMG is preferred for large sparse matrices, such as the ones that appear in discretization techniques, because they solve N-unknown systems with only $O(N)$ work and can be parallelized, which is both optimal and scalable.

Under-Relaxation Factors

Though the analysis above linearizes the Navier-Stokes equations, their true nonlinearity must be taken into account when calculating their solution. This is accomplished by applying correction terms throughout the analysis. This technique is often referred to as under-relaxation. There are two types of under-relaxation used by Fluent: explicit relaxation and implicit relaxation.

Explicit relaxation, or variable relaxation, is applied directly to the variable of interest, as described by Eq. (2.22). This changes the previous cell value ϕ_{old} to a new value ϕ by using the computed change $\Delta\phi$ and the used-specified under-relaxation factor.

$$\phi = \phi_{old} + \alpha\Delta\phi \tag{2.22}$$

Implicit relaxation, or equation relaxation, is effected by introducing selective amounts of ϕ into the desired equation, for example:

$$\frac{a_p\phi}{\beta} = \sum_{nb} a_{nb}\phi_{nb} + b + \frac{1-\beta}{\beta}a_p\phi_{old} \tag{2.23}$$

Where β is a function of the user-specified Courant-Friedrichs-Lewy (CFL) parameter:

$$\frac{1-\beta}{\beta} = \frac{1}{CFL}$$

Under-relaxation factors do not affect the final solution quality as a properly relaxed simulation will converge to the same solution regardless of specified factors. They do, however, affect the convergence ability of the simulation. A simulation that is too relaxed (large factors) will often diverge creating erroneous results. Conversely, a simulation that is not relaxed enough (small factors) will converge to a valid solution, but will take much longer than necessary. The appropriate under-relaxation factors directly correspond to mesh quality and element skewness, discussed in Sec. 2.4. A higher quality mesh requires less strict under-relaxation factors.

2.3 Turbulence Models

Turbulent fluid motion is a well-known phenomenon that often occurs in nature. From smoke rising from a cigarette to continent-sized oceanic currents, turbulence occurs continuously on a wide spectrum of time and length scales and directly impacts our environment in a variety of ways. Most turbulent flows are extremely complex and characterized by chaotic fluid property changes and irregular, seemingly random, motion.

Despite being so well-observed, little is known about modeling turbulence. Turbulence is challenging to simulate effectively due to the nonlinearity and its apparent non-closure of the Navier-Stokes equations. Two primary turbulence models were considered and utilized in this work: a traditional model called "k-ε" and a newer model termed "Detached Eddy Simulation."

Reynolds Decomposition

To better examine the nature of turbulence, and where within the Navier-Stokes equations it is generated, a mathematical technique called Reynolds decomposition is often employed. As described in Eq. (2.24), Reynolds decomposition is the process of separating a quantity ϕ into two parts: a fluctuation ϕ' and an average $\bar{\phi}$.

$$\phi = \bar{\phi} + \phi' \tag{2.24}$$

By assuming that every property has an average value and that turbulence is simply small deviations from the average value, it is possible to manipulate Eq. (2.25), conservation of momentum, in such a manner that draws out the nonlinear terms that give rise to turbulent flow.

$$\rho \left[\frac{\partial v_i}{\partial t} + v_j \frac{\partial v_i}{\partial x_j} \right] = -\frac{\partial p}{\partial x_i} + \frac{\partial \tau_{ij}}{\partial x_j} \tag{2.25}$$

Where i and j are indices representing spatial components. Decomposing each property (except density because the fluid is incompressible) into an average and fluctuating part yields:

$$\rho \left[\frac{\partial(\bar{v_i} + v_i')}{\partial t} + (\bar{v_j} + v_j') \frac{\partial(\bar{v_i} + v_i')}{\partial x_j} \right] = -\frac{\partial(\bar{p} + p')}{\partial x_i} + \frac{\partial(\bar{\tau_{ij}} + \tau_{ij}')}{\partial x_j} \tag{2.26}$$

Assuming the mean of a fluctuation is zero and keeping in mind averaging and differentiation commute, the average of Eq. (2.26) is:

$$\rho\left[\frac{\partial(\bar{v_i})}{\partial t}+(\bar{v_j})\frac{\partial(\bar{v_i})}{\partial x_j}+\left\langle v_j'\frac{\partial v_i'}{\partial x_j}\right\rangle\right]=-\frac{\partial(\bar{p})}{\partial x_i}+\frac{\partial(\bar{\tau_{ij}})}{\partial x_j} \tag{2.27}$$

Where ⟨⟩ represents the arithmetic average of a quantity. A similar approach can be used to average Eq. (2.28) (conservation of mass) and arrive at Eq. (2.29).

$$\frac{\partial\bar{v_j}+v_j'}{\partial x_j}=0 \tag{2.28}$$

$$\frac{\partial\bar{v_j}}{\partial x_j}=0 \tag{2.29}$$

Subtracting Eq. (2.29) from Eq. (2.28) then yields Eq. (2.30), which can be multiplied by $\rho v_i'$ and averaged again to give Eq. (2.31):

$$\frac{\partial v_j'}{\partial x_j}=0 \tag{2.30}$$

$$\rho\left\langle v_i'\frac{\partial v_j'}{\partial x_j}\right\rangle=0 \tag{2.31}$$

Adding this to the averaged momentum equation Eq. (2.27) gives:

$$\rho\left[\frac{\partial(\bar{v_i})}{\partial t}+(\bar{v_j})\frac{\partial(\bar{v_i})}{\partial x_j}\right]+\rho\left[\left\langle v_j'\frac{\partial v_i'}{\partial x_j}\right\rangle+\left\langle v_i'\frac{\partial v_j'}{\partial x_j}\right\rangle\right]=-\frac{\partial(\bar{p})}{\partial x_i}+\frac{\partial(\bar{\tau_{ij}})}{\partial x_j} \tag{2.32}$$

Applying the commutable property of arithmetic averaging, the product rule of differentiation, and moving the resulting term to the right hand side yields:

$$\rho\left[\frac{\partial(\bar{v_i})}{\partial t}+(\bar{v_j})\frac{\partial(\bar{v_i})}{\partial x_j}\right]=-\frac{\partial(\bar{p})}{\partial x_i}+\frac{\partial(\bar{\tau_{ij}})}{\partial x_j}-\rho\left\langle\frac{\partial(v_i'v_j')}{\partial x_j}\right\rangle \tag{2.33}$$

$$\rho\left[\frac{\partial(\bar{v_i})}{\partial t}+(\bar{v_j})\frac{\partial(\bar{v_i})}{\partial x_j}\right]=-\frac{\partial(\bar{p})}{\partial x_i}+\frac{\partial}{\partial x_j}\left[\bar{\tau_{ij}}-\rho\langle v_i'v_j'\rangle\right] \tag{2.34}$$

The Reynolds averaged momentum equation, Eq. (2.34), and the averaged continuity equation, Eq. (2.29), are collectively referred to as the Reynolds Averaged Navier Stokes (RANS) equations. This analysis is the traditional approach to turbulence modeling.

Notice that there are now two stress terms: the stress tensor resulting from the viscosity of the fluid and the fluctuation contribution from the non-linear acceleration terms. The second term, while not a stress in physical terms, is referred to as the Reynolds stress and is the source of turbulence.

The appearance of the Reynolds stresses may seem to complicate the problem, it adds several unknown quantities to the system without adding any additional equations, forming a very ill-posed problem. However, by writing the equations in RANS form, the source of turbulence has been isolated into a single term and can be modeled independently from the remainder of the equations.

Traditionally, there are several methods of modeling the Reynolds stresses and a large number of models have been developed over time; each possessing specific applications or strengths. Models are typically classed by their order or by the number of additional transport equations added to solve for the Reynolds stresses. Models range from first order algebraic, which contain zero additional transport equations, to higher order models, which can contain up to seven additional transport equations, such as the Reynolds Stress Model (RSM).

Realizable k-ε

The primary turbulence model used herein was the realizable k-ε (RKE) model. RKE is a RANS-based, two equation model first developed in 1972 by Jones and Launder [25]. The model has since become one of the most widely used turbulence models in CFD.

The “k” in RKE stands for turbulent kinetic energy (TKE) and “ε” is the turbulent dissipation. The first transported variable, TKE is defined using the traditional definition of massless kinetic energy, as shown in Eq. (2.35). The second, turbulent dissipation is the rate of dissipation of TKE due to viscous stresses and is formally defined in a differential form by Eq. (2.36).

$$k \equiv \frac{1}{2}\left(\overline{u'u'} + \overline{v'v'} + \overline{w'w'}\right) \tag{2.35}$$

$$\varepsilon \equiv \nu \overline{\frac{\partial v_i'}{\partial x_k}\frac{\partial v_i'}{\partial x_k}} \tag{2.36}$$

The two new transport equations governing the flow of these variables are:

$$\frac{\partial}{\partial t}(\rho k) + \frac{\partial}{\partial x_j}(\rho k v_j) = \frac{\partial}{\partial x_j}\left[\left(\mu + \frac{\mu_t}{\sigma_k}\right)\frac{\partial k}{\partial x_j}\right] + P_k + P_b - \rho\varepsilon - Y_M + S_k \tag{2.37}$$

$$\frac{\partial}{\partial t}(\rho \varepsilon) + \frac{\partial}{\partial x_j}(\rho \varepsilon v_j) = \frac{\partial}{\partial x_j}\left[\left(\mu + \frac{\mu_t}{\sigma_k}\right)\frac{\partial \varepsilon}{\partial x_j}\right] + \rho C_1 S\varepsilon - \rho C_2 \frac{\varepsilon^2}{k + \sqrt{\nu\varepsilon}} + C_{1\varepsilon} C_{3\varepsilon}\frac{\varepsilon}{k} P_b + S_\varepsilon \tag{2.38}$$

Where the model constants are given by:

$$C_{1\varepsilon} = 1.44$$

$$C_{2\varepsilon} = 1.92$$

$$C_{\mu} = 0.09$$

$$\sigma_k = 1.0$$

$$\sigma_{\varepsilon} = 1.3$$

With C_1 given by:

$$C_1 = \max\left[0.43, \frac{\eta}{\eta + 5}\right]$$
$$\eta = S\frac{k}{\varepsilon}$$
$$S = \sqrt{2S_{ij}S_{ij}}$$

S is the modulus of the mean strain rate tensor, S_{ij} being the rate of strain of directional relevance, given by:

$$S_{ij} = \frac{1}{2}\left(\frac{\partial v_j}{\partial x_i} + \frac{\partial v_i}{\partial x_j}\right) \tag{2.39}$$

P_k and P_b represent the production of turbulent kinetic energy due to mean velocity gradiants and buoyancy, respectively. They are calulated by:

$$P_k = \mu_t S^2$$

$$P_b = \beta g_i \frac{\mu_t}{Pr_t} \frac{\partial T}{\partial x_i}$$

$$\beta = -\frac{1}{\rho}\left(\frac{\partial \rho}{\partial T}_p\right)$$

β is the coefficient of thermal expansion, Pr_t is the turbulent Prandtl number with a constant value of $Pr_t = 0.85$ for the realizable model, and g_i is the gravitational acceleration in the i direction.

Finally, an important variable yet to be discussed is the turbulent or eddy viscosity, μ_t. This quantity was first formulated by Boussinesq in 1877 [26] and models the momentum transfer caused by turbulent eddies. It is titled after the fluid property of the same name because fluid viscosity similarly measures the amount of momentum transfer caused by molecular diffusion within a fluid, i.e. fluid friction. Turbulent viscosity is modeled in RKE by the following equations:

$$\mu_t = \rho C_\mu \frac{k^2}{\varepsilon} \tag{2.40}$$

Where:

$$C_\mu = \frac{1}{A_0 + A_s \frac{kU^*}{\varepsilon}}$$

$$U* = \sqrt{S_{ij}S_{ij} + \tilde{\Omega}_{ij}\tilde{\Omega}_{ij}}$$

$$\tilde{\Omega}_{ij} = \Omega_{ij} - 2\varepsilon_{ijk}\omega_k$$

$$\Omega_{ij} = \bar{\Omega}_{ij} - \varepsilon_{ijk}\omega_k$$

$\bar{\Omega}_{ij}$ being the mean rate of rotation tensor viewed in a rotating reference frame with angular velocity ω_k. The constants A_0 and A_s are given by:

$$A_0 = 4.04, \qquad A_s = \sqrt{6}\cos\phi$$
$$\phi = \frac{1}{3}\arccos(\sqrt{6}W), \quad W = \frac{S_{ij}S_{jk}S_{ki}}{(SijS_{ij})^{3/2}}$$

A caveat to this model is that of near-wall treatment. Near-wall treatment is a critical aspect of the design, as solid boundaries are the main source of vorticity and turbulence in a flow and turbulent flow is strongly affected by the presence of a wall. The RKE turbulence model cannot capture the non-trivial effects that occur in near wall regions and thus a secondary near-wall model is added– typically in the form of a semi-empirical wall function.

When turbulent flow encounters a wall boundary, three primary layers form: an inner layer, where (molecular) viscous shear dominates, an outer layer where turbulent shear prevails, and a center blending layer where neither force eclipses the other. Each of these layers has different behavior and this must be taken into account by the wall function.

The standard wall function in Fluent is a two layer approach (viscous and turbulent shear dominant layers) and is based on the work of Launder and Spalding [27] and modifies the velocity calculation. Instead of using momentum transport to solve for velocity, it is calculated instead using the law of the wall:

$$v^* = \frac{1}{\kappa}\ln(Ey^*) \tag{2.41}$$

v^* and $y*$ are dimensionless velocity and distance from the wall, defined as:

$$v^* \equiv \frac{v_p C_\mu^{1/4} k_P^{1/2}}{\tau_w/\rho}$$

$$y^* \equiv \frac{\rho C_\mu^{1/4} k_P^{1/2} y_P}{\mu}$$

where:

$E =$ empirical constant $= 9.793$

$\kappa =$ von Kármán constant $= 0.4187$

$v_P =$ mean velocity at the near-wall node P

$y_P =$ distance to the wall from P

$k_P =$ turbulent kinetic energy at P

Unfortunately, this form of velocity does not account for the effect of the pressure gradient, which can lead to quite severe errors in the case of large pressure gradients. This presents a significant problem for bluff bodies, such as a tractor-trailer or the Ahmed body, as large pressure gradients are often present on their surfaces. This is countered by modifying the velocity with a non-equilibrium approach, as developed by Kim [28], to make the model sensitive to the effects of spatially changing pressure. The desired effect is achieved by replacing the mean velocity v_P with the modified velocity $\tilde{v}$, as shown in Eq. (2.42):

$$\tilde{v} = v - \frac{1}{2}\frac{dp}{dx}\left[\frac{y_v}{\rho\kappa\sqrt{k}}\ln\left(\frac{y}{y_v}\right) + \frac{y - y_v}{\rho\kappa\sqrt{k}} + \frac{y_v^2}{\mu}\right] \tag{2.42}$$

With y_v being the viscous sublayer thickness, calculated by:

$$y_v \equiv \frac{\mu y_v^*}{\rho C_\mu^{1/4} k_P^{1/2}}$$

$$y_v^* = \text{empirical constant} = 11.225$$

The dimensionless velocity then becomes:

$$v^* = \frac{\tilde{U} C_\mu^{1/4} k_P^{1/2}}{\tau_w/\rho}$$

In the standard wall function, the local equilibrium principle leads to the assumption that the production (P_k) and dissipation (ε) rates of TKE are equal at wall adjacent cells, allowing expressions for P_k and ε to be developed, as shown in Eq. (2.43) and Eq. (2.44).

$$G_k \approx \tau_w \frac{\partial v}{\partial y} = \frac{\tau_w^2}{\kappa \rho C_\mu^{1/4} k_P^{1/2} y_p} \tag{2.43}$$

$$\varepsilon_P = \frac{C_\mu^{3/4} k_P^{3/2}}{\kappa y_P} \tag{2.44}$$

The transport equation for turbulent kinetic energy k is then solved throughout the domain, using the expression in Eq. (2.43) and the following boundary condition at the wall:

$$\frac{\partial k}{\partial n} = 0$$

Though Eq. (2.43) allows use of the TKE transport equation, Eq. (2.44) directly conflicts with the dissipation transport equation. Thus at wall adjacent cells, Eq. (2.44) is used instead of the ε transport equation.

Equation (2.43) and Eq. (2.44) are dependent on the equilibrium assumption. However, local equilibrium is violated by the introduction of the modified law of the wall expression and instead an average spatial TKE production per cell is calculated for the TKE transport equation, as shown by Eq. (2.45). For quadrilateral and hexahedral cells, which account for most near wall cells, the volume average can be approximated using a depth averaged, as shown. For cells of other types, e.g. triangular or tetrahedral, the appropriate volume averages are used.

$$\overline{G_k} \equiv \frac{1}{y_n} \int_0^{y_n} \tau_t \frac{\partial v}{\partial y} dy = \frac{1}{\kappa y_n} \frac{\tau_w^2}{\rho C_\mu^{1/4} k_P^{1/2}} \ln\left(\frac{y_n}{y_v}\right) \tag{2.45}$$

With y_n being the height of the cell. Again, the ε expression is replaced by a volume averaged (or depth averaged) expression:

$$\bar{\varepsilon} \equiv \frac{1}{y_n} \int_0^{y_n} \varepsilon dy = \frac{1}{y_n} \left[\frac{2\nu}{y_v} + \frac{k_P^{1/2} C_\mu^{3/4}}{\kappa} \ln\left(\frac{y_n}{y_v}\right)\right] k_p \tag{2.46}$$

Lastly, as part of the non-equilibrium two layer wall function, the following modifications are made to turbulent quantities within the equations above to differentiate between the viscous and turbulent shear layers. Within the viscous sublayer, when $y < y_v$:

$$\tau_t = 0 \qquad k = \left(\frac{y}{y_v}\right)^2 k_p \qquad \varepsilon = \frac{2\nu k}{y^2} \tag{2.47}$$

In the turbulent sublayer, when $y > y_v$:

$$\tau_t = \tau_w \qquad k = k_p \qquad \varepsilon = \frac{k^{3/2} C_\mu^{3/4}}{\kappa y} \tag{2.48}$$

Large Eddy Simulation

A more recently developed, non-traditional turbulence model is Large Eddy Simulation (LES). LES is a technique that was first proposed by Smagorinsky in 1963 [29] and operates primarily on the principle that large eddies, or vortices, in a flow are dependent on the geometry while smaller scales are universal and can be implicitly accounted for using a subgrid-scale (SGS) model. This implies that one can effectively separate the flow fields into a resolved and a sub-grid portion, which are mutually exclusive. The resolved field represents the geometry-dependent "large eddies" and the sub-grid portion models the "small scales." Despite being independent, the small-scale component does have an effect on the resolved component, which is included in the governing equations via the SGS model.

Though the LES model was not directly used to simulate turbulence within the simulations discussed here, it is a fundamental portion of the Detached Eddy Simulation (DES) model. The DES model was the secondary model used for turbulence analysis and, because DES is based in the LES model, LES merits discussion and explanation for clarity of the DES model.

Separating the velocity field into resolved and SGS elements is accomplished via low-pass filtering. Mathematically, this is represented using a filter convolution kernel G to produce the resolved field, as shown in Eq. (2.49). Equation (2.49) represents both a spatial and temporal filtering across the entirety of both domains.

$$\bar{\phi}(\vec{x},t) = \int_{-\infty}^{\infty}\int_{-\infty}^{\infty} \phi(r,t')G(\vec{x}-\vec{r},t-t')dt'd\vec{r} \tag{2.49}$$

$$\bar{\phi} = G * \phi \tag{2.50}$$

$$\phi = \bar{\phi} + \phi' \tag{2.51}$$

Whereas with the RANS analysis, $\bar{\phi}$ was the average flow property and ϕ' was the fluctuation, $\bar{\phi}$ is now the resolved, or large scale component, and ϕ' is the SGS, or small scale component. Though not entirely analogous, the representations are comparable.

The filtering function G uses cutoff length and time scales, typically referred to as Δ and τ_c, to remove small scales from the resolved component. Though there are several types of appropriate filters that have been developed for the LES method, typically no explicit filtering is done. Instead, a simple box filter is used with the cutoff length being drawn from the mesh grid. For example, a spatial box filter is shown in Eq. (2.52) which will cut off any values beyond half a filter length away.

$$G(x-r) = \begin{cases} \dfrac{1}{\Delta}, & \text{if } |x-r| \leq \dfrac{\Delta}{2} \\ 0, & \text{otherwise} \end{cases} \tag{2.52}$$

Now that a method of differentiating between scales within the flow has been developed, the principle of filtering can be applied to the governing Navier-Stokes equations by substituting $\phi = \bar{\phi} + \phi'$ for variables of interest, namely pressure and velocity. Again, density is not a parameter of interest as the flow is incompressible. The continuity equation remains unchanged, but the momentum equation becomes:

$$\frac{\partial \bar{v}_i}{\partial t} + \frac{\partial}{\partial x_j}(\overline{u_i u_j}) = -\frac{1}{\rho}\frac{\partial \bar{p}}{\partial x_i} + 2\frac{\mu}{\rho}\frac{\partial S_{ij}}{\partial x_j} \tag{2.53}$$

This equation presents a problem, however, as the resolved quantity $\overline{u_i u_j}$ cannot be calculated since it requires knowledge of the yet-to-be-determined unfiltered velocity field. Following Leonard [30], this term can be decomposed into more manageable form:

$$\overline{u_i u_j} = \bar{u}_i \bar{u}_j + \tau_{ij}^r \tag{2.54}$$

That is, the resolved multiple of velocity components is equivalent to the multiple of the resolved components plus some residual stress tensor, τ_{ij}^r. Substituting this into Eq. (2.53) yields:

$$\frac{\partial \bar{v}_i}{\partial t} + \frac{\partial}{\partial x_j}(\bar{u}_i \bar{u}_j) = -\frac{1}{\rho}\frac{\partial \bar{p}}{\partial x_i} + 2\nu\frac{\partial}{\partial x_j}(S_{ij} - \tau_{ij}^r) \tag{2.55}$$

With ν being defined as the kinematic viscosity, $\nu = \mu/\rho$. This form is similar to the RANS method in that the residual stress tensor τ_{ij}^r can be modeled independently from the remainder of the equation.

The residual stress tensor term is calculated by the subgrid-scale model, of which several are available. SGS models often use a simlar approach to RANS-based techniques to calculate the residual stress, employing the Boussinesq hypothesis [26] to express the residual via the resolved scale strain rate tensor:

$$\tau_{ij} - \frac{1}{3}\tau_{kk}\delta_{ij} = -2\mu_t \bar{S}_{ij} \tag{2.56}$$

Before proceeding, it is important to note that this analysis does not preclude steady state analysis: there is no implicit assumption that requires a transient formulation to be used. However, because turbulent flow is inherently comprised of unstable structures, particularly when attempting to examine smaller scales such as the subgrid scale, transient analysis is often used with LES techniques as it provides a more accurate result. It should be noted that the LES (and DES) model within Fluent was designed exclusively for transient analysis and results produced with a steady state approximation are unreliable. Thus for all DES simulations, transient analysis was used.

Since its inception, Large Eddy Simulation has been shown to be more accurate for modeling turbulence when compared to the traditional Reynolds averaged approach. However, the improved solution fidelity comes at the cost of greatly increased computation time. In terms of computational resources required, LES is second only to Direct Numeric Simulation (DNS) [31], which discretizes and solves the Navier-Stokes equations directly without introducing turbulence models and can takes weeks for even the simplest of cases. The large increase in time requirement is due to the fact that even though an LES solver “ignores” the small scales, they must still be accounted for using a sub-grid scale, which is effectively equivalent to simulating a very large increase in mesh size.

The problem can become exacerbated in regions where the mesh is already fine, such as near-wall regions. Here, creating and analyzing a subgrid scale can become prohibitively expensive from a computational perspective. Reasons such as this are the main causes

RANS-based simulations are still prevalent in CFD, except in cases where much higher fidelity solutions are required.

Detached Eddy Simulation

To achieve the accuracy of LES without the massive computational cost, RANS-LES hybrid models, such as Detached Eddy Simulation (DES), have been developed. DES is the second turbulence model explored herein and combines the accuracy of the LES model with the lower computational cost of the RANS models. DES was first proposed by Spalart in 1997 [32] and is often considered to be more accurate than a traditional RANS approach, particularly with bluff bodies [33].

DES is referred to as a hybrid model, because it utilizes both LES and RANS approaches to model turbulence. In regions with low grid density (such as far away from the body), the LES approach is used because it produces a more accurate result. In high grid density regions (i.e. near wall), the model transitions to a traditional RANS formulation at the cost of a slight decrease in solution accuracy, but achieving a greatly reduced computational time. Thus the DES model has more computational cost than a RANS technique, but far less than a pure LES application. The increase in time comes with an increase in accuracy that makes the solution very comparable to the LES technique without the often unfeasible calculation time requirements.

The DES implementation in Fluent offers three RANS methods: Spalart-Allermas (SA), realizable k-ε, and shear stress transport k-ω (SST k-ω). The original formulation of DES, proposed by Spalart [32], utilized the SA method. For this research, both DES-SA and DES-RKE formulations were compared.

2.4 Mesh Quality

Though most of the protean parameters within the modeling and simulation process come from the numeric scheme used to solve the equations governing the flow, discretizing the geometry in a satisfactory fashion is one of the most critical elements of modeling. Low quality meshes will often produce low quality solutions that, if they can be made to converge at all, are unreliable. The solution output can only be as good as the mesh input, thus it is very important to begin with a high quality mesh.

The main metric used to evaluate the meshes generated for this research was skewness. Illustrated in Fig. 2.2, skewness is the measure of how close an element is to its "ideal" equiangular equivalent. For example, in an unstructured mesh the preferred element is a hexahedron, a polyhedron with six faces. The zero skewness (ideal) regular hexahedron would be a cube, because each angle is equivalent within the cube. Shearing the cube would create a rhombohedron, which would have an associated skewness when compared to the original cube.

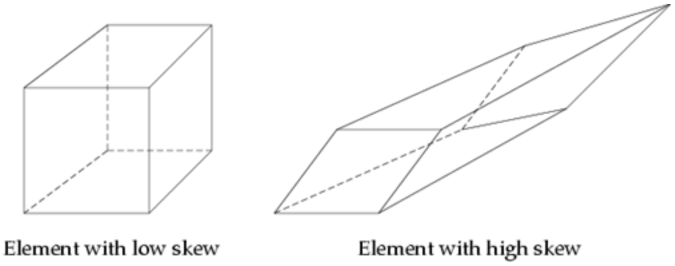

Figure 2.2: Element Skewness

Element skew can range from zero to one, with zero being equiangular and one being a physically impossible, or degenerate, element. An element with a skewness of one is an element that has collapsed upon itself, effectively creating a 2D plane in a 3D mesh, which is unphysical and unsolvable. Table 2.1 below shows skewness and the typically associated element quality [34].

Skewness is an apt indicator of mesh quality because it represents the amount of deviation from an orthogonal mesh that exists within the domain. Cartesian meshes are inherently more accurate than unstructured meshes because skewed elements lower the accuracy of interpolation regions. Large skew elements can even compromise the results of interpolation. Therefore the lower the mesh skewness, the better. Because each element has an associated

Table 2.1: Element Quality

Skewness	**Element Quality**
0	Ideal
0.01 - 0.25	Excellent
0.26 - 0.50	Good
0.51 - 0.75	Fair
0.76 - 0.90	Poor
0.91 - 0.99	Bad (Sliver)
1	Degenerate

skewness, there are two main components associated with the skewness metric: average and maximum element skewness.

Average skewness is the mean skewness of every element and measures the overall quality of the mesh. It is particularly useful when making broad statements about mesh quality and determining the appropriate solution relaxation and tolerance parameters within Fluent. For meshes generated here, the average cell skewness was found to be between 0.25 and 0.26. As seen in Table 2.1, this constitutes good, bordering-on-excellent average cell quality. Because most meshes are comprised of several million elements, an average is not representative of outlier elements with high skewness, which can often remain undetected. Measuring maximum element skewness can be used to combat this by highlighting areas where a few elements are largely skew.

Maximum skewness is an important quantity to calculate because unstructured meshes, by their nature, can be prone to extreme skewness when resolving advanced geometric features. Most 3D unstructured meshes will have elements that are low to poor quality, particularly in regions with complex geometry. Fluent is a robust solver and can handle very large local element skewness, up to approximately 0.95 for most cases, before a mesh becomes unsolvable. The maximum allowable skewness for elements in meshes developed for this research was 0.90. This ensures that so-called “sliver” elements do not appear and affords more relaxed solution parameters in the Fluent simulation; allowing for quicker solution convergence. In most cases, the number of elements that approached this threshold was very minimal, approximately 10 or so out of 5 million. These elements most often occurred in regions where the geometric gradient was extremely sharp.

Chapter 3

Simplified Car Body

The first geometry developed and simulated was a single generic, simplified body. The model, colloquially known as the Ahmed body, is a bluff body that is representative of a simplified car geometry. The model's namesake, S. R. Ahmed, first developed and tested the geometry via wind tunnel experiments in 1984 [13].

The Ahmed body is an excellent test body because while it can be constructed of basic geometric shapes, it is not overly simplistic and is an effective representation of a bluff body. A bluff body is a body that is not aerodynamically optimized and typically has poor aerodynamic performance, this includes most ground vehicle bodies such as cars, vans, and, most relevant to this research, tractor-trailers.

3.1 Geometry

The 2D geometry of a generic Ahmed body is shown in Fig. 3.1, all measurements are shown in millimeters (mm). The original wind tunnel tests of the Ahmed body tested a variety of backlight angles, designated by φ in Fig. 3.1. The primary angle used in simulations for this research was 0°. A body with no rear slope was chosen to more closely simulate the tractor-trailer configuration, which also has no taper and is box-like. The 0° angle body was also chosen because the wind tunnel drag coefficient is determined numerically, as opposed to graphically, within the 1984 Ahmed paper.

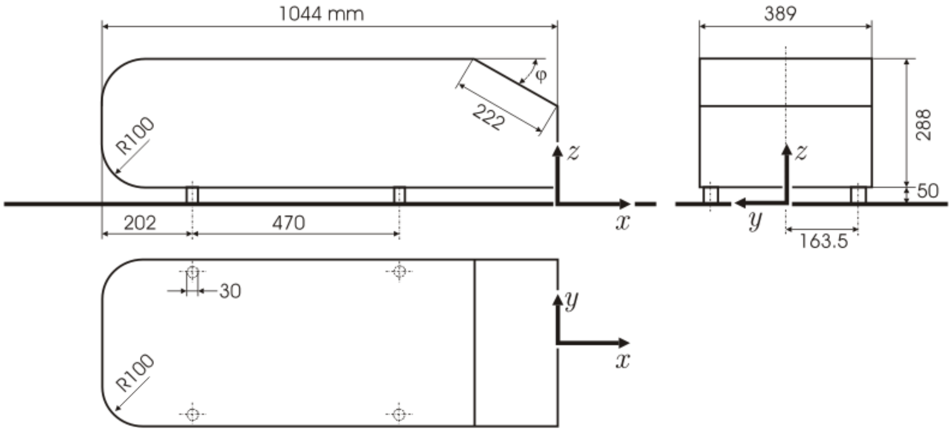

Figure 3.1: Generic Ahmed body 2D drawing

The isometric view provided by Fig. 3.2 illustrates the no-slope body and is the model that was used for all the single and multiple Ahmed body simulations. The model was created from the dimensions shown in Fig. 3.1 and thus has a reference length of 1.044 meters (m) and, more pertinently, a frontal cross sectional area of 0.115032 m^2.

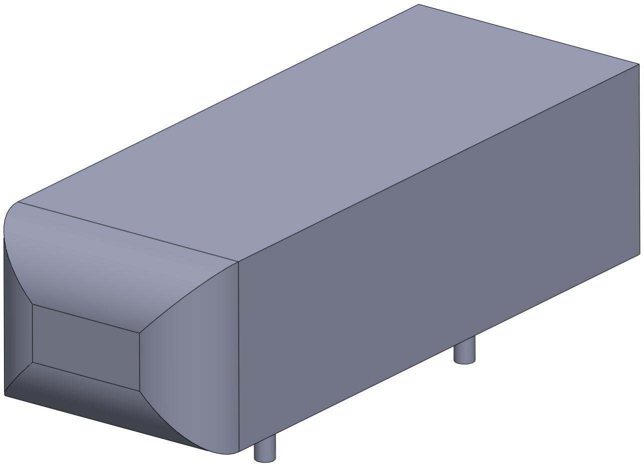

Figure 3.2: Ahmed body isometric view

3.2 Meshing

After the above model was produced in SolidWorks and imported into Design Modeler, the meshing process was begun. Because of the simplicity of the Ahmed body, meshing was accomplished with relative ease. The simplicity also allowed for direct analysis of the impact various sizing parameters had on overall mesh size and quality.

Global Meshing Parameters

The global parameters are the user-specified values that the ICEM algorithm (upon which ANSYS Meshing is based) uses to build the basis of the mesh and define elements in the absence of locally imposed sizing constraints. Table 3.1 lists the majority of the global meshing parameters used.

Table 3.1: Ahmed body global mesh parameters

Parameter	**Value**
Advanced Sizing	Proximity and Curvature
Smoothing	High
Minimum Cell Size	1 mm
Max Face Size	250 mm
Max Size	250 mm
Growth Rate	1.2

The first parameter listed, the advanced sizing function, defines how the meshing algorithm handles meshing surfaces. The "proximity and curvature" option is the most suitable for the majority of CFD applications because the element sizing is based off of both the proximity of nearby surfaces and the curvature of the current surface. This provides the most accurate meshing for geometric bodies for nearly all cases.

In ANSYS Meshing, mesh smoothing is accomplished by moving node locations relative to surrounding nodes to achieve a higher quality mesh. The option is set to "High" to attain maximum smoothing. This increases the mesh generation time but improves the overall quality.

The minimum and maximum cell sizes are somewhat self-explanatory, being the minimum and maximum element edge lengths through the domain. There is an additional, unlisted property that is used by the advanced sizing function known as proximity minimum size. It is used by the advanced sizing function in locations where the nearness of other surfaces interferes with the default sizing. This setting is not used, however, as it is overridden by the minimum cell size setting, which has a smaller magnitude.

The purpose of the growth rate parameter can also be inferred from its name, it is the maximum growth rate allowed between elements. A growth rate of 1.2 indicates that a cell (when moving away from refined areas) can be no more than 20% larger than the previous cell.

Mesh Refinement

After global parameters were defined, the next step in the meshing process was determining regions of the control volume that required additional refinement to sufficiently and accurately resolve features of the flow. In the free stream region, elements that are large in comparison to the length scale (e.g. 1/4 body length) are not non-contributing to solution accuracy because there is little change in flow properties far away from the body. However, as one approaches a solid boundary within the domain significant changes in flow properties begin to occur. Indeed, as the point of inspection nears complex solid structures, property gradients can become very sharp, producing rapid local changes.

Due to the nature of interpolation, attempting to calculate a cell face value of that property from a cell center value in the presence of a large gradient can result in a highly inaccurate approximation if the distance of interpolation is too great. The solution to this is simply to reduce element size near solid boundaries. Adequate solid boundary resolution is the primary objective of adding mesh refinement zones.

Three refinement regions, or “bodies of influence” (as termed by ANSYS Meshing), were identified and created: an exterior region, an under-body region, and a wake region. Figure 3.3 depicts a side view of the Ahmed geometry modeled in Design Modeler, along with the refinement regions added to assist with meshing in ANSYS Meshing.

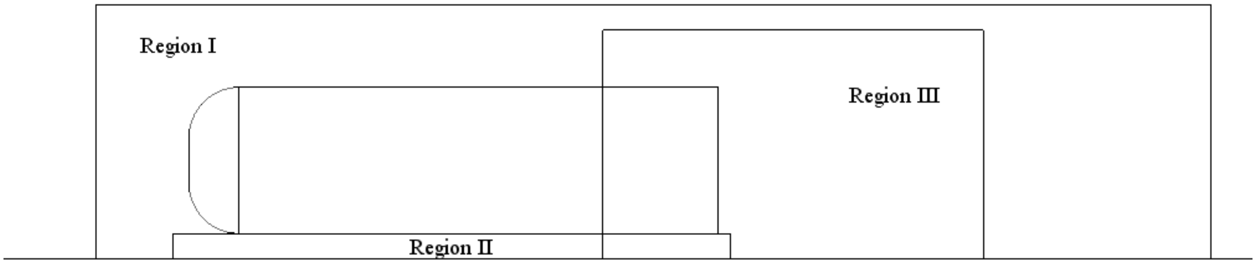

Figure 3.3: Ahmed model refinement side view

Region I, the exterior region, encapsulates the entirety of the Ahmed body as well as a buffer area around the body and the other two refinement zones. The primary purpose of this region was to tighten the meshing parameters in the immediate vicinity of the body. The under body region, Region II, encloses the area between the body and the solid surface at the bottom of the domain, referred to as the “road.” This zone was added for two reasons: the space between the road and the body is 50 mm– much smaller than the global sizing parameters– and because the presence of cylinders (legs) complicates the flow. These geometric constraints require finer meshing constraints than those imposed by Region I to preserve the integrity of the flow properties in this region.

The wake zone, Region III, was the final refinement zone applied to this model. This region was selected for tighter meshing because the wake generated in the volume immediately behind the model is very turbulent, thus additional refinement is required not only to maintain solution fidelity, but also to resolve the features of the flow for examination and analysis.

In addition to parameterized volumetric meshing zones, finer constraints were also imposed on the body surfaces. With ANSYS Meshing, these element size restrictions are known as ”Face Sizes,” which define a preferred element size on 2D surfaces. Again, the simplicity of the Ahmed body was advantageous: only two additional sizings were required, body faces and leg faces. The body faces sizing is inclusive of all the faces on the Ahmed body. Due to the smaller stature of the Ahmed body legs, an additional, reduced parameter was specified for the leg faces only.

Table 3.2 lists the baseline preferred element size for the three volumetric sizings and the two surface refinements. As discussed in Sec. 3.4, these parameters were not fixed for every test case, they were varied to determine the reduction or improvement in simulation accuracy in order to determine the ideal level of refinement.

Table 3.2: Ahmed body mesh refinement parameters

Location	**Preferred Size (mm)**
Region Sizing	
Exterior	30
Under body	15
Wake	20
Face Sizing	
Body	10
Legs	2

The term “preferred size” is used because settings are not hard-coded sizes. The ICEM algorithm will attempt to make elements approximately the specified size, but cannot always match the desired size and will adjust as needed. In most cases ICEM accomplishes meshing regions such as this using smaller elements, down to the specified minimum size.

Using the element sizing parameters listed in Table 3.2 generated a mesh of approximately 1.4 million elements. The average element skewness was approximately 0.22: indicating excellent overall quality (referring to the guidelines presented in Sec. 2.4). The histogram in Fig. 3.4 shows the worst quality elements, those above 0.80 skewness. There were 23 elements out of 1405005 total that had a skewness above 0.80, nineteen 4-node tetrahedrons and four 6-node linear wedges (prisms). Of these elements, the maximum skewness was 0.845, which is well below the acceptable maximum of 0.90. Overall, these parameters provided a high quality mesh that did not contain an overabundance of elements and, thus, were chosen as the baseline for multi-body simulations.

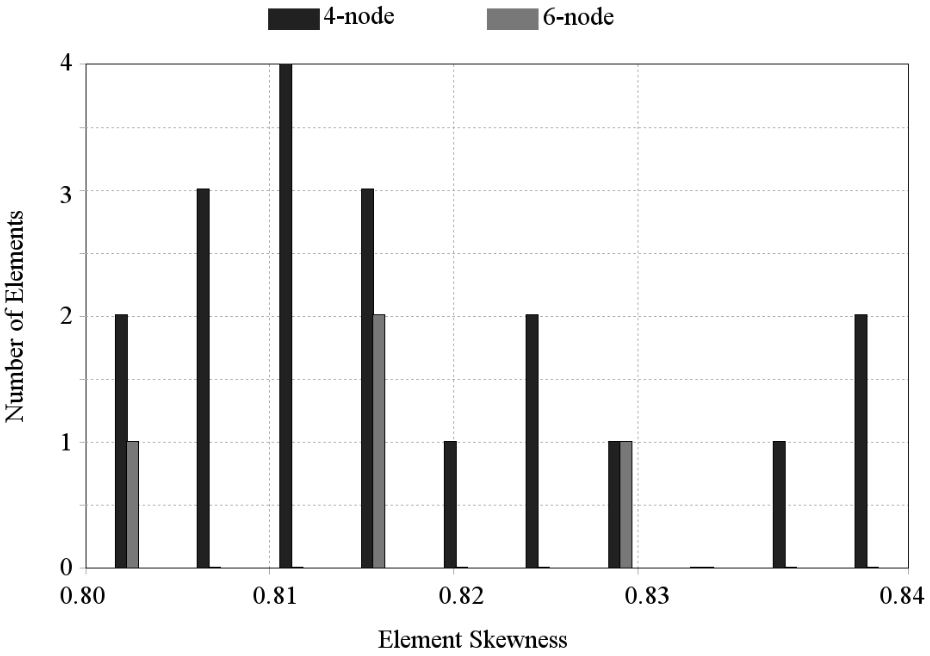

Figure 3.4: Ahmed body maximum skewness histogram

Inflation Layers

A second type of refinement added to all solid surfaces (including the road surface) was an inflation layer. Inflation layers are semi-structured layers of quadrilateral, prismatic elements that are extruded normally from a surface. They are added in order to more accurately resolve the near-surface flow for reasons discussed in Sec. 2.4 because they capture geometry in a superior manner to an unstructured approach. Figure 3.5 illustrates the use of inflation layers on the Ahmed body.

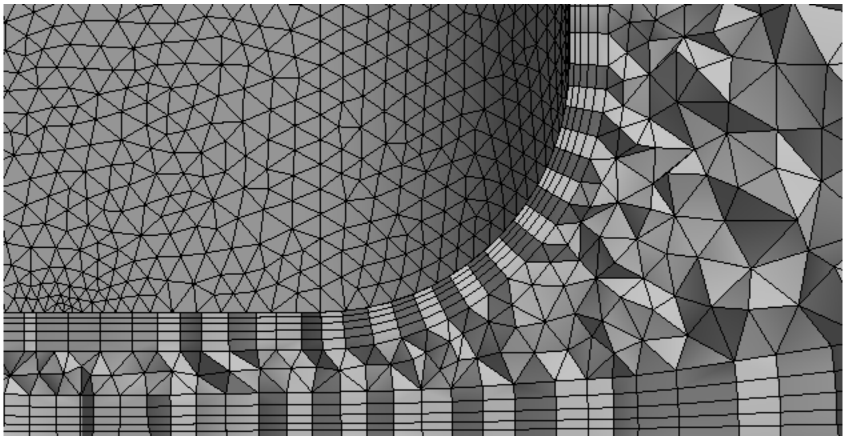

Figure 3.5: Ahmed body inflation layer

The values used for determining inflation layer parameters were gathered from the Best Practices guidelines for Automotive External Aerodynamics in FLUENT [35] and are summarized in Table 3.3. The inflation method used was the “First Aspect Ratio” option, in which the aspect ratio (length:width) of the wall adjacent cell is specified and inflation layer is fixed using the inputs of growth ratio and maximum layers. As per [35], these parameters were chosen because they minimize the volumetric size gradient during the transition from prismatic to tetrahedral elements.

Table 3.3: Ahmed body inflation layer settings

Parameter	**Value**
First Aspect Ratio	5
Maximum Layers	5
Growth Rate	1.20

3.3 Simulation

The parameters used for the Fluent simulation of the flow field around the Ahmed body are discussed in this section. The theoretical background and underpinnings of the methods and parameters addressed here are developed in Secs. 2.2–2.3.

Solution Methods, Controls, & Tolerance

There was no deviation from the solution methods discussed in Chapter 2 and they are summarized below in Table 3.4. All solution methods remained the same for transient analysis, except the momentum discretization, as noted.

Table 3.4: Ahmed body solution methods

Parameter	**Method**
Pressure-Velocity Coupling	Coupled
Pressure	Standard
Momentum	Second Order Upwind (SOU)
Turbulent Kinetic Energy	SOU
Turbulent Dissipation Rate	SOU
Transient Analysis	
Momentum	Bounded Central Differencing
Transient Formulation	Bounded Second Order Implicit

The solution controls (i.e. the relaxation parameters) used for the simulation are shown below in Table 3.5. These factors were kept constant for both single body and multi-body simulations so that the results were as comparable as possible. A relaxation factor of one represents no change to the quantity throughout the solution process. Conversely, the lower the factor the more relaxed the variable, increasing convergence time but assisting in numeric stability. Low factors are used to counter highly non-linear effects.

Table 3.5: Ahmed body solution controls

Parameter	**Value**
Courant Number	50
Explicit Relaxation Factors	
Momentum	0.25
Pressure	0.25
Implicit Relaxation Factors	
Density	1
Body Forces	1
Turbulent Kinetic Energy	0.8
Turbulent Dissipation Rate	0.8
Turbulent Viscosity	0.95

An important annotation that should be made is that the Courant number, momentum, and pressure relaxation factors are significantly lower than the Fluent default parameters (200, 0.75, and 0.75 respectively). These defaults cause the solver to have trouble with high skewness meshes because they directly impact the transported quantities, translating to a potential numerical divergence. Thus the parameters were reduced to account for the fact that there will be poor quality regions in the mesh due to the bluff nature and complexity of the geometry.

For steady state solution convergence, no explicit convergence tolerances were applied, instead the solution convergence was judged to be converged when the drag force (the parameter of interest) remained constant (to 5 significant digits) for at least 100 solution iterations. This indicates a residual tolerance of 10^{-5}. This residual was chosen over traditional residual (such as continuity) monitoring because the parameter of interest was force. The continuity residual for example, does not directly indicate the convergence of the forces within the model (though it is correlated) and even at 10^{-4} continuity residual, the drag coefficient could still be in flux.

Boundary Conditions

Four types of boundaries were employed to simulate a highway environment: inlet, outlet, symmetry, and walls.

An inlet, as one would expect, is a mass inflow boundary, where mass enters the control volume (CV). There are several ways to define the mass flux entering the CV, but because the flow is incompressible the necessary input can be simplified to a velocity vector and any transported turbulence variables (k and ε in this case). For the work herein, this is convenient because the highway velocity magnitude and direction are prescribed quantities.

Contrarily, an outlet is a boundary where mass is expected to flow out of the domain. The type of outlet used for all simulations in this research is a pressure outlet. For a pressure outlet only a static gauge pressure must be specified. Because the flow outlet is far enough away from the body to once again be considered the free stream, a gauge pressure of zero (atmospheric) can be used.

A wall boundary presents a physical surface in the flow. For these simulations both the bottom surface, the "road," and the model body were treated as walls. A wall is rigorously defined in a flow via two conditions: matter cannot penetrate the boundary and the tangential relative velocity component at the surface is zero. The second condition is known as the "no-slip" condition, as it states that a viscous fluid at a solid surface cannot "slip" along (i.e. move relative to) a stationary wall.

A symmetry boundary is typically used to represent planes of symmetry within a flow, but can also be used as a far-field boundary. Mathematically, a symmetry boundary is represented as a slip wall– a solid boundary that the flow cannot cross the where the zero velocity condition is not enforced, but rather a zero shear condition. The far-field boundaries represented by a symmetry plane were the upper boundary (the “roof”) and the domain boundaries parallel to the model (i.e. the sides).

Reference Parameters

There are three reference parameters that were used for producing the drag coefficient C_D from the drag force F_D: free stream velocity, free stream density, and cross sectional area. Equation (3.1), which is a restatement of Eq. (2.1), shows the relationship between force, drag coefficient, and the reference parameters.

$$F_D = \frac{1}{2} C_D \rho_\infty v_\infty^2 A \tag{3.1}$$

The free stream velocity, v_∞, used for all simulations was $v_\infty = 30$ m/s, or 67.1 miles per hour (mph), which is approximately the typical highway speed of a tractor-trailer. This is somewhat at odds with Ahmed’s wind tunnel tests, which were run at 40 m/s [13]. Though the simulation and wind tunnel speeds are different, the coefficient of drag results can be compared effectively because, by definition, C_D is nondimensionalized by the free stream velocity and is thus independent of air speed by the principles of similarity. This is indeed confirmed by the results discussed in the following section, Sec. 3.4.

The free stream density, ρ_∞, used was $\rho_\infty = 1.225$ kg/m^3, which is the standard sea level air density. Again, due to similarity the density can be varied and the resulting drag coefficient can be accurately compared.

The cross sectional reference area used was 0.115032 m^2, as previously discussed in Sec. 3.1. This area is the projected frontal cross section; to which the drag force is directly proportional. This effect can be intuitively observed: a dart, which has a low frontal cross section to overall surface area ratio, is more aerodynamic than a brick, which has a very large cross section to surface area ratio.

3.4 Results

Beyond the baseline calculated for simulation validation and multi-body comparison, two additional results were computed: mesh size and turbulence model effect. For the mesh size trial the sizing parameters were varied and the solution accuracy was compared to the wind tunnel result. Secondly, the turbulence model changed from the primary RKE model to the ancillary DES model to examine the effects on solution accuracy.

3.4.1 Baseline Model

Shown below in Fig. 3.6 are the velocity magnitude, pressure distribution, wake vorticity magnitude, and streamline flow profiles for the single Ahmed body simulation.

The resultant drag coefficient was 0.26150, which is a 4.6% relative error from the wind tunnel value of 0.25 [13]. An error of less than 5% was considered acceptable for 1.4M mesh elements, particularly considering the steady state assumption and use of the RKE turbulence model. Thus, the baseline meshing parameters discussed above were used for all Ahmed body simulations.

The pressure profile presented by Fig. 3.6a provides a visualization of the forces the body experiences due to pressure. There is significant pressure force acting parallel to the free stream (the direction of interest) on both the front and rear faces of the body. The front face experiences a very large "pushing" pressure increase at the stagnation point (location of zero velocity), near the nose. As one inspects further away from the the nose, the pressure drops and even becomes lower than gauge pressure, which is "pulling" on the vehicle. In fact, the low presure at the top of the front face is approximately equivalent to the high pressure at the stagnation zone. However, while the high pressure regions exerts a large amount of hindering force on the body because of the orthogonality of the nose, the helpfulness of the low pressure region is limited because the body is sloped away near the top surface. The change in geometry alters the force vector on the surface so that it is mostly in the transverse direction, (i.e. lift) minimizing the drag reduction effect.

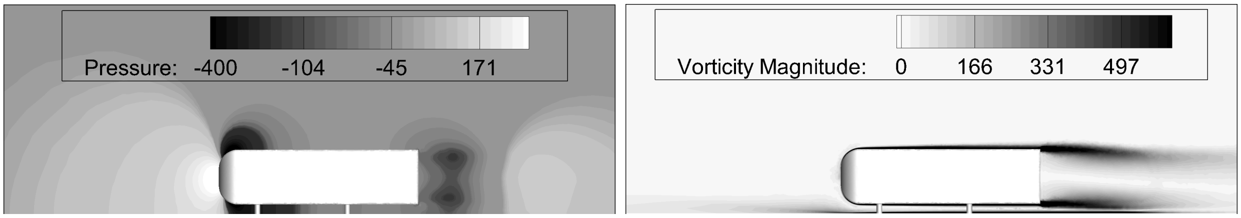

(a) Pressure distribution (b) Wake vorticity magnitude

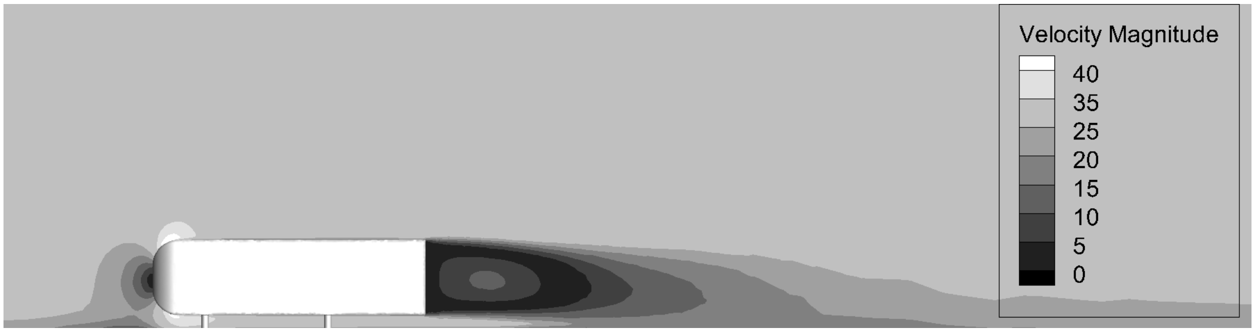

(c) Velocity magnitude

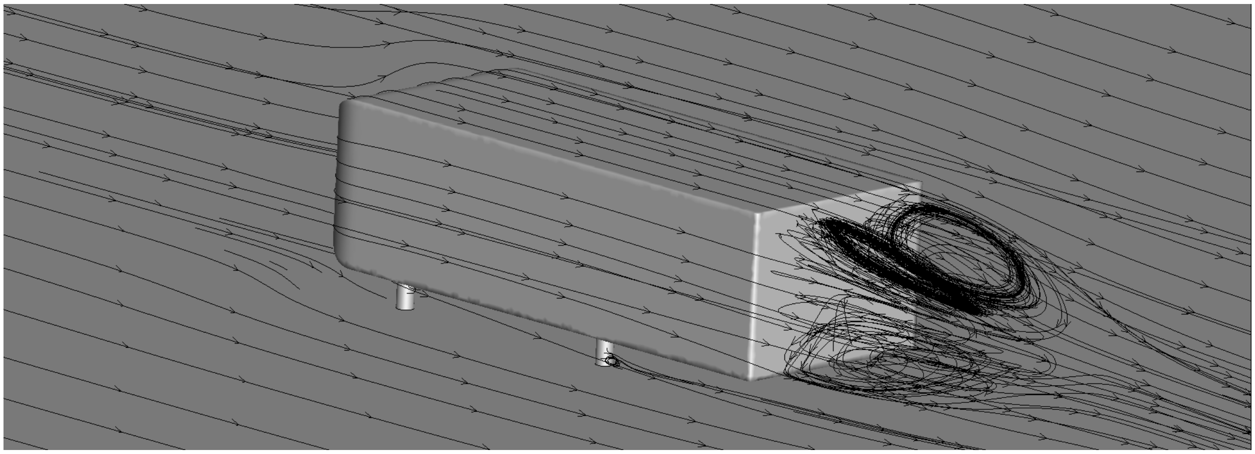

(d) Streamlines

Figure 3.6: Single Ahmed body property profiles

The pressure profile on the rear face is less complex: there is a low pressure region that is once again exerting a net outward force ("pulling") on the body, as was seen on the outer region of the front face. In this case however, the force is actually increasing the drag instead of decreasing as it is on the front of the body, where the surface normal vector is in the drag direction.

On the side faces of the body there is no drag pressure force as the normal vector on these surfaces is entirely in the lift direction. There is, however, viscous (skin) drag that occurs on these surfaces. Though not insignificant, skin drag does not contribute as much to the overall drag force as pressure, being approximately 10-20% of the total drag on the Ahmed body.

Examining the velocity profile presented in Fig. 3.6c confirms much of the pressure force discussion above. Applying Bernoulli's principle for incompressible flow shows that at the stagnation point, the highest pressure region exists. Similarly, as the flow accelerates to circulate around the body, the pressure decreases.

Figure 3.6c also describes the wake behind the vehicle: it shows that there is a single region encapsulating all the rotation immediately behind the vehicle. The overall velocity magnitude is greatly reduced in this region because it is highly non-directed due to the flow rotationality and the abrupt end of the body.

Considering the streamlines shown in Fig. 3.6d in conjunction with the vorticity information presented by Fig. 3.6b allows for a more detailed analysis of the flow structure behind the Ahmed body. The 3D perspective shows that within the macro-vortex there are four sub-vortices, formed from each corner of the body.

Using the vorticity information provided by Fig. 3.6b shows that immediately after the flow reaches the end of the Ahmed body, it expands into the now empty space by recirculating back, translating energy into a rotational form and resulting in a pressure decrease. The formation of this vortex therefore directly increases the drag on the rear of the vehicle.

3.4.2 Mesh Size

Once a baseline mesh size was established, the effect of mesh size on solution accuracy was examined to gain insight into how large a role mesh fineness plays in the force prediction. This is a useful study because it provides solution accuracy trends for meshing more complex geometries, such as the tractor-trailer model. The size of the mesh was varied from 500k elements to 4.2m elements and Fig. 3.7 shows the drag coefficient C_D vs. the total number of elements in the mesh.

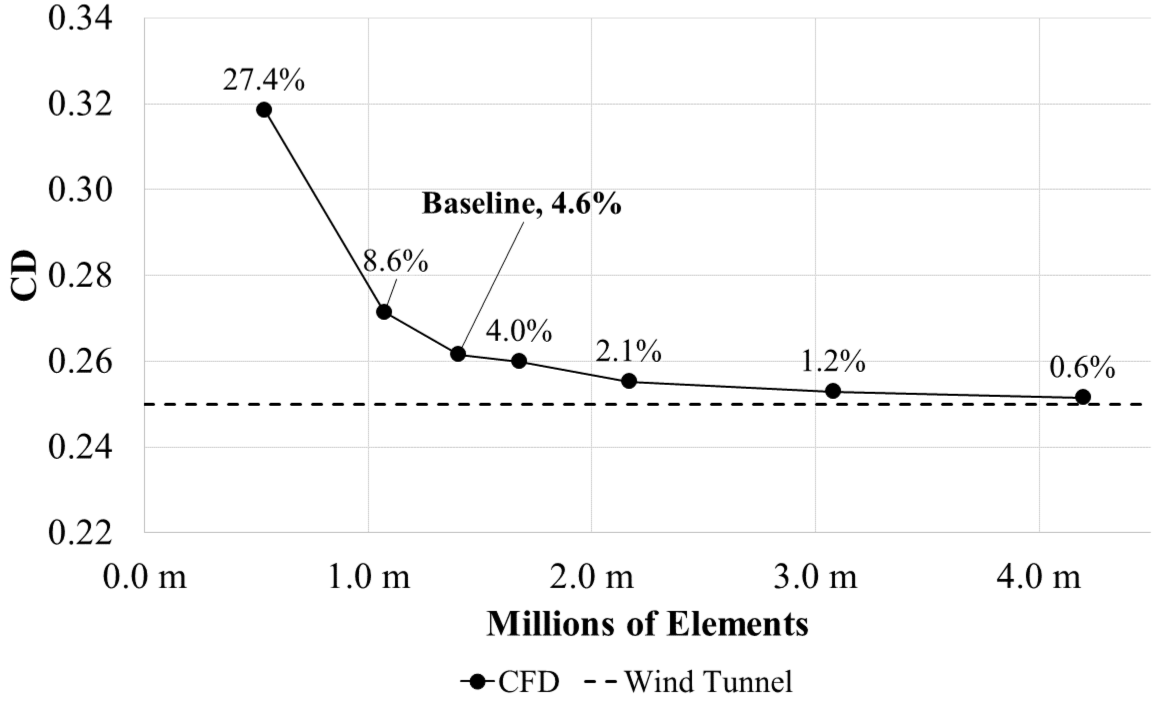

Figure 3.7: Single Ahmed drag vs. millions of elements

The trend that appears is exactly as expected: low element meshes have high errors and high element meshes have lower errors. While the error is extremely large for the lowest quality mesh, it quickly decreases to less than 5% at 1.4M cells. Beyond the baseline case the solution continues to become more accurate, but the marked 600% decrease in error per million elements is not present. Adding 3M elements decreases the error from 4.6% to 0.6%, but comes at the cost of incredibly increased computational resources. While this may be viable for a single body simulation, this level of refinement is simply unfeasible for multi-body simulations as mesh requirements would quickly outpace the hardware resources available.

Though it would be possible to use the more accurate single body simulation for further analysis, this would degrade the results because the lone body and multi-body simulations would no longer be comparable. Thus, to maintain similar solution accuracies across cases, the same baseline meshing parameters were used.

To achieve a reduction or increase in the mesh fineness, the sizing parameters on the refinement regions were proportionally varied. Varying each accordingly in relation to the other meshing parameters allows for a higher fidelity overall solution and does not produce a model that is extremely refined in some locations and poorly meshed in others. Table 3.6 below lists the parameters used to approximately obtain the desired mesh sizes. It is worth noting that the global meshing parameters (e.g. maximum size, growth rate, etc.) were not changed.

Table 3.6: Ahmed body meshing variation

Region	**Preferred Size (mm)**						
				Volumetric Sizing			
Exterior	150	40	30	30	25	23	23
Under	50	17	15	15	13	11	10
Wake	50	17	20	15	13	11	10
				Surface Sizing			
Legs	10	6	2	2	2	1.5	1
Body	50	15	10	10	9	8	7
				Number of Elements			
Total	536305	1071331	1405005	1677941	2167924	3080081	4197331

The global minimum elements size was defined as 1 mm, this was maintained for all simulations excepting the last case where the preferred element size on the legs was already the minimum. In this simulation, the local minimum element size was lowered to 0.5 mm to further increase the mesh quality on the leg surfaces.

Upon examination of Table 3.6, it is apparent that the scaling between refinement size and total mesh size is highly nonlinear. In the case of moving from 536k elements to 1.07M, the body surface zone was reduced from 50 mm to 15 mm, a delta of 35 mm for an increase of 534k. However, in the last case reducing size by 1 mm generated an additional 1.11M elements. This trend is exceedingly important when working with complex geometries where very small elements are required: even a small decrease in sizing can result in millions of additional mesh elements. Extremely large meshes not only take additional computational time but can become unusable due to hardware resource requirements (available RAM).

3.4.3 Turbulence Model

The second avenue of investigation was the use of the purported more accurate Detached Eddy Simulation turbulence model. Table 3.7 lists the resultant drag coefficients from each model. Because the DES solution is time accurate, the drag was averaged across several time steps once a quasi-equilibrium state had been reached. The DES-RKE drag coefficient prediction versus time is shown below in Fig. 3.8.

Table 3.7: Ahmed body turbulence model comparison

Turbulence Model	**Drag**	**Error**
RKE	0.26150	4.6%
DES-RKE	0.23899	4.4%

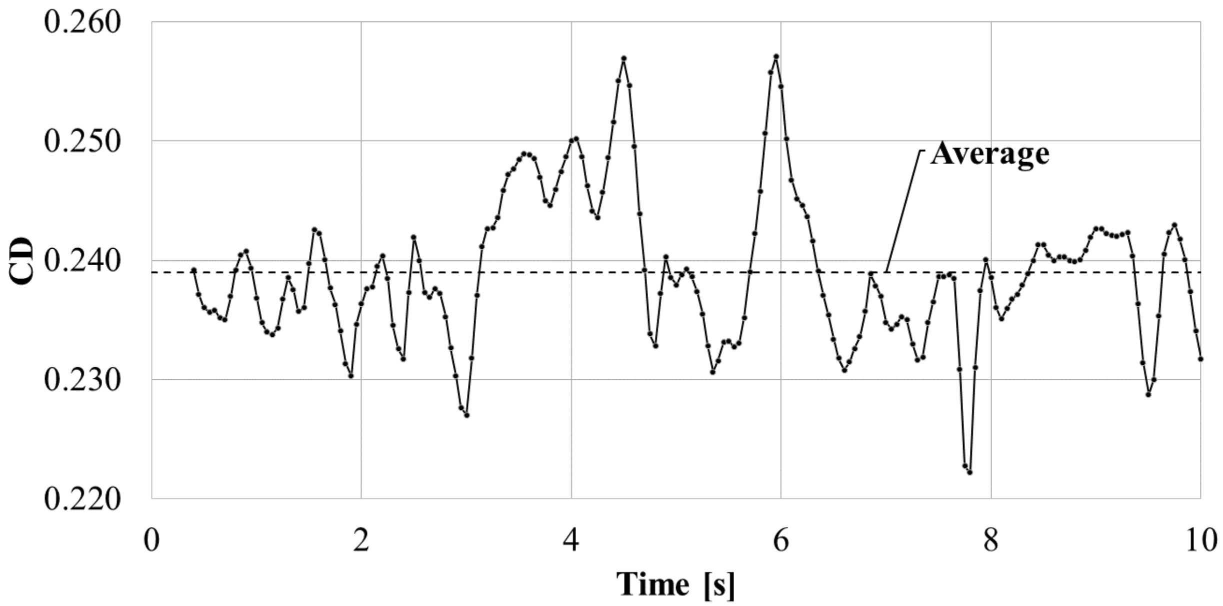

Figure 3.8: Single Ahmed DES-RKE drag vs. time

It is apparent from Table 3.7 that the DES-RKE under-predicts the drag coefficient and has slightly less error than the RANS-based RKE. The trend of drag under-prediction will always occur in a DES simulation because of the transition method from the near-wall RANS model to the far-field LES model. [36] This is a useful fact that is exploited in Sec. 5.2.1.

The reason for reduced error can be gleaned from examination of Fig. 3.8, which shows that the drag coefficient varies in a somewhat sinusoidal pattern as the solution time is progressed. Because of the large variation across time, representing an accurate drag coefficient is somewhat difficult. An arithmetic average was used to calculate the drag.

The large drag deviation between time steps also leads to the conclusion that the small decrease in error is likely statistically insignificant, as the resulting average depends largely on the range of time steps selected. Because there is no indicator of the suitability of a specific time range, such as a cycle completion, the variance becomes very problematic, increasing the uncertainty related to the average drag coefficient.

Figure 3.9 gives understanding into why the DES-RKE model under-predicts drag, which was a trend that was not present in the previously-examined RKE model. Figure 3.9 is a side-by-side comparison of the velocity magnitude profiles for both the RKE and the DES-RKE turbulence models. It is important to keep in mind that because DES is a transient model, Fig. 3.9b is only a snapshot of a particular time step, the flow at 5.00 s. This does not negate the comparison though, as the resolved structure remains approximately constant across time.

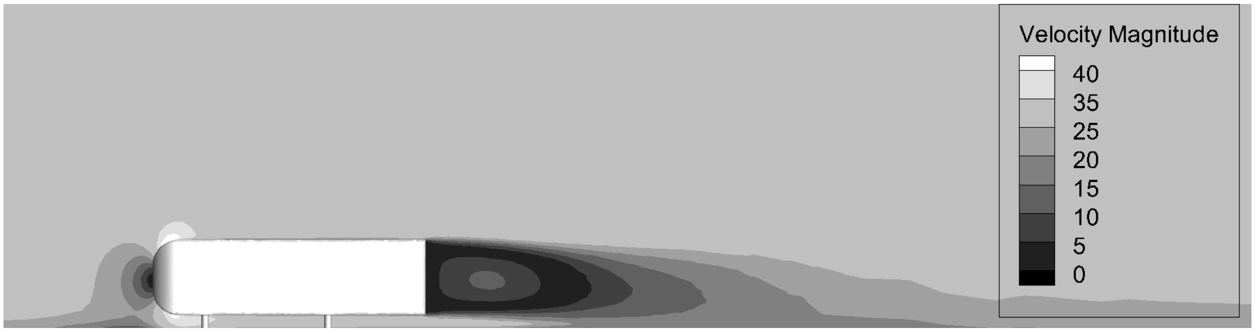

(a) RKE velocity magnitude profile

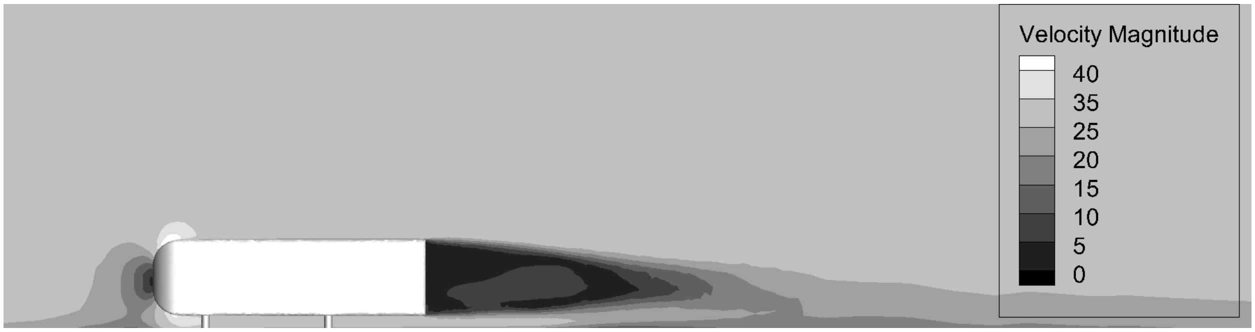

(b) DES-RKE velocity magnitude profile

Figure 3.9: Pressure distribution

When examining the profiles presented by Fig. 3.9 the reason that the DES-RKE model is under-predicting drag force becomes clear. In the RKE model, the vortex behind the body is compact and stable; the DES-RKE vortex, on the other hand, is much more elongated and less defined. Other than this, the profiles are near identical. This is indicative that the DES-RKE model is under-predicting the pressure force on the rear surface of the vehicle while the RKE turbulence model is over-predicting, thus leading to the difference in overall drag coefficients.

These results led to the conclusion that while the DES-RKE tuburlence model offers approximately the same level of accuracy as the RANS-based RKE, the extreme increase in computational time required and large variance in drag estimates make the model too unreliable to be used as the primary model. This rationale is further enforced by the results of Kapadia [37], where using a DES turbulence model resulted in large discrepancies and disagreements between body force results.

3.5 Two Ahmed Body Model

After the development and simulation of the single Ahmed body, a two body model was developed. This model was developed for two primary reasons: validation against wind tunnel data [18] and drag trend information.

The methodology, parameters, and settings used for developing the two body mesh and simulation were identical to those discussed in Sec. 3.2 and Sec. 3.3. This was done to preserve the level of solution fidelity and allow a comparison of two body results to the single body drag prediction.

The two Ahmed body simulation was ran at a variety of distances from 0.05 m to 2 m, which corresponds to values ranging 5% and 200% body length referring to a reference length of approximately one meter. Table 3.8 shows a comprehensive list of all the distances simulated.

Table 3.8: Ahmed body turbulence model comparison

Seperation Distance (m)	**Percent Body Length**
0.05	5%
0.15	15%
0.25	25%
0.50	50%
1.00	100%
1.50	150%
2.00	200%

3.5.1 Overall Drag Prediction

The drag coefficient predicted by Fluent for each vehicle is shown Fig. 3.10, along with the single body drag and net drag per body (the average drag) coefficients. Note that despite the fact there is a rear body drag increase in many cases, the average drag is always lower than the single body drag (i.e. vehicles always experience a net benefit from platooning).

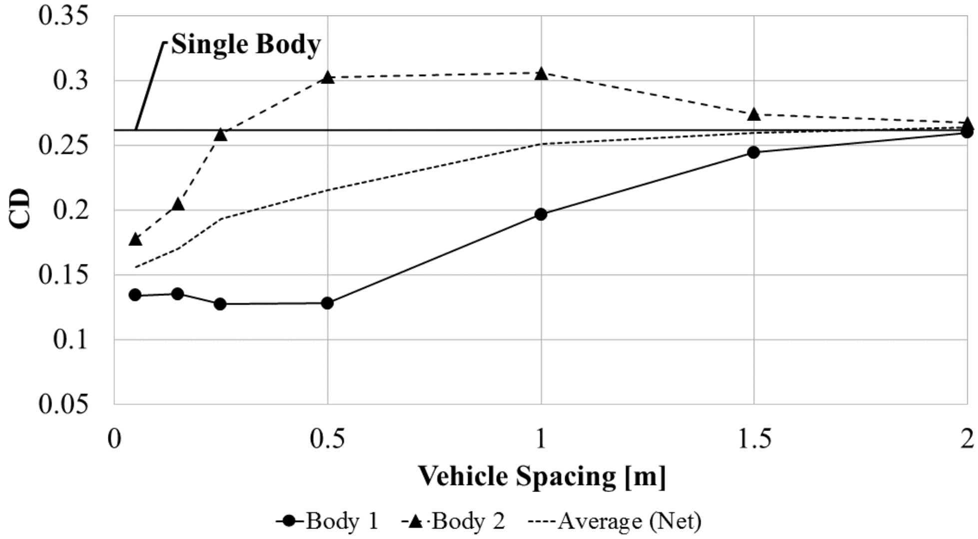

Figure 3.10: Total drag coefficient by vehicle

The results are immediately suspect, as it appears from Fig. 3.10 that platooning actually increases the drag the second vehicle experiences until very close following distances (less than 0.25 body length). However, upon comparison to the wind tunnel data provided in [18], it is clear that this trend is indeed correct. To compare the wind tunnel and simulation data, the simulation results (CFD) in Fig. 3.10 are normalized and compared to the wind tunnel results (WT) in Fig. 3.11. The normalization value for the wind tunnel tests was the single body wind tunnel drag and likewise for the CFD results, the normalization factor was the single body simulated drag. A normalized value of one represents no increase or decrease in drag.

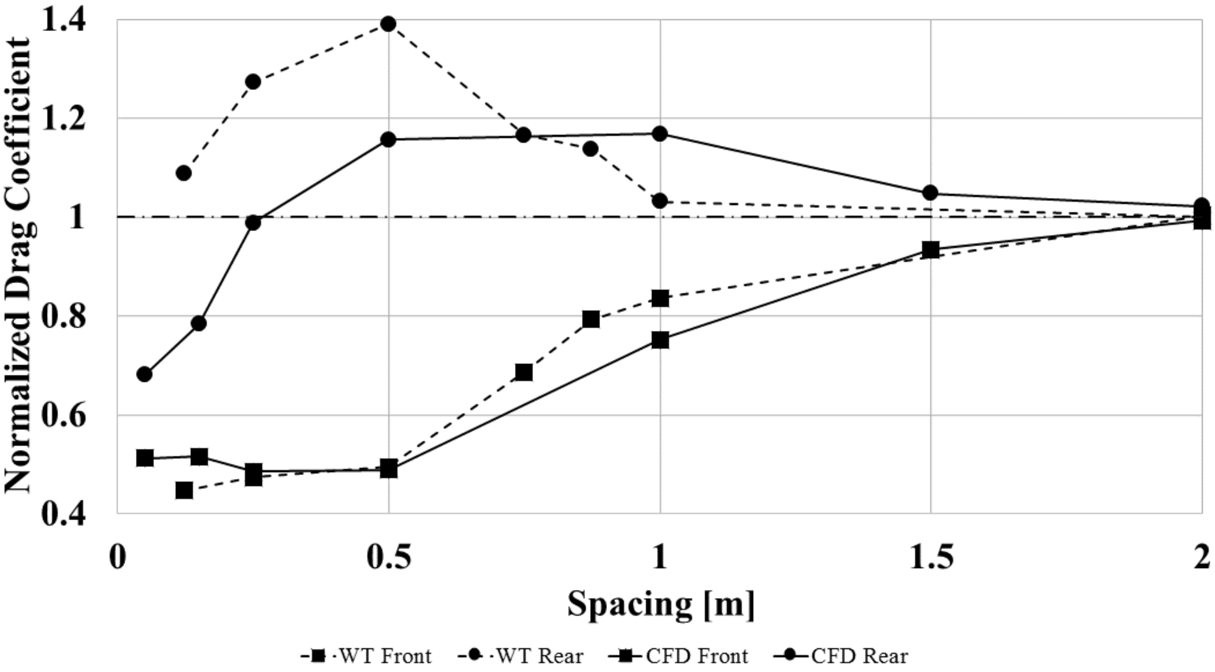

Figure 3.11: Normalized slanted wind tunnel data vs. no slant CFD Comparison

Though the second body does see increased total drag in most cases, the overall result is a decrease in net drag for all cases simulated, as can be seen by the averaged line in Fig. 3.10. This is because the increase in drag on the second body is always less than 20% whereas the decrease in drag on the front body can be as much as 50%. This form of net drag reduction is advantageous but not always desirable. For example: if a platoon of two tractor-trailers from different fleets experience this effect, there would be overall fuel savings but the follow vehicle (from Fleet 2) would see an increase in fuel consumption, resulting in increased cost for Fleet 2 and decreased cost for Fleet 1. This situation does not benefit Fleet 2 and thus the Fleet 2 tractor would be unlikely to platoon with Fleet 1 if it were to be the follow vehicle. This effect is addressed in Sec. 5.4, where multiple vehicle geometries are examined.

Notice that results of Fig. 3.11 do not agree numerically, only qualitatively. This is due to the fact that the wind tunnel tests performed by Pagliarella were conducted on bodies with slant angles, whereas the simulations performed examined only models with no rear slant. The data shown in Fig. 3.11 is from a suite of tests where the slant configuration was 35°angles for both bodies.

Pagliarella, in fact, sees a larger increase in drag on the trailing body than the simulation predicts. This is not a discrepancy between the simulation and wind tunnel results, but likely due to the aforementioned slant angle difference. Because the flow is low speed, the gradual decrease in cross-sectional area draws the flow downward forming a much smaller, tighter vortex structure and overall lower flow disturbance. The opposite is true for the zero angle body where the sudden end of the body creates a recirculation of the flow, resulting in a larger and more chaotic vortex pattern in the vehicle wake. The consequence of this difference in flow structure is a less directed, lower velocity flow behind the zero slant body, creating a more conducive drag reduction environment for the following vehicle.

Figure 3.12 below shows the numerical results of Luminari for a slanted body [38] side-by-side with results generated herein to view the stark difference in flow structure behind each body.

3.5.2 Surface Drag Comparison

Though the additional drag reduction provided by a no slant vehicle reduces the drag force the second body experiences, it does not lead to the desired outcome of less drag than a single body. To examine why the second body experiences increased drag, the drag force

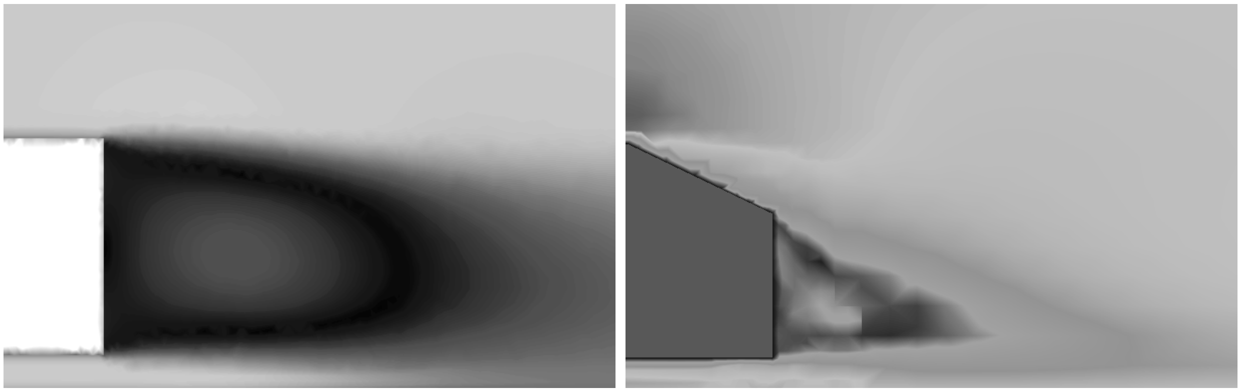

(a) No slant (b) Slant

Figure 3.12: Effect of rear slant on vehicle wake

on each surface of the body was investigated. The results for each body, lead and follow, are shown in Fig. 3.13.

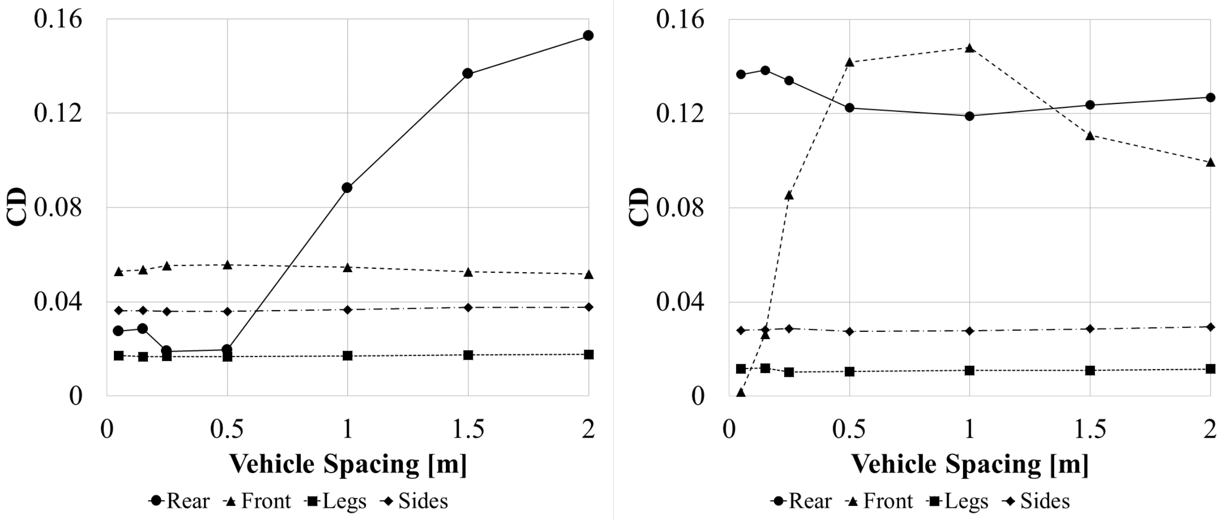

(a) Lead body (b) Follow body

Figure 3.13: Pressure force by surface

Several important conclusions can be drawn from Fig. 3.13. Firstly, it is evident that the lead body in the 2 m separation case can effectively be treated as a single body. Inspecting this test shows that for a single Ahmed body, the rear surface pressure force (wake drag) is the largest contributor to overall drag by a factor of three. Therefore impacting the wake drag is the easiest way to achieve significant drag savings on the Ahmed body.

Secondly, the each body has three surface forces that remain approximately constant. The side and leg forces are common between them and do not significantly change. The third constant surface differs: for the lead vehicle the front surface force remains constant, for the follow the constant force is on the rear surface. The rear surface on the follow vehicle does have more variance than the leg and side forces, but the deviation is very minimal when compared with the change in frontal surface force.

This leads to the final conclusion: only a single surface on each body experiences considerable changes. The variant surface is the rear face on the lead body and the frontal face on the follow body. This essentially states that the region of influence of each vehicle is limited to the closest surface of its fellow body.

Rear Surface Drag Comparison

Isolating and combining the rear surface pressure information presented in Fig. 3.13 produced Fig. 3.14, which is normalized as a percentage of the single body drag. This was done to better present the drag reduction achieved by each body due to the platooning effects.

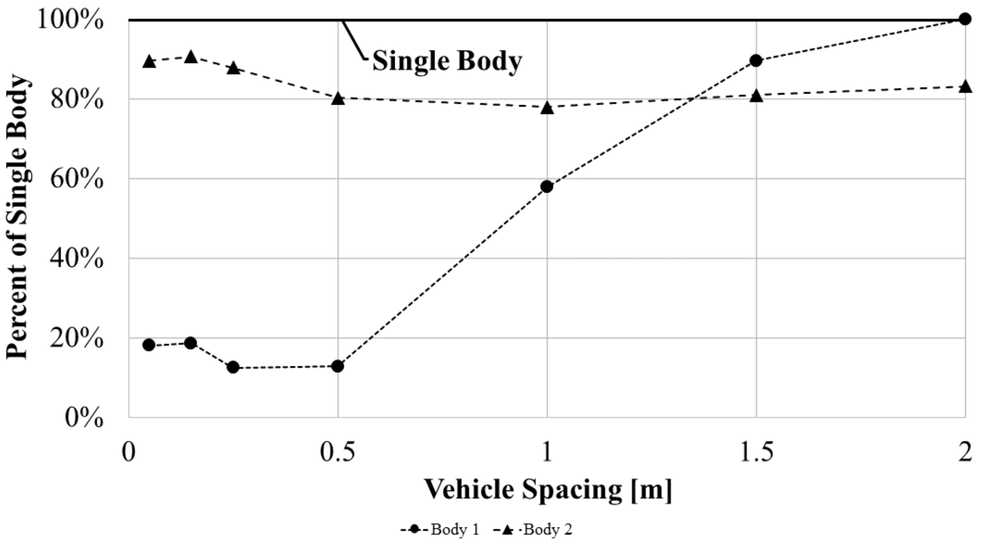

Figure 3.14: Rear surface force comparison

Inspecting the rear surface drag reveals that there is approximately a 20% decrease in rear drag due to the lower effective free stream velocity and that remains almost constant, seeing only a slight rise at very close distances. This indicates that while the follower wake drag reduction is nearly independent of vehicle spacing, the presence of a frontal vehicle allows for a base reduction in wake drag.

Analyzing the rear surface drag on the lead vehicle shows that it decreases greatly as the distance between bodies decreases. Because the rear surface pressure drag is such a large contributor to the overall drag, this reduction results in a massive decrease in drag coefficient. This suggests that for geometries where the wake drag does not intensely dominate the pressure forces, the overall drag reduction would decrease due to the limited zone of influence of the following body.

Front Surface Drag Comparison

Again using the data from Fig. 3.13, Fig. 3.15 was developed. Figure 3.15 is the pressure drag on the frontal surface of each body as a function of vehicle spacing and is normalized in a similar manner to Fig. 3.14.

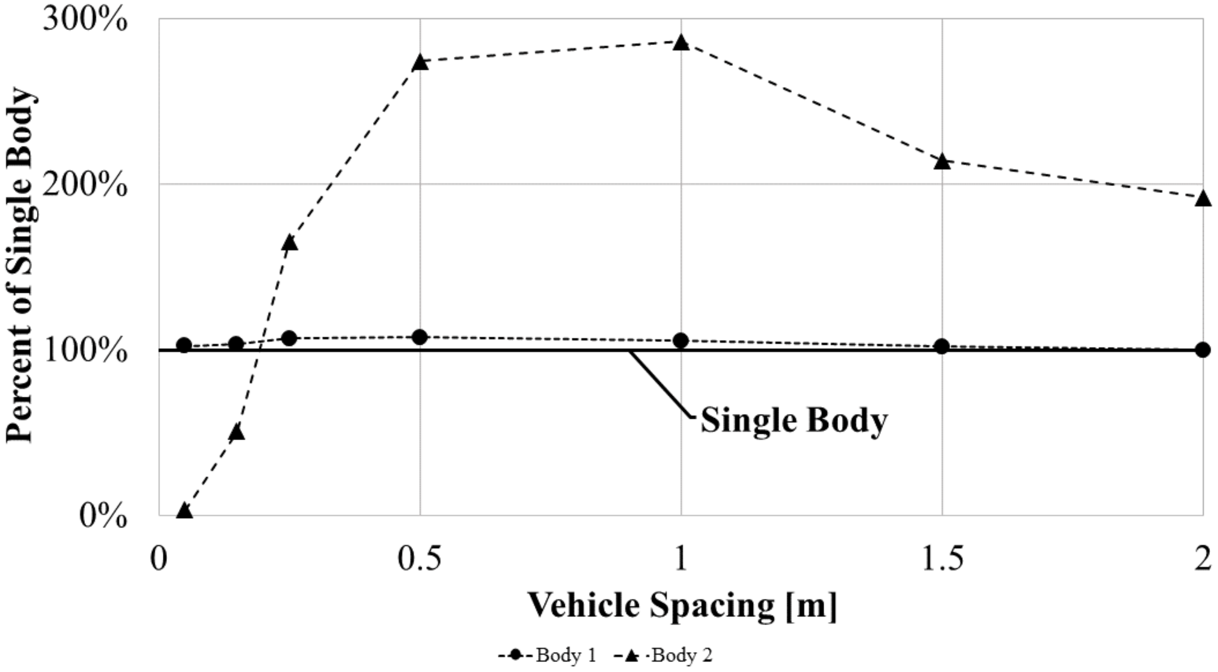

Figure 3.15: Frontal surface force comparison

Figure 3.15 shows that the lead vehicle is essentially unaffected on the front surface. This is as expected; there is no upwind object to affect the flow in front of the lead vehicle. On the front surface of the follower vehicle, however, a large increase from the single body surface drag develops. This is the reason for overall drag coefficient increase: the benefit afforded by the slightly reduced rear surface drag is overcome by the increase in frontal surface pressure. This trend is seen for nearly all spacings, excepting distances closer than 0.25 body lengths, when the follow vehicle frontal drag reduces and even becomes lower than the single body equivalent.

To gain physical understanding of this phenomenon, the frontal pressure distribution and velocity field of both bodies for multiple separation distances were examined, the profiles shown in Fig. 3.16 show the pressure for both the lead and the following vehicle at a separation distance of one meter as well as the velocity field surrounding the bodies. The one body length separation case was chosen because the pressure differential between frontal surfaces is the greatest.

(a) Lead body (b) Follow body

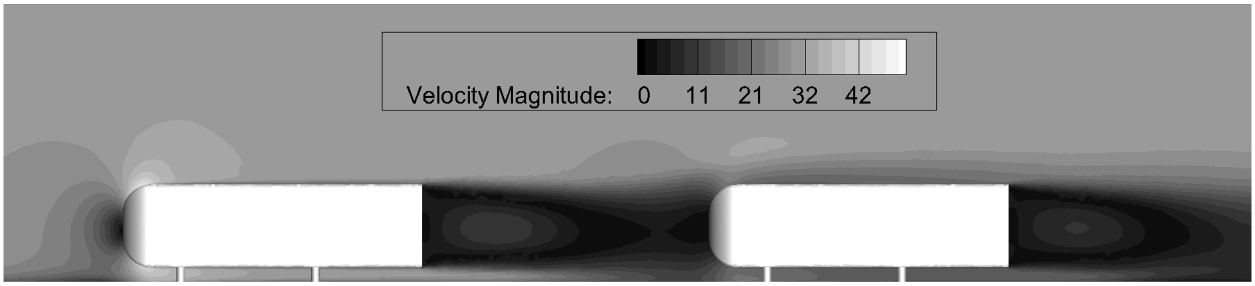

(c) Total drag coefficient by vehicle

Figure 3.16: Pressure distrubution & velocity profile on frontal surfaces for 1 m separation

Upon review of Fig. 3.16 it becomes immediately clear that the surfaces have the same pressure distribution, differing only in magnitude. As indicated by the legend, darker and lighter shadings represent lower and higher pressure distribution, with pure white being very high above gauge pressure and black being much lower than gauge, with reference to one atmosphere.

The pressure on the normal face (the nose) is much higher on the lead body than the follower. The result: more drag force on the nose of the lead than on the follower. This is surprising because it is known from the simulation results that the follow vehicle has a higher frontal force.

The cause of this can be found in the high velocity region. When the flow accelerates around the curved portion of the frontal surface, the pressure drops drastically on both vehicles, as can be seen in Fig. 3.16. The pressure reduction on the lead body, however, is much greater than that on the follow body and, in fact, the transition to negative pressure (below gauge) occurs much closer to the nose. Even though the curved surface has a normal vector that is not primarily in the longitudinal direction, the extremely large pressure gradient on the lead body results in a net lower drag force than on the follow vehicle.

The large pressure gradient can be related to first principles via Bernoulli's equation, which states that pressure is inversely proportional to the square of velocity. This is why the large velocity gradient on the lead body, shown in Fig. 3.16c, leads to an even larger pressure gradient.

Thus it is concluded that the pressure profile and gradient on the frontal surface are extremely important. This is not surprising when considering the fact that the pressure gradient appears directly in the conservation of momentum equation, which is used to calculate body forces.

A second point that can be inferred from these results is that the drag reduction is directly correlated to frontal geometry. It is in fact highly likely that the increase in frontal drag is due largely to the extremely blunt nature of the Ahmed body, suggesting that in real world applications vehicles with more bluff profiles will see less drag reduction or even experience detrimental effects from platooning. This is a significant finding: not all geometries benefit from platooning. This concept is further developed in Sec. 5.4, where simulation data on multiple geometries sheds light on this trend.

Chapter 4

Single Tractor-Trailer

This chapter discusses the development and meshing of the single tractor-trailer models simulated, which were used as a baseline comparison model for the multiple heavy vehicle simulations. Three models were used, each a simplified version of an existing tractor. The basis vehicles used for modeling were: a Peterbilt 579, a Peterbilt 379, and a Mercedes-Benz ACTROS.

4.1 Geometry

As mentioned above, three separate base geometries were used, which are depicted below in Fig. 4.1. Fig. 4.1a shows the primary model, the Peterbilt 579. This model was chosen to be the primary model because two Peterbilt 579 tractors were available for road experiments via the contract awarded through [11].

Fig. 4.1b and Fig. 4.1c show the secondary models, the Peterbilt 379 and Mercedes-Benz ACTROS, respectively. These models were used primarily to examine the influence of geometry on drag reduction potential. The Peterbilt 579 is a modern tractor design with a sloped engine hood and fairing over the tractor cabin. The Peterbilt 379 is an older model, having a classic design with little aerodynamic styling. The final test geometry, the Mercedes-Benz ACTROS is vastly different from the Peterbilt models, it is a flat-nosed, cab-over European-style tractor.

(a) Peterbilt 579 [39]

(b) Peterbilt 379 [40]

(c) Mercedes-Benz ACTROS [41]

Figure 4.1: Tractors Modeled & Simulated

To begin the modeling process, two CAD models were acquired from the CAD community GrabCAD [42]. The original models are shown below in Fig. 4.2a and Fig. 4.2b:

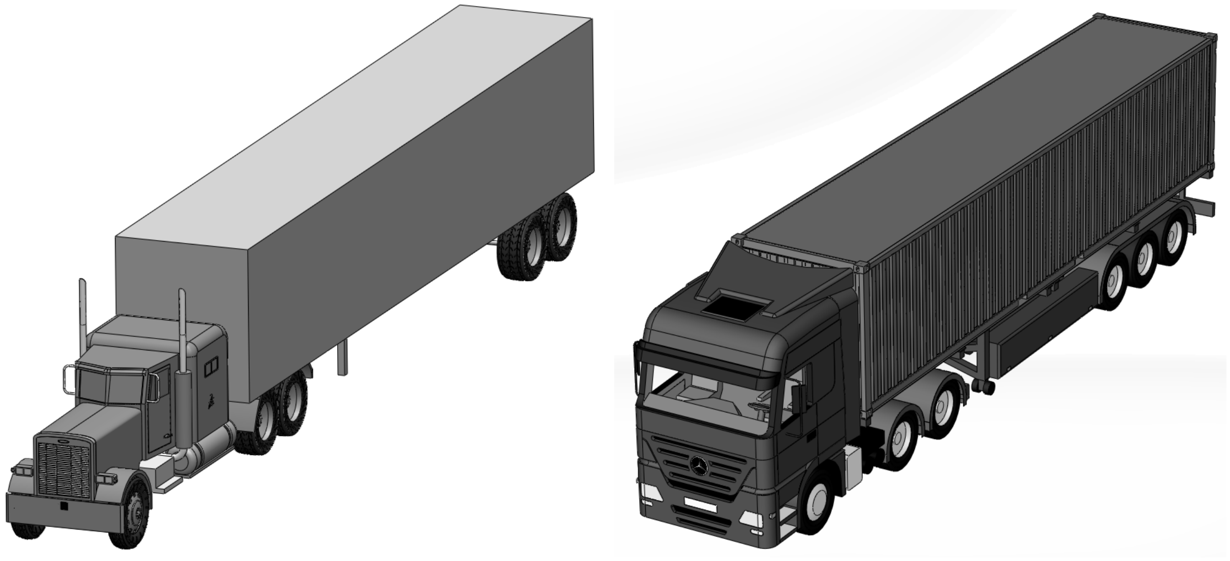

(a) Peterbilt 379 (b) Mercedes-Benz ACTROS

Figure 4.2: Original CAD Models

Both of these CAD models have a very high level of detail; a level that is unnecessary to produce accurate simulation results. In fact, the amount of detail present is actually detrimental to the meshing process, since the finer features requires intensive mesh design often resulting in a very large increase in total numbers of elements. Thus the models above were simplified via a defeaturing process, where features that do not contribute significantly to the overall drag were removed. The resulting simplified versions are the models used for meshing and are shown below in Fig. 4.3:

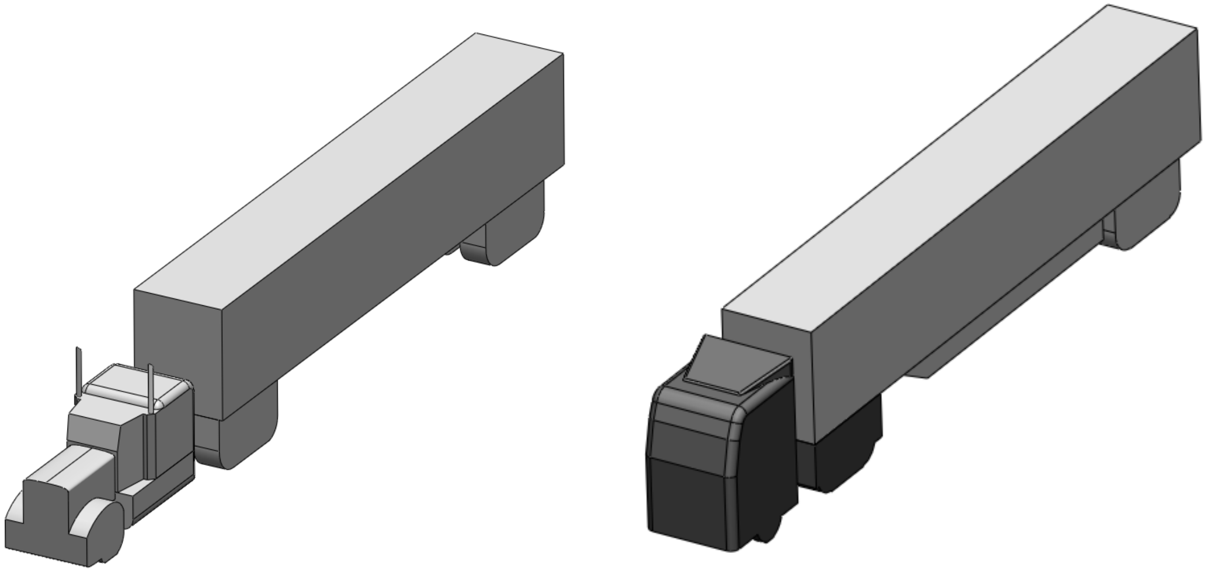

(a) Peterbilt 379 (b) Mercedes-Benz ACTROS

Figure 4.3: Simplified CAD Models

Defeaturing is an important aspect of the meshing process of a complex geometry such as the tractor-trailer mainly because of the length scale disparity between features. Some features, such as side mirrors or windshield overhangs, are proportionately very small when compared to the overall vehicle length, being of the order of 1 ft when the entire length is approximately 70 ft.

The parameters that are necessary to generate a quality mesh around these diminutive features will also cause the number of elements to grow exponentially, as was seen in Sec. 3.4.2 where a small change in element size caused an extremely large increase in cells at highly refined levels. When compounded by the fact that there are several of these features, the mesh size can quickly get out of hand and become several millions elements per vehicle. If time and finite computing resources were not factors in modeling, then multi-vehicle meshes of these sizes could be viable. However, because this is not the case and an over-refined mesh provides minimally better results than its less-refined counterpart (as discussed in Sec. 3.4.2), it is not feasible to simulate a full, non-simplified tractor-trailer geometry.

As alluded to above, features that were candidates for removal were components that were highly detailed and changed the flow locally, but did not affect the overall aerodynamic profile. This included features such as (but not limited to): side mirrors, wind shield overhangs, tractor grills, wheel detail, window cutouts, headlamps, etc.

Conversely, there are some small features that do have significant impact on the flow and are highly nontrivial. The windshield of the Peterbilt 359, for example, is only 2 ft in length, but the slope greatly affects the flow on the entire upper tractor and must be included in analysis, despite the additional elements generated.

After defeaturing had been completed, the simplified Peterbilt 379 was modified to the profile of the road test vehicle, the Peterbilt 579. The resulting CAD was the primary test model for simulations and is shown below in Fig. 4.4.

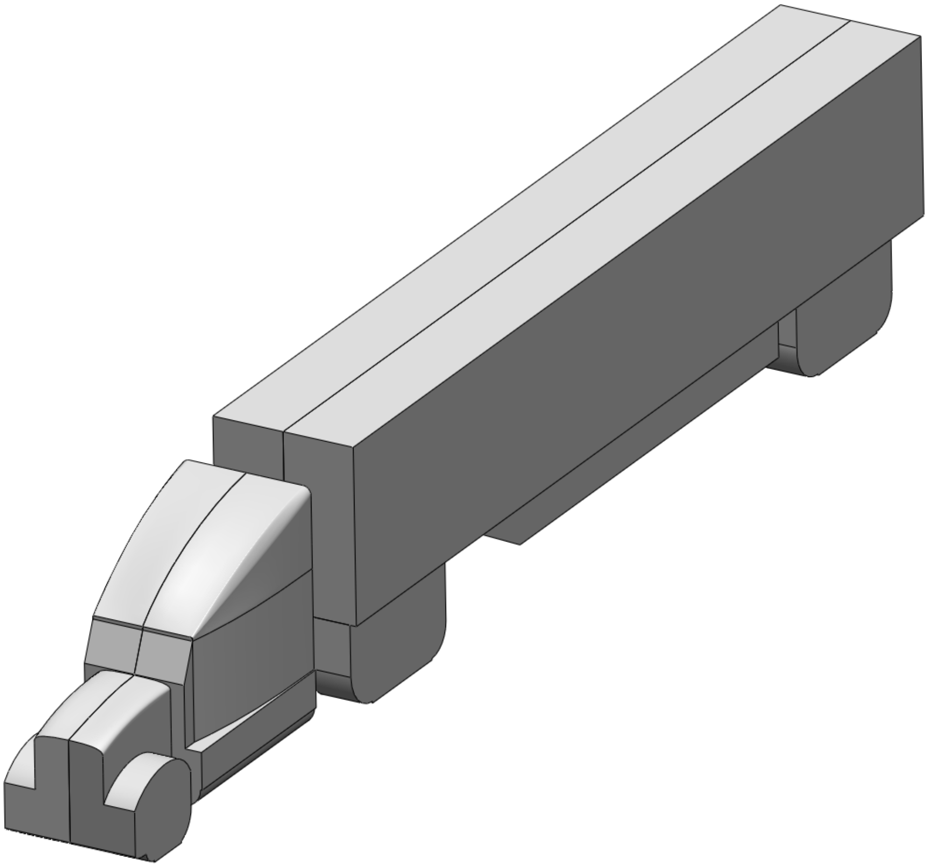

Figure 4.4: Peterbilt 579 Model

4.2 Meshing

The mesh development process was similar to that of the Ahmed body: global parameters were defined, refinement zones were identified, and inflation layers were added to solid surface. The only major difference in the meshing process came from the complexity of the tractor geometry, as discussed in Sec. 4.2.4.

4.2.1 Global Meshing Parameters

Many of the global parameters developed in Sec. 3.2 were independent of length scale and could be directly applied to the tractor-trailer model, for both the single and multi-vehicle simulations. The knowledge obtained from the meshing of the Ahmed body was used to determine the appropriate global settings, the most dominant of which are shown below in Table 4.1.

Table 4.1: Single tractor-trailer global mesh parameters

Parameter	**Value**
Advanced Sizing	Proximity and Curvature
Smoothing	High
Minimum Cell Size	1 in
Max Face Size	120 in
Max Size	120 in
Growth Rate	1.2

Parameters such as sizing method, smoothing, and growth rate were not changed from the Ahmed body simulation, while minimum and maximum cell sizing were scaled to the tractor-trailer. The minimum and maximum sizes of 1 in and 120 in respectively correspond to 0.11% and 14.29% of the reference scale length (70 ft), whereas the Ahmed body mesh minimum and maximum element sizes represented 1% and 25% of reference length (1 m). This is indicative of a finer overall tolerance, particularly in the free stream region.

4.2.2 Mesh Refinement

Five refinement zones were identified for the single truck geometry: exterior, tractor, trailer, under body, and wake regions. These volumes are respectively labeled Regions I-V and a side view is shown below in Fig. 4.5.

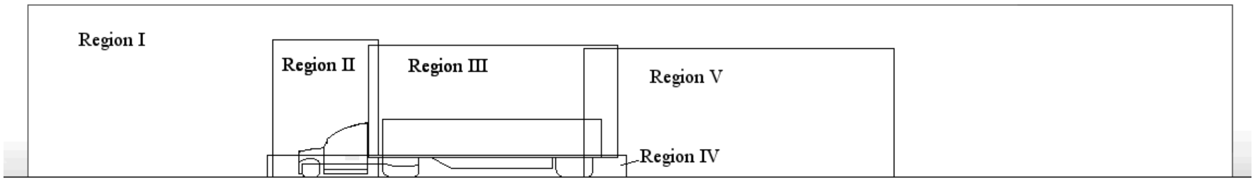

Figure 4.5: Single tractor-trailer model refinement regions

Region I, the exterior region, was defined for the same purpose as in the Ahmed body simulation, to provide a mesh transition region that is not as fine as the near body regions, but less coarse than the far field. This zone includes the entire geometric model and was proportionally defined to be much larger than its Ahmed body counterpart because the flow enveloping the tractor-trailer is much more complex and extends farther into the surrounding domain. The volume around the tractor was defined as Region II, and together with Region III, encompasses the entire upper vehicle. Region II and Region III were treated as separate refinement zones because the flow around the trailer is much less complex than the flow around the tractor, requiring less refinement. Flow over the trailer is comparable to that over a flat plate, while the tractor has contours and attributes that deflect the airflow and cause flow structures.

Region IV includes the remainder of the geometry: the under body. This region was specifically targeted because there are several geometric features and limited space between the road and other surfaces, similar to the Ahmed body. The final region, Region V, is the wake region. As with the simpler model, a refinement region was added in the vicinity of the wake to preserve variable quality and properly resolve wake features. As with the exterior region, the Region V zone of influence is increased when proportionally compared to the Ahmed body wake refinement.

In addition to volumetric refinements, surface refinements were defined to increase the mesh fineness on the body surface. All surfaces on the body were candidates for refinement, thus the entire body was selected and parsed into four categories: tractor, trailer, wheel, and lower wheel surfaces. Figure 4.6 explicitly shows the locations corresponding to each surface refinement, with Fig. 4.6b being a zoom view of the rear wheel.

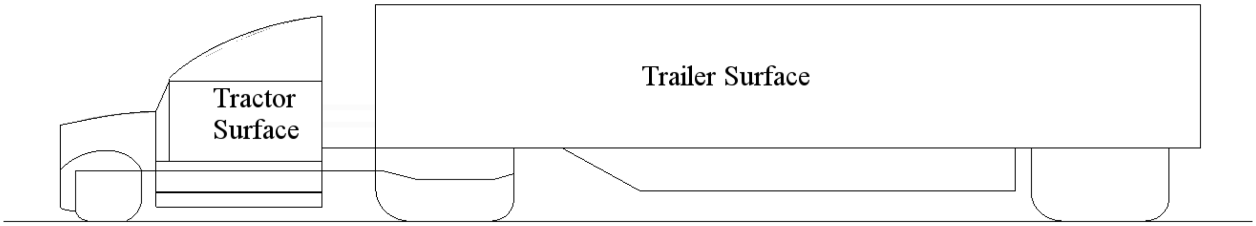

(a) Single tractor-trailer surface refinements

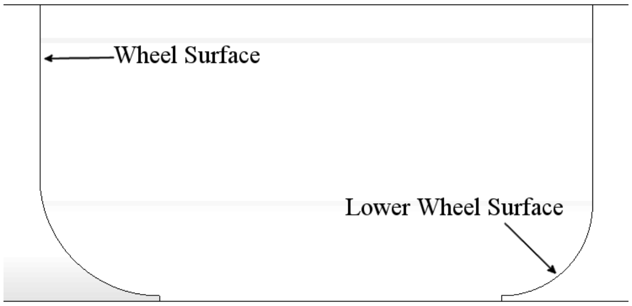

(b) Single tractor-trailer wheel surface refinements

Figure 4.6: Single tractor-trailer wheel surface refinements

It should be noted that although Fig. 4.6 only shows a rear wheel, this surface sizing included every vehicle wheel. The lower wheel surface refinement was separated from the general wheel refinement to allow a smaller minimum cell size on the surfaces of the wheels that were in close proximity to the road surface and had high surface curvatures. A minimum element size of 0.1 in was used instead of the default 1 in.

Table 4.2 below summarizes the refinement settings for both the volumetric and surface regions discussed above, along with the percent of scale length and the percent length for the Ahmed body equivalent refinement parameter.

Table 4.2: Single tractor-trailer mesh refinement parameters

Location	**Preferred Size (in)**	**% Body Length**	**Ahmed % Equivalent**
		Region Sizing	
Exterior	36	4.3%	3.0%
Tractor	12	1.4%	3.0%
Trailer	20	2.4%	3.0%
Under body	12	1.4%	1.5%
Wake	20	2.4%	2.0%
		Face Sizing	
Tractor	10	1.2%	1.0%
Trailer	15	1.8%	1.0%
Wheel	10	1.2%	0.2%
Lower Wheel*	10	1.2%	0.2%

* - Lower Wheel minimum size set to 0.1 in

It can be seen from Table 4.2 that most of the parameters closely match the related Ahmed value, the largest discrepancies being a 1% difference in relative wheel element sizing and a 1.3% difference in exterior volume sizing. The deviation in exterior element sizing affects the mesh quality trivially: the tractor-trailer exterior zone is much larger than the Ahmed exterior zone and the model includes further refinement zones that the Ahmed does not.

The 1% difference in wheel element sizing was considered acceptable for two reasons, foremost being scale of the wheel. The Ahmed body leg diameter is 3% of body length, whereas the trailer wheel length is approximately 12.6% of scale length. Because the wheel percent length is approximately four times larger on the tractor-trailer geometry than the Ahmed, a more coarse mesh is appropriate. The second reason is the overall mesh density was already much higher than that of the Ahmed body simulation, as discussed in the subsequent section, Sec. 4.2.5.

4.2.3 Inflation Layers

As described in Table 4.3, inflation layer parameters used for meshing the tractor-trailer vehicles were identical to those used to mesh the Ahmed body. Once again, these determined parameters were set using the methods described in the Best Practices guidelines for Automotive External Aerodynamics in FLUENT [35].

Table 4.3: Single vehicle inflation layer settings

Parameter	**Value**
First Aspect Ratio	5
Maximum Layers	5
Growth Rate	1.20

Figure 4.7 below illustrates the resulting mesh of the inflation parameters listed in Table 4.3 using a cross section of the mesh near the midpoint of the vehicle.

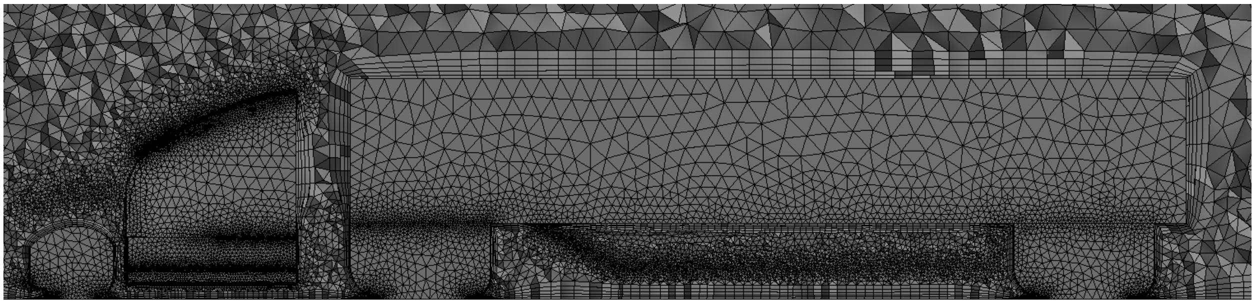

Figure 4.7: Single tractor-trailer inflation layers

4.2.4 Workaround Features

Though much of the meshing process was similar to meshing the Ahmed body, due to the complexity of the tractor-trailer geometry, additional steps had to be taken to ensure mesh quality.

Because a CAD model is only a representation and not a physical object, nonphysical regions can be created. The meshing algorithm will fail when attempting to discretize and mesh these regions. A prime example of this phenomenon is the intersection of a wheel with the ground surface, as shown in Fig. 4.8. This interface leads to the mesher attempting to create a volumetric mesh on a single 1D line, which results in an ill-posed or impossible-to-solve grid.

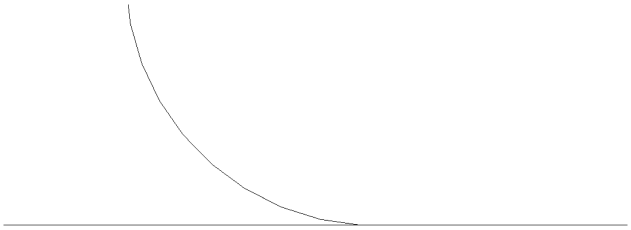

Figure 4.8: Wheel – road surface interface

When ANSYS Meshing attempts to create a volume mesh in this space it cannot because the elements must be a finite size, and to mesh this unphysical feature would require infinitely small elements. In essence, the meshing algorithm is attempting to create a mesh in an ever-shrinking volume that converges to a single line.

It is possible to create "pinches" in regions such as this that cut off the plane intersection locations, but they must be defined for every instance of non-physical geometry. It is often more accurate and more convenient to make model modifications to work around such limitations.

Thus workarounds were added or created from existing features to allow the geometry to be meshed. The workaround features added were always minimally invasive and were designed to affect the overall flow in a negligible way. For example, the solution to the problem presented by Fig. 4.8 is shown below in Fig. 4.9; a simple one inch stair step was added to create a finite region instead of a steep plane intersection.

Figure 4.9: Wheel – road modified surface interface

4.2.5 Baseline Meshes

After global and inflation layer parameters had been set, refinement zones specified, and work-around features implemented, the final meshes were generated for each geometry. Identical meshing parameters were used on each geometry, resulting in similar quality meshes.

An isometric view of the vehicle surface mesh for the Peterbilt 579 is shown below in Fig. 4.10. Note that the mesh becomes tighter in complex regions, such as around the curvature of the tractor or in the under body region, while becoming more coarse in regions requiring less refinement, for example the "flat-plate" style region on the trailer. This is a desired quality and results from the refinement volumes and surfaces specified and passed to the meshing algorithm.

Table 4.4 shows the final baseline mesh metrics for each geometry: number of elements, average skewness, and maximum skewness. Reiterating the discussion of Sec. 2.4, the desired average skewness is 0.25 and the maximum allowable single element skewness is 0.90.

Table 4.4: Single vehicle mesh results

Geometry	**Number of Elements**	**Average Skewness**	**Maximum Skewness**
Peterbilt 579	2.7M	0.2511	0.8877
Peterbilt 379	2.5M	0.2517	0.8991
Mercedes-Benz ACTROS	2.2M	0.2485	0.8966

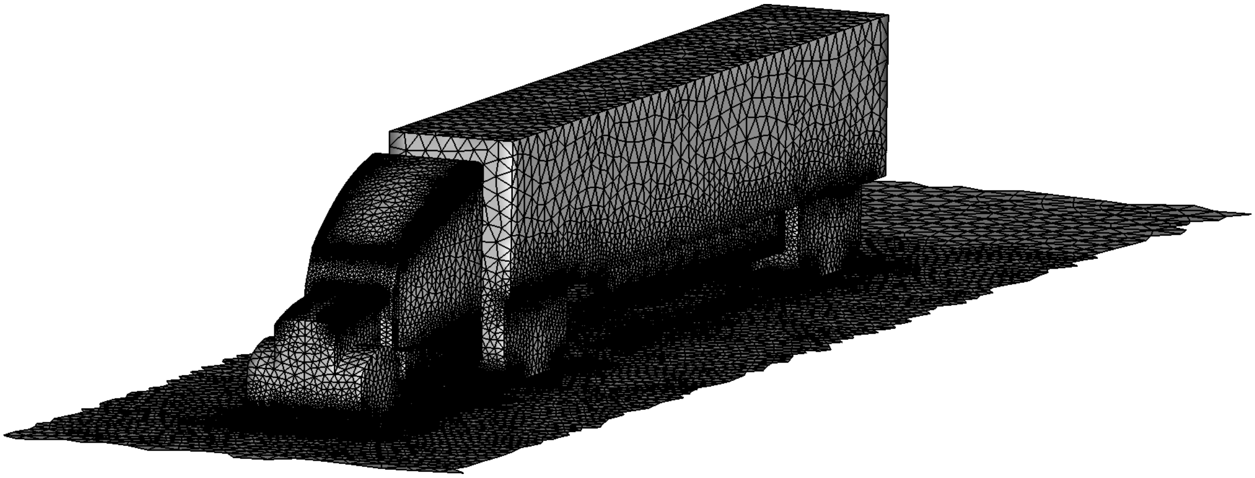

Figure 4.10: Single tractor-trailer final mesh

Table 4.4 shows that each mesh is over two million elements in size, with the primary Peterbilt 579 almost doubling the size of the Ahmed body baseline mesh. The large increase in number of elements for very similar meshing parameters is a testament to how much geometric complexity is added from using even the simplified models. Though element size reduction was considered, it was ultimately decided that the parameters above resulting in a satisfactory baseline because any mesh larger than 3M elements per vehicle would be unfeasible to run for multi-vehicle simulations due to hardware limitations.

A histogram of the largest skewness elements was also examined for each geometry. This was done to determine if there were a large number of low quality elements that would reduce solution accuracy or prevent convergence. Figure 4.11 shows the all elements with a skewness larger than 0.80 for the Peterbilt 579 model.

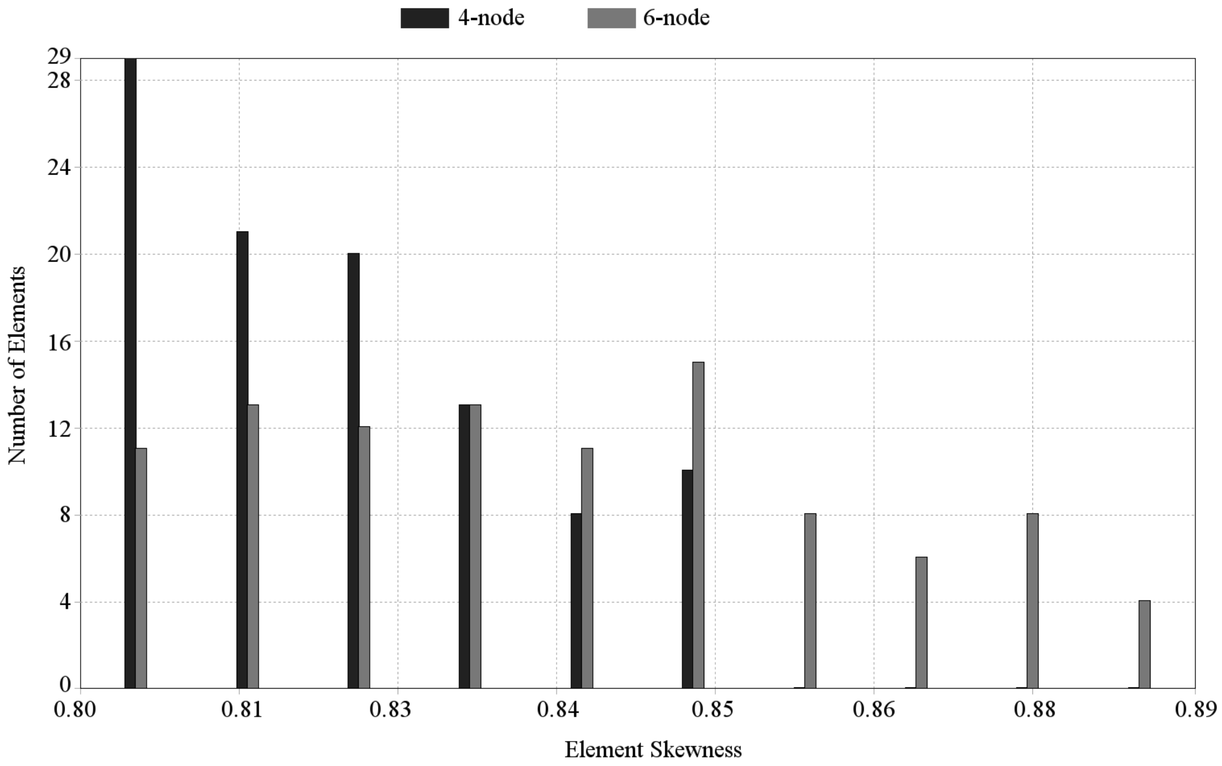

Figure 4.11: Single tractor-trailer maximum skewness histogram

All geometries had profiles similar to this, with a fairly large number of high skew elements in the low 0.80s and fewer closer to 0.90. There are more low quality elements than with the Ahmed body, which was expected, but the total set size is still less than one hundred elements out of more than two million in every case.

4.3 Simulation

Though there was some variance in the meshing procedure to accommodate the added complexity of the tractor-trailer geometry, the simulation methodology developed in Sec. 2.2 and discussed in Sec. 3.3 was modified as little as possible. This was because the techniques used in the Fluent simulation were verified for the Ahmed body against wind tunnel data [13] and therefore known to produce an accurate solution.

The only variance from the already determined methodology was relaxation factors to assist in solution convergence. The Courant number was lowered from 50 to 20 to prevent divergence in the multi-vehicle cases and thus was also lowered to 20 in the single body simulations to maintain congruency.

The reference conditions used to nondimensionalize the drag force are listed below in Eq. (4.1). The velocity and density are nominal values and the reference area was calculated used Fluent's "Projected Area" capability with a tolerance of 0.001 m for each model.

$$\begin{aligned}
&v = 30\,\mathrm{m/s} \\
&\rho = 1.225\,\mathrm{kg/m^3} \\
&A = 9.487\,\mathrm{m^2} \quad \text{(Peterbilt 579)} \\
&A = 9.694\,\mathrm{m^2} \quad \text{(Peterbilt 379)} \\
&A = 9.621\,\mathrm{m^2} \quad \text{(Mercedes-Benz ACTROS)}
\end{aligned} \tag{4.1}$$

4.4 Results

Once all geometries had been properly meshed and simulation parameters defined, single vehicle flow solutions were generated. Figure 4.12 shows the pressure distribution and velocity magnitude profiles for each geometry, while Table 4.5 lists the predicted drag coefficient for each vehicle. The first geometry shown is the primary model, the Peterbilt 579, or P579. The second model shown in both Fig. 4.12 and Table 4.5 is the Peterbilt 379 (P379). The final profile and drag discussed is the Mercedes-Benz ACTROS (MBA).

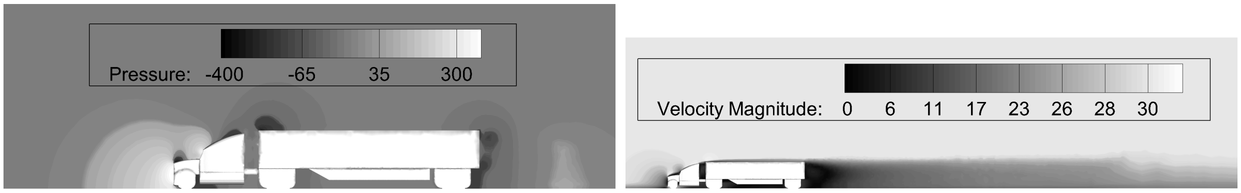

(a) P579 pressure (b) P579 velocity

(c) P379 pressure (d) P379 velocity

(e) MBA pressure (f) MBA velocity

Figure 4.12: Single tractor-trailer pressure distribution and velocity profile

Table 4.5: Single vehicle drag coefficients

Geometry	**Pressure**	**Viscous**	**Overall Drag**
P579	0.4949	0.0322	0.5271
P379	0.8513	0.0252	0.8766
MBA	0.4734	0.0344	0.5078

Comparing the pressure and viscous drag presented in Table 4.5 confirms the expected: viscous forces account for a small amount of total drag (small but not negligible), whereas pressure force produces the majority of drag, being approximately 95% of overall drag is each case. The drag coefficient for the Peterbilt 379 is much higher than that of the P579 or the MBA, this is also an anticipated result as the P379 does not have an over-cab fairing to slowly displace the flow, thus the highly directed airflow over the tractor encounters a second flat orthogonal surface, producing an extraordinary amount of additional drag. This is discussed in Sec. 4.4.1, where an analysis of the pressure drag per surface for the P379 model is presented.

An unpredicted result that is apparent from Table 4.5 is that the drag of the ACTROS tractor is comparable to that of the Peterbilt 579. The MBA vehicle is extremely blunt, whereas the P579 is designed to be more aerodynamic. When examining Fig. 4.12c, this highlights the impact of the upper fairing on the tractor; having a high speed flow impacting the front surface of the trailer is extremely detrimental from a drag perspective.

The most immediately noticeable feature of Fig. 4.12 is the similarity between all the profiles: each has a region of high pressure / low velocity at the nose, where the stagnation point is located, followed by a sharp acceleration over the cabin. The flow then continues along the trailer, which acts effectively as a flat plate, until it reaches the abrupt end. The immediate ending of the trailer causes the flow to recirculate backwards and form two vortices: an upper and a lower. The wake of each vehicle is remarkably similar, this emphasizes the region of influence concept discussed earlier: the tractor of each vehicle has little effect on the wake flow. A closer view of the P579 wake is shown in Fig. 4.13.

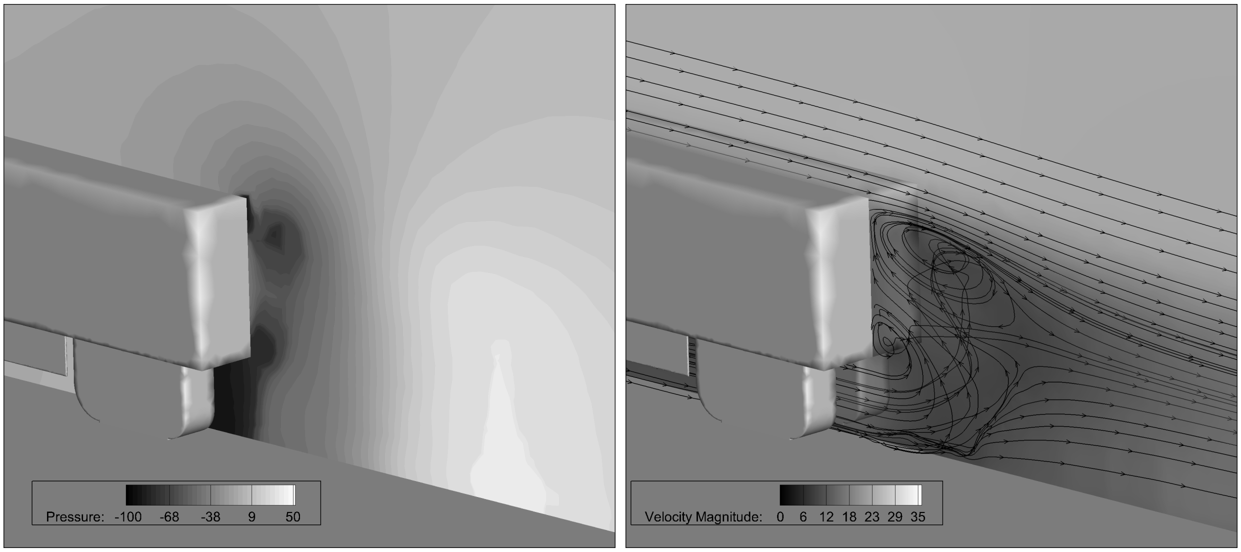

(a) Pressure

(b) Velocity & streamlines

Figure 4.13: P579 wake pressure distribution and velocity profile

From the streamlines shown in Fig. 4.13b it is clear that the flow from under the vehicle accelerates upward and spirals towards the rear face. After encountering the rear surface, a portion of the flow is channeled into the tighter, smaller lower vortex but the majority of the flow moves upward where it encounters the air from above the vehicle, this causes the flow to spin into the larger upper vortex. The trapped air from each vortex is then laterally funneled outward where it rejoins the remainder of the flow in the longitudinal direction.

To give insight into the strength of each vortex, Fig. 4.14 below illustrates the vorticity magnitude profile of the P579 wake. It shows that not only is the upper vortex larger, it also has a significantly higher rotational energy than the lower vortex, indicating that the upper vortex is the dominant of the two.

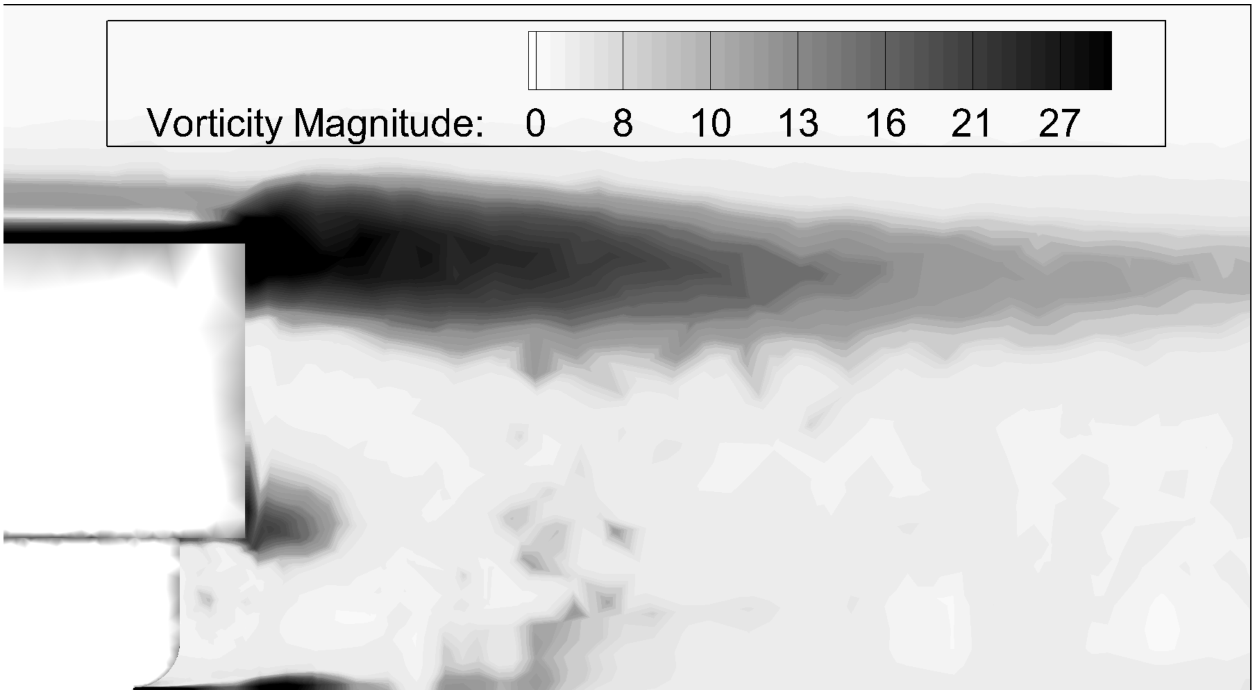

Figure 4.14: Peterbilt 579 wake vorticity magnitude

Another important conclusion that can be drawn from the velocity profiles shown in Fig. 4.12 is the wake length. The slipstream from each vehicle extends approximately 2-3 vehicle lengths backwards in the domain before experiencing significant degradation. This distance is considerably longer than the Ahmed body wake region, which, using a generous estimate, extended to two body lengths at most. The slipstream disturbance length is noteworthy because that is region where the most drag reduction is expected to occur. Vehicles inside this region are predicted to experience increased benefit due to the lower overall flow velocity.

4.4.1 Surface Drag

In an effort to better comprehend which faces cause the most drag on each vehicle, each vehicle was separated into five surface zones and the contribution from each zone was examined. The five zones analyzed were: tractor surfaces, the trailer front surface, the trailer rear surface, front trailer wheel surfaces, and rear trailer wheel surfaces.

Surface zones where used instead of individual surfaces because of the geometric complexity of the tractor-tailer models. Whereas in the Ahmed body simulations there were minimal body faces and analysis on each surface could be easily performed, the tractor-trailer models each contain many surfaces and it is highly impractical to study individual surfaces. Additionally, a surface-by-surface investigation is unnecessary since the areas highlighted by each zone are of interest because of the sum total effect they have on the flow.

The results of the surface drag analysis are shown below in Table 4.6. The pressure drag in each zone is shown as percentage of the total pressure drag. Though these surfaces are not inclusive of the entire body, they account for over 98% of the pressure drag in each model. The main reason for this is because most surfaces that were not analyzed were parallel to the flow direction and thus caused only skin friction (viscous drag). The data presented in Table 4.6 is also graphically displayed by Fig. 4.15 to provide a visual representation of the surface drag composition.

Table 4.6: Single vehicle surface pressure drag as a percent of total

Geometry	**Tractor**	**Trailer Front**		**Trailer Rear**	
		Surface	**Wheels**	**Surface**	**Wheels**
P579	53.7%	10.4%	3.7%	22.7%	9.5%
P379	33.5%	45.8%	3.2%	12.0%	5.5%
MBA	46.7%	8.7%	7.7%	24.3%	12.6%

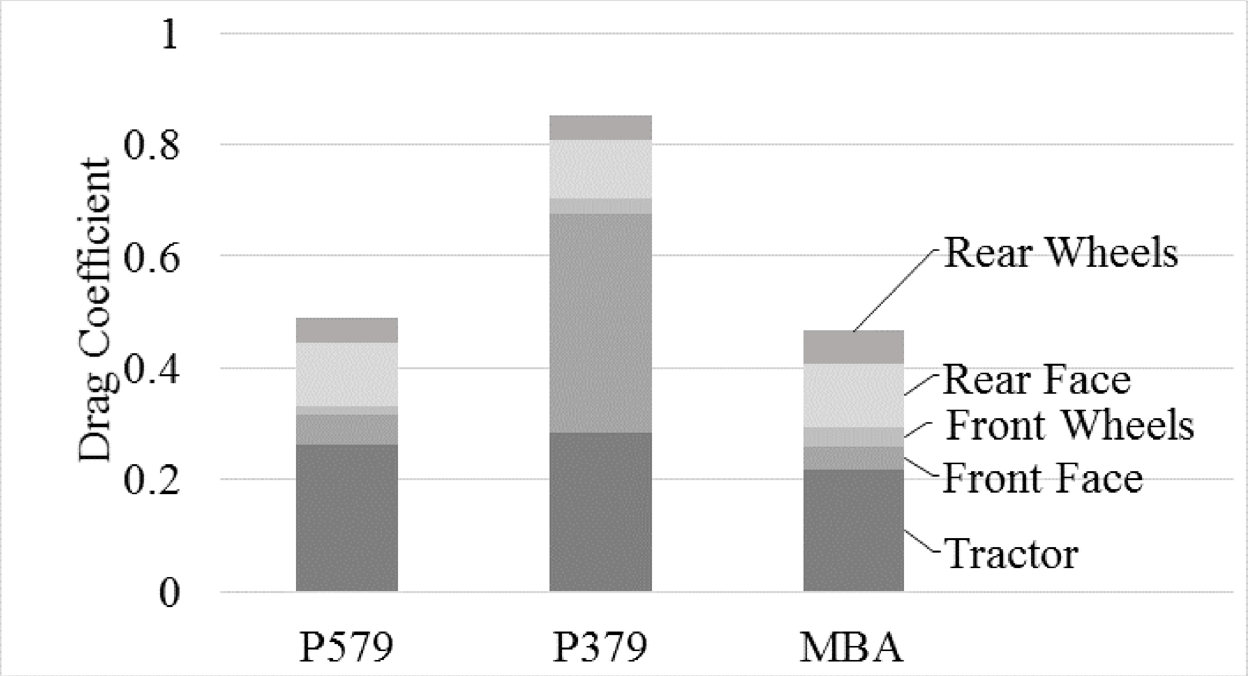

Figure 4.15: Single vehicle surface pressure distribution

For the P579 and MBA models there were two main contributors to drag: the tractor and the rear surfaces. The P379 had an additional major factor in the frontal trailer surface, which was due to the fact that there is no fairing over the P379 tractor. From a non-relative perspective this extra force is the main reason the drag coefficient on the P379 model is so large: the tractor drag magnitudes were similar while the frontal trailer drag was increased by a factor of 10 on the Peterbilt 379 when compared to the other models.

The pressure drag on the wheels is also noteworthy. Combined it accounts for 15-20% in the P579 and MBA cases: a significant contribution that likely cannot be negated via the platooning methods investigated in this study.

Using the conclusions drawn in Sec. 3.5.2, much can be gleaned from the drag composition profile presented by Table 4.6. It was discovered that the rear vehicle only influenced the rear surface of the lead vehicle and vice versa. Because the table above shows an uneven distribution between frontal and rear surfaces, it can be reasonably proposed that the rear vehicle will always see significant benefit over the lead vehicle. Using the Peterbilt 579 case as an example, the drag reduction the lead vehicle in the platoon experiences will be only on the rear surface, which accounts for only 22.7% of total drag, whereas the follow vehicle will experience a reduction on the drag experienced by the tractor, which composes 53.7% of the total.

A fact that is not apparent from Table 4.6 but was expected from the qualitative analysis of the flow profiles is the magnitude of drag on the trailer surfaces. With the exception of the frontal trailer surface on the P379 model, the trailer surfaces had comparable drag force in every model. This further reinforces the conclusion that tractor geometry has little effect on vehicle wake or wake drag.

Chapter 5

Multiple Tractor-Trailer

This chapter presents main conclusions of this study: the results for multiple tractor-trailer simulations. The subjects covered at length include: two vehicle platoons, three vehicle platoons, and two vehicle platoons with incongruous tractor geometry.

The first results discussed are the two vehicle platoons, which were the primary focus of this research. The scope of the study was then extended to include platoons larger than two vehicles and multiple geometry simulations. These two topics were simulated and analyzed because they have direct applications to the CACC system discussed in Sec. 1.2.

Three tractor-trailer groups were examined to determine the added benefit of adding a third heavy vehicle to the platoon. While the CACC system can support additional vehicles, the logistical cost increases with every vehicle. The primary inquiry then becomes whether the third vehicle sees the same level of benefit as the second vehicle and if the fuel savings outweighs the additional complexity of a three vehicle platoon.

Multiple tractor geometry platoons were investigated to ascertain the effect of tractor geometry on drag reduction. As discussed in Sec. 4.1, three geometries were examined: the primary Peterbilt 579, the older Peterbilt 379, and the flat-nosed Mercedes-Benz ACTROS. There is a stark difference in the geometry of each these tractors, as would be seen in a real world highway situation. A platoon of uniform vehicles would be unlikely to form unless specifically designated, as there are many models of transportation vehicles on the highway at any given time.

When this is considered, vehicle order within the platoon becomes a significant issue. For example: if the Peterbilt 379, which has considerably more drag than the Peterbilt 579, experiences greater drag reduction as a follow vehicle than the P579, then a P579-P379 configuration platoon would result in the best overall drag reduction.

The same is true of the Mercedes-Benz ACTROS, though it sees roughly the same drag as the P579, it may provide less wake interference due to less-intrusive flat-nose profile. This would result in higher drag on the rear surface of the lead and would make it more beneficial overall for the MBA to be the lead vehicle in a platoon.

5.1 Meshing & Simulation

The meshing and simulation of the multiple tractor-trailer model was accomplished using the parameters developed in Chapter 4 and the meshing principles discussed in Sec. 3.2. As with the transition from single to multiple Ahmed bodies, parameters were kept as close as possible to maintain the same level of solution accuracy for comparison to the baseline single vehicle results.

The only major difference between the meshing and simulation of the single vehicle and multi vehicle models is the modification of the intermediate vehicle wake region to be an interior refinement region. For all simulations, this was a region that had identical meshing parameters to the wake box but instead of including only volume in the immediate vicinity of the vehicle, it encompassed the entirety of the spacing between vehicles. The extension of the wake region increased the number of elements in the mesh but was deemed necessary to maintain the flow fidelity between vehicles.

5.2 Two Vehicle Platoons

To begin multiple vehicle simulations, a second, identical body was added to the existing model and then simulated via the Fluent parallelized solver. An isometric view of the CAD model is shown below in Fig. 5.1 at a separation distance of 20 ft.

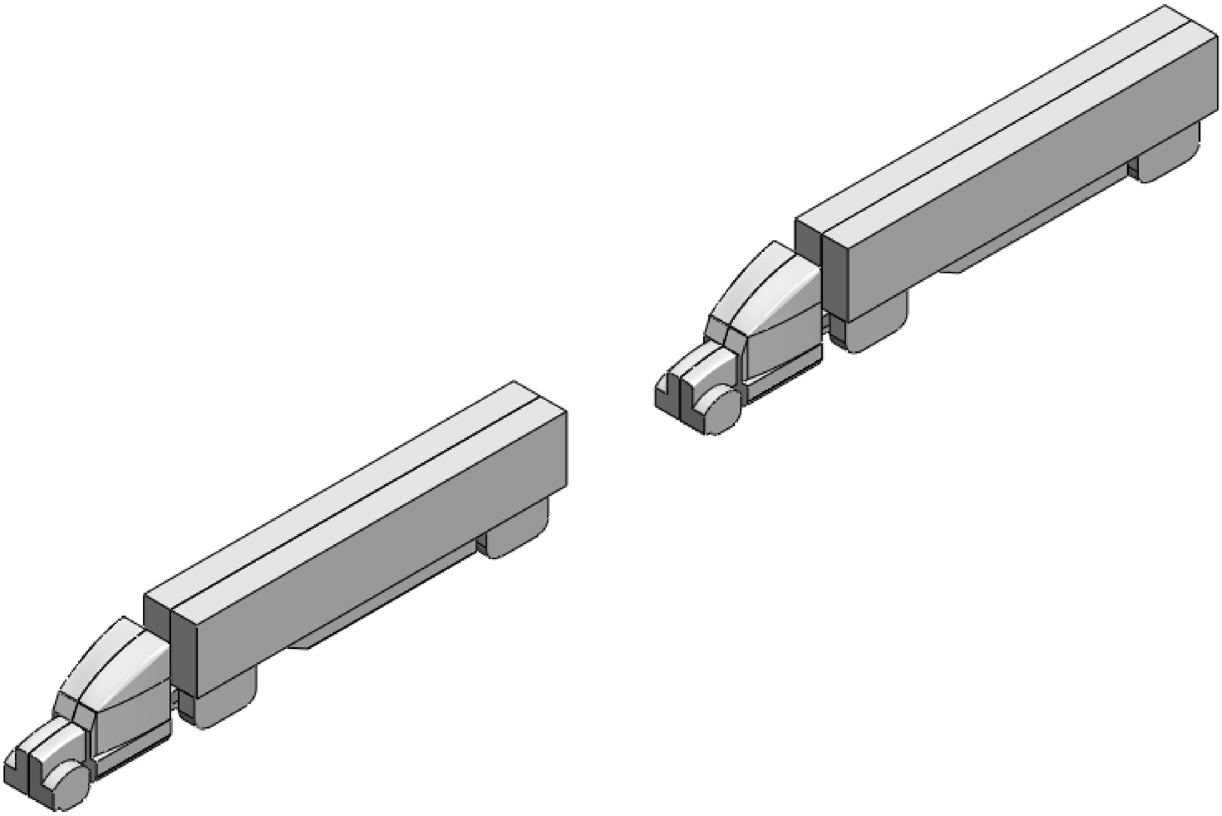

Figure 5.1: Two vehicle CAD model – 20 ft separation

Several separation distances were simulated in order to accurately portray the drag reduction trends that occur when a heavy vehicle is closely following a leader vehicle. The full suite of test cases is listed below in Table 5.1 along with percentage of body length (73 ft). Some distances were tested twice: once with the RKE turbulence model and once with DES. The reason for using both the DES and RKE models on particular distances is discussed Sec. 5.2.1.

Table 5.1: Two vehicle simulations matrix

Separation Distance	**Percent Body Length**	**Turbulence Model**
5	6.8%	RKE
10	13.6%	RKE
20	27.3%	RKE
30	40.9%	RKE
36	49.1%	RKE
40	54.6%	RKE
50	68.2%	RKE
60	81.9%	RKE
70	95.5%	RKE
80	109.1%	RKE, DES
90	122.8%	RKE
100	136.4%	RKE
200	272.9%	RKE, DES
300	409.3%	RKE
350	477.5%	RKE, DES
400	545.7%	RKE, DES
1000	1364.3%	RKE, DES

5.2.1 Results

To begin the analysis of the Fluent results, the velocity magnitude and pressure distributions were examined in the regions near the vehicles. This was done primarily to gain a qualitative understanding of the flow surrounding the two bodies. The velocity profiles and pressure distributions for the 10 ft, 36 ft, and 90 ft separation cases are presented below in Figs. 5.2–5.3.

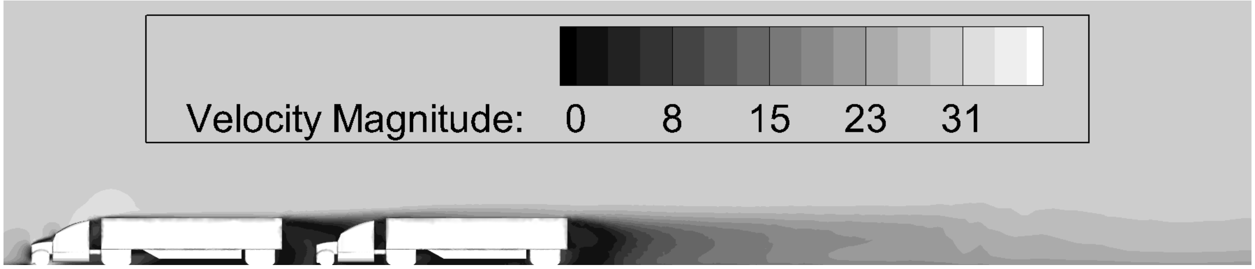

(a) 10 ft

(b) 36 ft

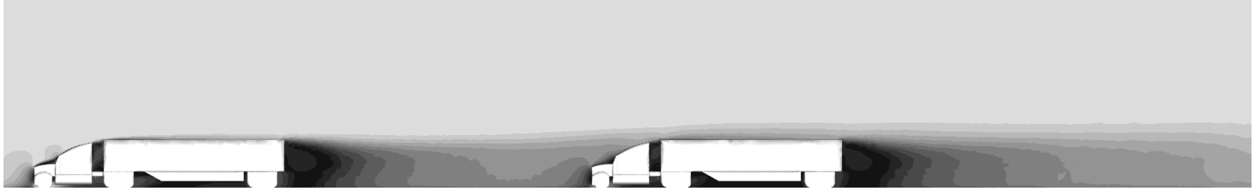

(c) 90 ft

Figure 5.2: Two vehicle velocity magnitude profile

The velocity profiles display what one would expect: when the follow vehicle is close (10 ft), there is a significant amount of wake interference, which is beneficial for both vehicles. As the separation distance increases, the wake interference decreases until there is virtually none at 70 ft, as evidenced by the drag coefficient discussed below in Fig. 5.4.

Even though the lead vehicle experiences no drag benefit at distances larger than a vehicle length, the follow vehicle still sees significant pressure force reduction. This is because the slipstream created by the front vehicle extends far beyond the wake and is considerably lower than the freestream velocity. Because force scales with velocity squared, the diminutive mean velocity results in a much lower force. The fact that the second vehicle is well within the slipstream of the first is easily seen in Fig. 5.2c.

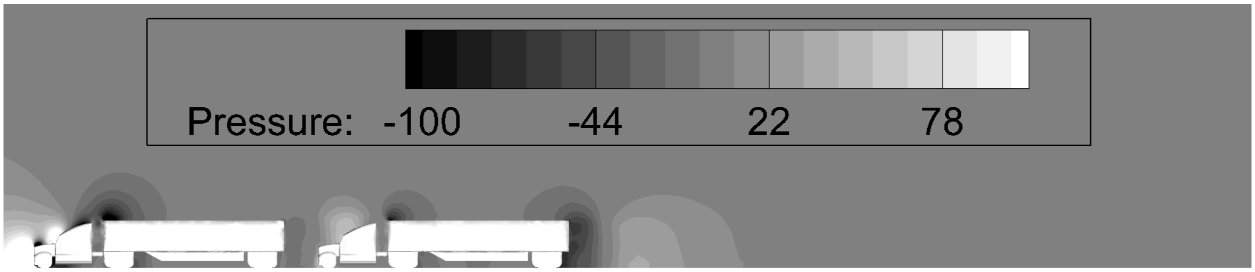

(a) 10 ft

(b) 36 ft

(c) 90 ft

Figure 5.3: Two vehicle pressure distribution

Examining the distributions presented in Fig. 5.3 confirms much of the speculation from examining the velocity magnitudes: at close distances the negative and positive pressure pockets that form at the rear of the lead and front of the follow vehicles are much smaller and lower in magnitude than at larger distances. This shows in Fig. 5.3a that the supposition that the lead trailer experiences less rear pressure drag because the wake is unable to fully form and the following tractor less frontal drag because of a lower mean velocity flow is in fact correct.

Each pressure profile also shows a trend from the Ahmed body simulations: the front of the lead body and the rear of the follow body are essentially unaffected as vehicle spacing changes. This was also expected and is an extension of the “limited region of influence” concept discussed in Sec. 3.5.

Once qualitative features of the flow were analyzed, the total drag force on each body was determined as a function of separation distance. The results are presented as a percentage of single body drag below in Fig. 5.4 for the test cases bewteen 0 and 100 ft separation. The single body drag coefficient for the Peterbilt 579 was $C_{D,single} = 0.5271$, as shown in Table 4.5 of Sec. 4.4.

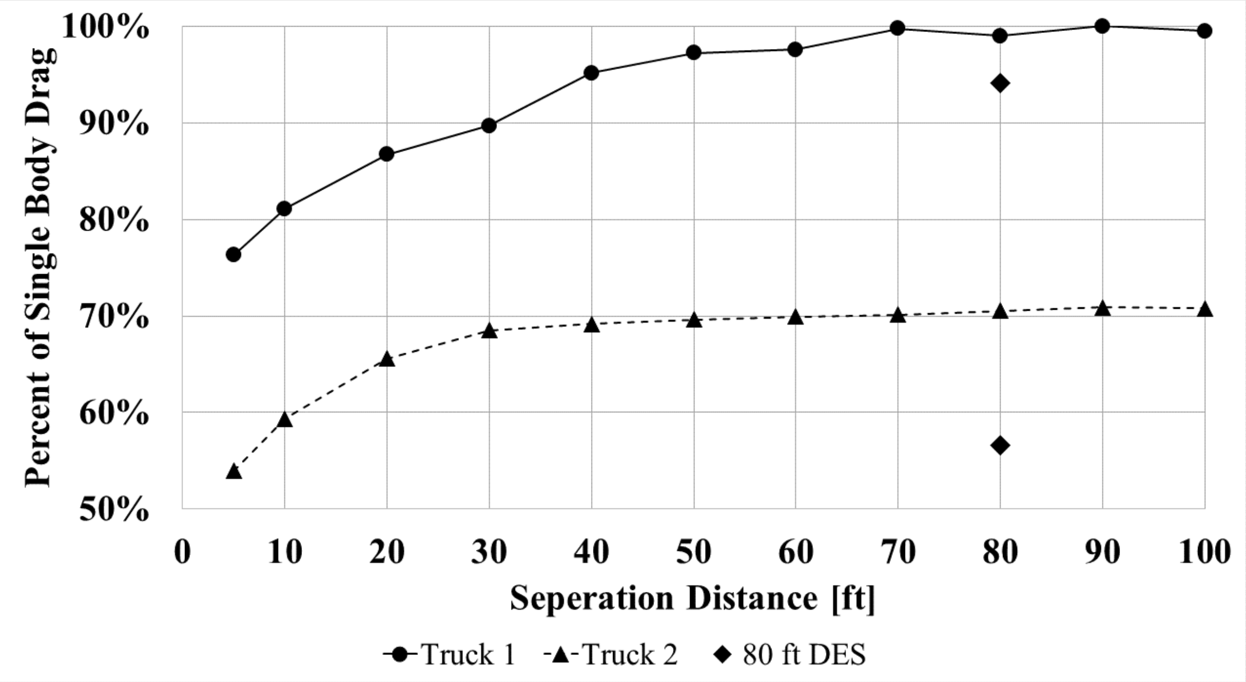

Figure 5.4: Two vehicle percent drag as a function of separation distance

It is apparent from Fig. 5.4 that the trend for the full tractor-trailer geometry is starkly different from that of the Ahmed body. Whereas the rear Ahmed body saw an increase (followed by a decrease at very close distances) in drag as distance between bodies decreased, the rear tractor-trailer sees a very large drag decrease at every distance, almost 50% at 5 ft. Secondly, at 1.5 body lengths both Ahmed bodies were within 10% of the nominal single body drag. While this is true for the front vehicle at 1.4 body lengths (100 ft), the rear vehicle is still only 70% of the single tractor-trailer drag and appears to be exhibiting asymptotic behavior. This phenomenon is what prompted the simulation at further distances.

5.2.2 Large Distance Simulation

A key point of investigation was determining the separation distance at which the follower vehicle no longer receives a noticeable benefit from platooning. It was clear at 100 ft, nearly 150% truck length, large benefits were still being experienced. Thus greater distances were simulated to find this cutoff distance.

Upon simulation of these distances, however, it was discovered that the solution generated by Fluent was incorrect at extremely large separations. To expose this flaw and why it occurs, it is helpful to begin by examining two cases at a spacing that can be considered effectively infinite, 1000 ft. These simulations were identical except for the turbulence model: the first used RKE while the second used DES. The velocity magnitude for each of these simulations is shown below in Fig. 5.5.

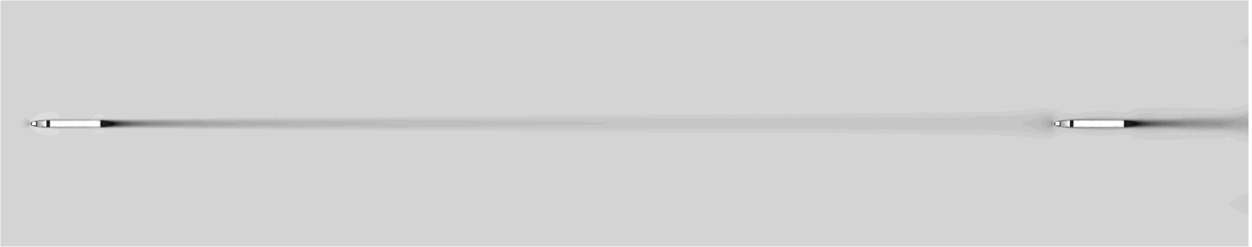

(a) RKE

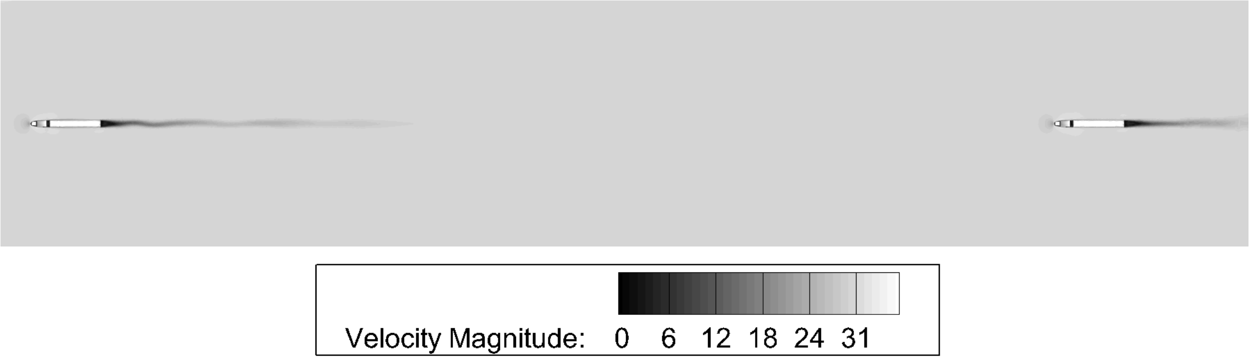

(b) DES

Figure 5.5: Two vehicle velocity magnitude – 1000 ft

It is immediately obvious that the RKE model is incorrect: the slipstream from the front vehicle propagates downstream infinitely; the wake is never terminated. The DES model, on the other hand, does accurately dissipate the disturbance caused by the lead. This leads to a marked difference in prediction of surface drag for the second vehicle in each case. The DES model correctly suggests that there is no drag reduction on the second body while the RKE model predicts a drag force that is still 75% of the single body drag.

The reason this occurs is the RKE turbulence model cannot capture the process of a turbulent flow returning to a laminar state, known as relaminarization [43]. If a flow cannot be relaminarized, the turbulence within the flow will self-perpetuate, a non-physical process that, in this case, extends the wake infinitely. The LES model upon which DES relies in the far field does have the capability to laminarize a turblulent flow [44] by virtue of the derivation approach, discussed in Sec. 2.3, and is thus much more appropriate for capturing this phenomenon.

The turbulent kinetic energy (TKE) of the flow is a good measure of the existing turbulence within a flow because it measures the total magnitude of the velocity fluctuations present, which is in essence the amount of turbulent energy that exists in that flow. For example, a completely laminar flow would have no TKE. Thus to examine the turbulence that exists in the wake of the lead vehicle, the TKE of both the RKE and DES 1000 ft simulations was graphed and is shown below in Fig. 5.6.

(a) RKE

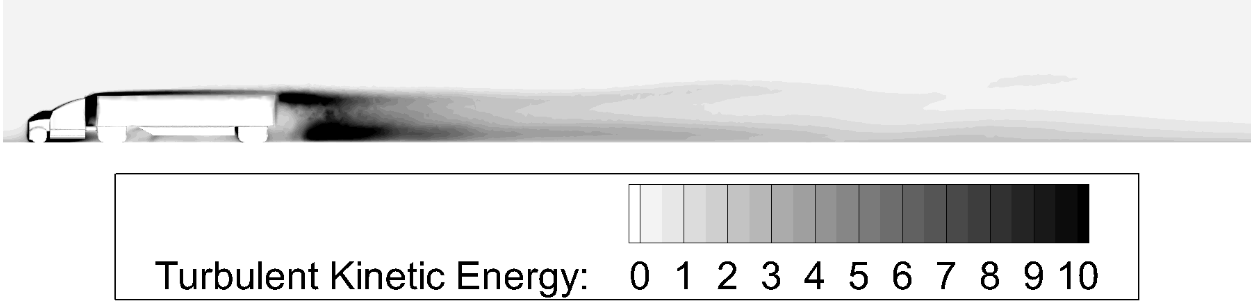

(b) DES

Figure 5.6: Two vehicle TKE – 1000 ft

As with all transient simulations, it is important to keep in mind that the DES profile of Fig. 5.6b is only a snapshot of a single time step.

It is clearly visible that the DES model properly dissipates the turbulent kinetic energy behind the vehicle whereas RKE retains a significant amount of TKE, never fully removing the turbulence from the flow. This shortcoming is the reason that the wake behind the RKE model is infinite: the flow can never transition back to a laminar state.

The inability to properly handle low TKE flows does not negate the usefulness of the RKE turbulence model or the results generated. This was seen in Sec. 3.4 and Sec. 3.5 where the single and multi Ahmed body simulations were validated with less than 5% error for the RKE turbulence model.

It does, however limit the regime of applicability for the RKE model. An RKE simulation cannot be reliability used at separation distances where the TKE has degraded significantly. Thus TKE was measured in the wake region of the 1000 ft DES model to determine the distance at which the TKE was 5% of the maximum in-wake value. This distance was found to be approximately 350 ft from the rear surface of the front vehicle. This location coincides very nearly with the end of the slipstream, which was calculated to be 307 ft from the rear surface using a velocity magnitude of 95% free stream value.

Knowing the approximate length of the turbulent wake region, large distances up to 500 ft were simulated to determine where the RKE model becomes inaccurate. Figure 5.7 shows the drag coefficients predicted by both the DES and RKE models.

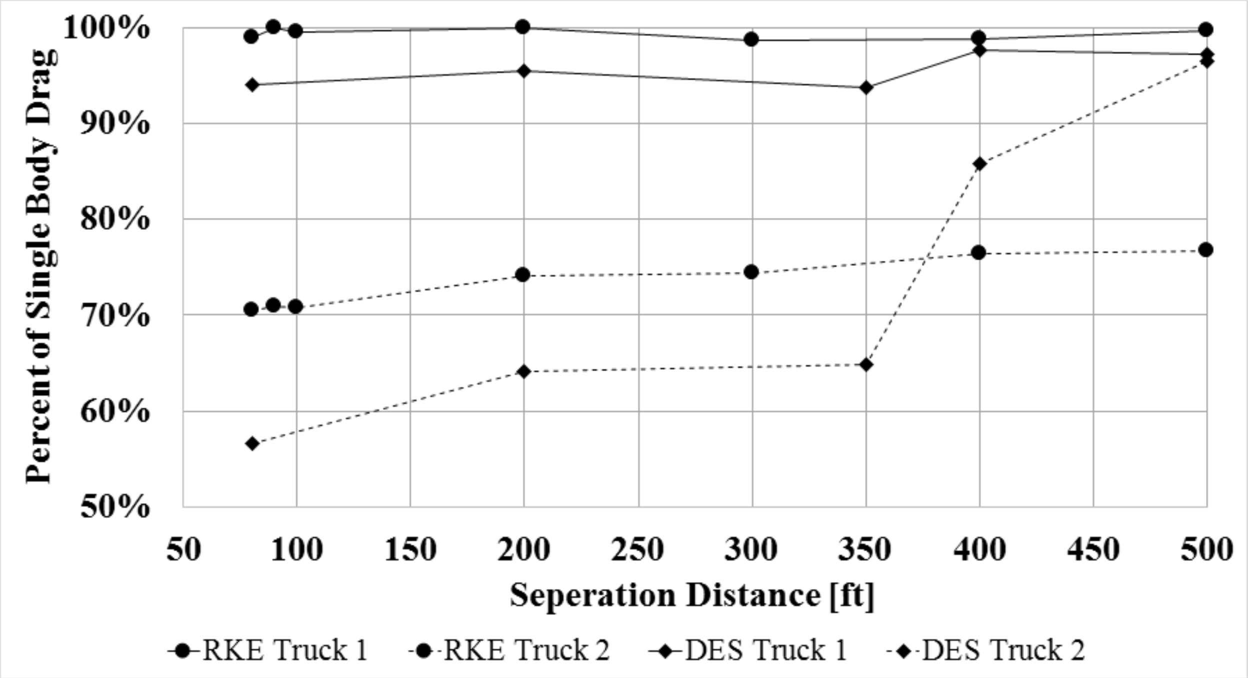

Figure 5.7: Two vehicle percent drag as a function of separation distance – large distance

Knowing that the DES model will always under-predict surface drag [36] is an important fact that can be used to determine the inaccuracy of the RKE model. When the follow vehicle drag coefficient produced by the DES model approaches that of the RKE model, it can be said that the RKE model is no longer accurately predicting the drag force experienced by the second vehicle.

Thus it can be seen from Fig. 5.7 that the RKE model becomes inaccurate between 350 and 400 ft. This suggests that the RKE model produces accurate results while the second vehicle is within the true wake created by the front vehicle; that is the inaccuracy of the RKE model compared to the vehicle separation distance is more correctly represented by a step function rather than a linear or polynomial function.

A periphery effect of this analysis answers the question initially posed: the distance at which the follower vehicle stops experiencing drag reduction. That distance occurs, as expected, shortly after the termination of the wake, which is approximately 450-500 ft.

When combining the knowledge of the small separation simulations presented by Fig. 5.4 and the large spacing tests presented in Fig. 5.7, three clear regions become apparent: wake, slipstream, and freestream. The wake region can be decomposed into two sub-regions: the inner wake and outer wake regions. In the inner wake region, any separation smaller than 40 ft, both vehicles see an extremely sharp decrease in drag as the distance between them decreases. In the outer wake, spacings between 40 and 70 ft, Vehicle 1 still experiences wake interference and has a reduced overall drag, but Vehicle 2 remains nearly constant at 70% of single vehicle drag.

The second region, the slipstream region, is defined as the region between 70 and 350 ft. In this region Vehicle 1 experiences no benefit, as Vehicle 2 is too far from the wake to have a significant effect on the lead body. The follow body experiences a near constant drag reduction between 65% and 75% of the single body value. This extremely slow increase suggests that while Vehicle 2 is in the slipstream created by Vehicle 1 the drag will be only weakly dependent on distance: a body following at 300 ft would see almost the same drag reduction as a body following at 100 ft.

The final region, termed the freestream, is any separation great than 450 ft. This region is marked by a sharp transition from the slipstream region to outside the Vehicle 1 disturbance. In the freestream region, neither vehicle sees any benefit from platooning.

5.2.3 Surface Drag Analysis

Having validated the RKE turbulence model and determined an appropriate cutoff distance, an in depth analysis of surface pressure drag was performed to determine the regions that receive drag reduction. As with the Ahmed surface analysis, viscous drag was not included because it comprises less than 10% of the total drag, is nearly non-existent on the transverse surfaces of interest, and is approximately constant.

While the single body drag was decomposed into five surface zones, it was more expedient to combine the frontal and rear surface and wheels into two zones because each of these zones is closely related to its counterpart. The three zones studied were then: tractor, trailer front, and trailer rear. Combined, these surfaces accounted for over 99% of the pressure drag in every case. The composition of the surface drag of the leader and follower vehicles is shown as a percentage of single truck drag below in Fig. 5.8.

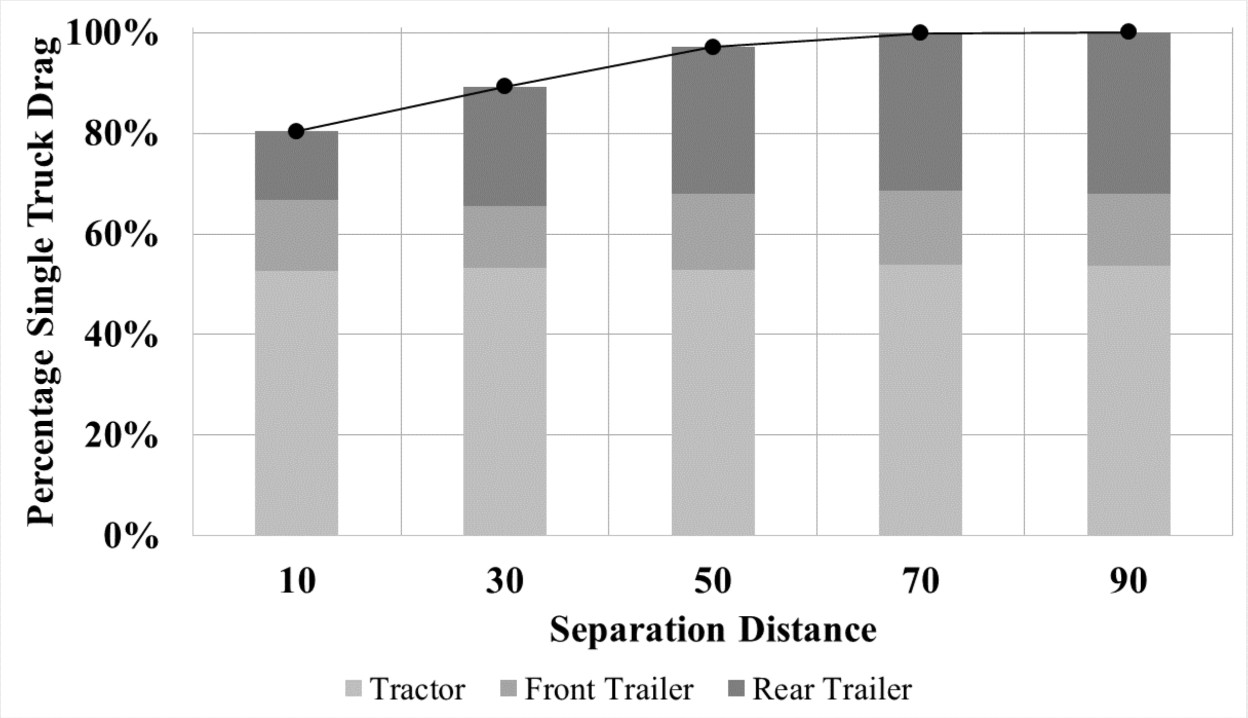

(a) Front Vehicle

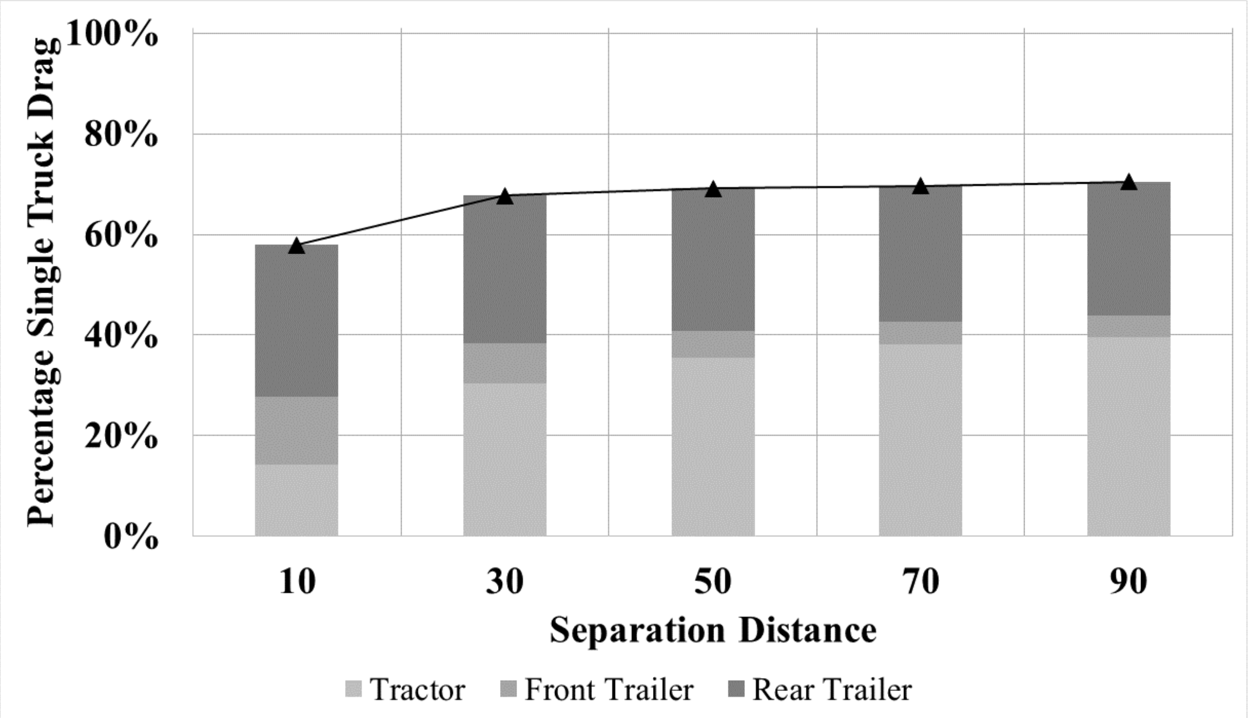

(b) Rear Vehicle

Figure 5.8: Two vehicle surface drag vs. separation distance

Examining Fig. 5.8a shows identical trends for the front vehicle as seen in the Ahmed body: frontal drag, namely tractor and front trailer drag, remains very nearly constant, indicating no effect on the front of the leader body. It is also shown that the increase in total drag with distance comes exclusively from the increase in rear drag, also as expected. Much the same is seen with the rear trailer and tractor drag in Fig. 5.8b: the rear drag is close to constant and the tractor drag increases with separation distance.

It is also worth noting that the surfaces that do see drag reduction, the rear of the lead and the front of the follow, experience roughly the same percentage change in drag force, 58% and 64% respectively. However, because the magnitude of the drag on the tractor is the largest contributor to pressure force, the close percentages translate to an overall larger reduction for the follow vehicle.

Trailer Front Surface Drag

An unexplained trend that appears, however, is a decrease in the front trailer pressure drag as distance between vehicles increases. This anomaly is explicitly shown by Fig. 5.9 where the trailer front drag is presented for each vehicle normalized by single body front trailer drag.

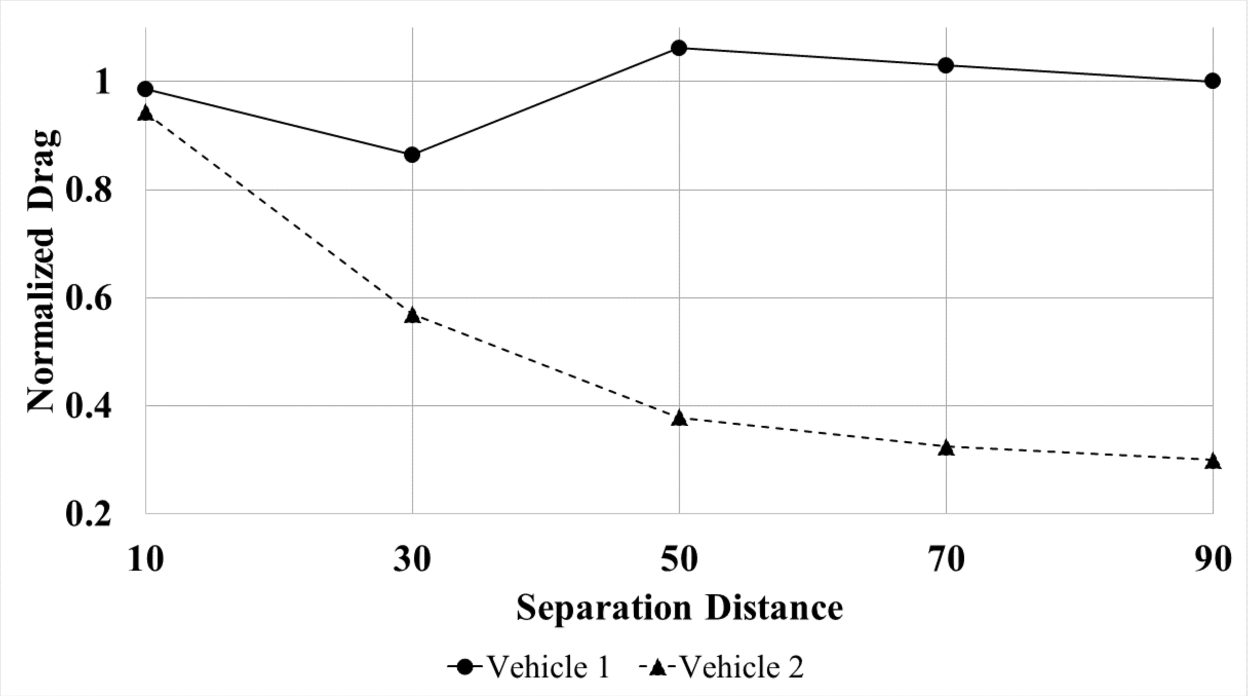

Figure 5.9: Two vehicle trailer front surface drag

As can be seen, the change is significant, reducing from over 90% at 10 ft to under 30% at 90 ft. To determine the origin of this stark decrease in force, pressure contours were graphed on the front trailer surface of the single vehicle and the two most different cases, 10 ft separation and 90 ft separation. The results are shown below in Fig. 5.10.

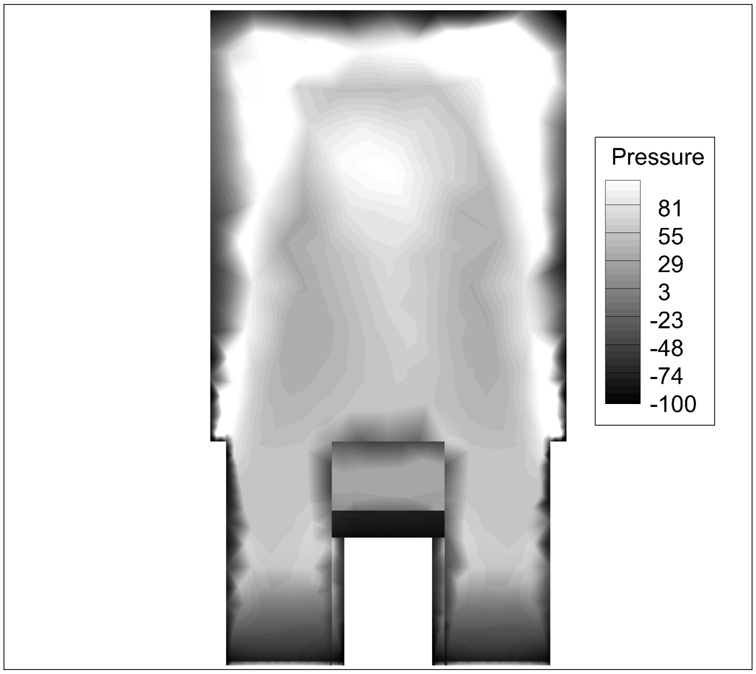

(a) Single Tractor-Trailer

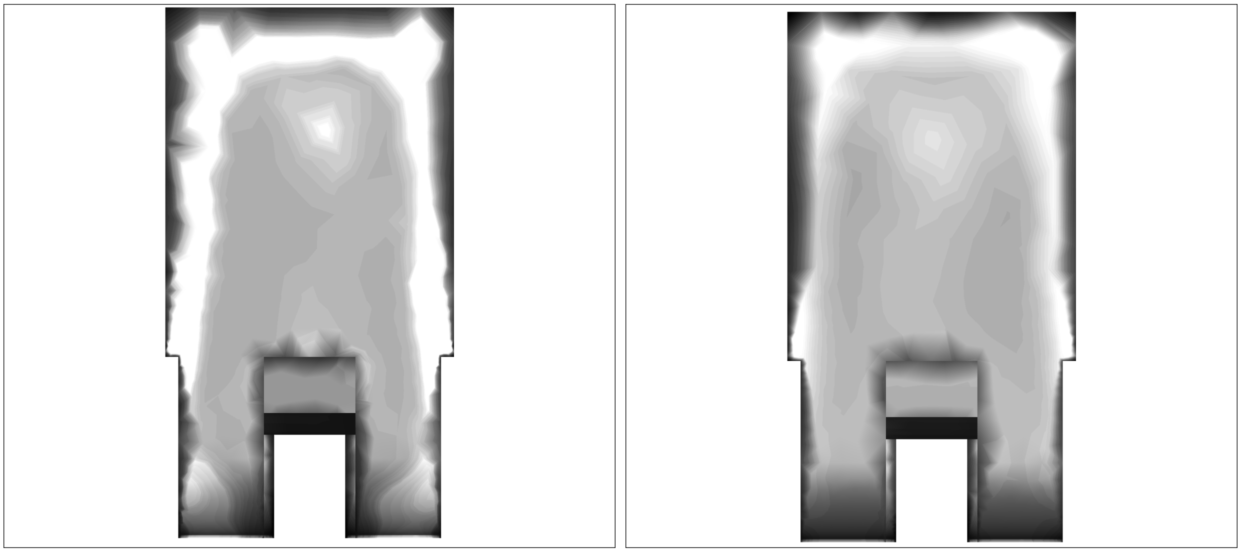

(b) Vehicle 2, 10 ft

(c) Vehicle 2, 90 ft

Figure 5.10: Two vehicle front trailer surface drag

The profiles are clear: though the force from Fig. 5.10a and Fig. 5.10b are nearly equivalent, the pressure distribution is not. In Fig. 5.10a, there are highly focused regions of large magnitude pressure causing the majority of the drag force whereas the pressure in Fig. 5.10b is less concentrated both in area and magnitude.

When considered with Fig. 5.10c, the contrasting pressure profiles and similar resulting forces indicate there is a separate drag-increasing phenomenon that arises in the tractor-trailer gap at close following distances but dissipates as the distance between the lead and follow vehicles increases.

To understand the pressure distribution, one must return to first principles. Typically, Bernoulli's equation can be used to relate pressure and velocity, however, in the region of interest there is a significant amount of vorticity and Bernoulli's equation is not sufficient as irrotational flow is one of the fundamental assumptions of the derivation. In cases such as this, Crocco's theorem [45] can be used to relate velocity and pressure via the inclusion of vorticity, denoted as ω.

Crocco's theorem, which uses the concept of stagnation pressure loss, states that:

$$\vec{v} \times \omega = \frac{1}{\rho} \nabla p_0 \tag{5.1}$$

Where vorticity is formally defined as the curl of velocity:

$$\omega = \nabla \times \vec{v} \tag{5.2}$$

The stagnation pressure p_0 is a measure of total flow energy and becomes a quantity that is no longer conserved with the introduction of vorticity, which is the primary reason that Bernoulli's equation cannot be applied. Stagnation pressure is represented using static pressure and velocity magnitude as follows:

$$p_0 = p + \frac{1}{2}\rho|\vec{v}|^2 \tag{5.3}$$

Substituting this into Eq. (5.1) and solving for static pressure p yields:

$$\nabla p = \rho(\vec{v} \times \vec{\omega}) - \nabla\left(\frac{|\vec{v}|^2}{2}\right) \tag{5.4}$$

This shows that the pressure distribution is a function of three variables: the velocity vector, the vorticity vector, and the velocity magnitude. Because velocity and vorticity are three dimensional vectors, the total number of properties of interest is seven. This adds a large amount of complexity to the Bernoulli equation, which depended only on the velocity magnitude to determine the pressure field.

To begin the analysis, the local velocity magnitude was examined. Figure 5.11 shows the rear vehicle for the 10 ft and 90 ft simulations side-by-side.

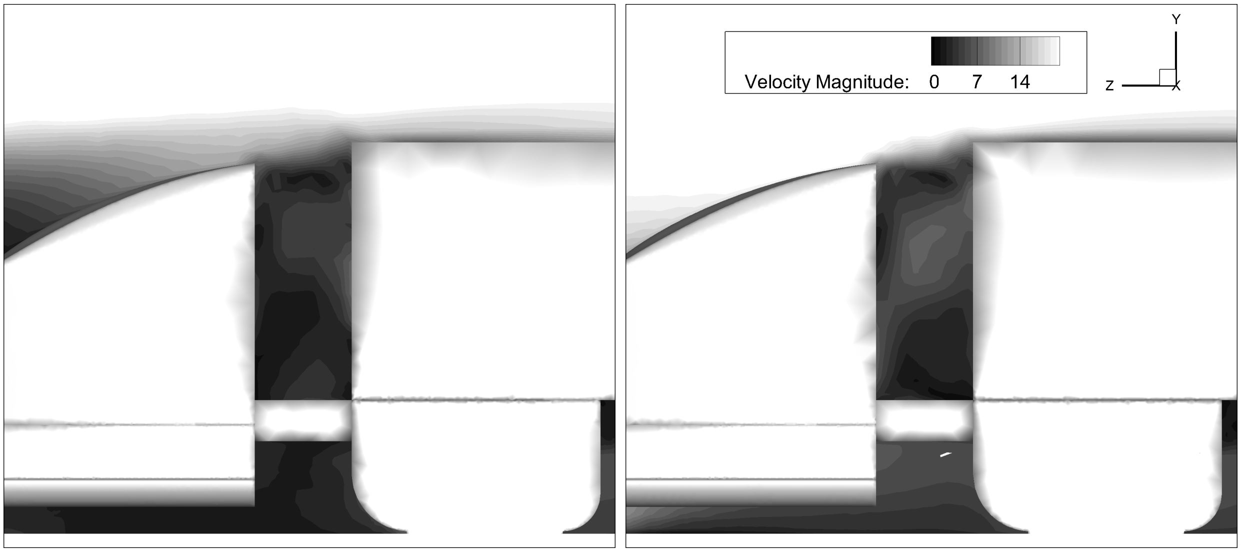

(a) Rear Vehicle – 10 ft

(b) Rear Vehicle – 90 ft

Figure 5.11: Two vehicle trailer front velocity magnitude

Though there are slight differences between Fig. 5.11a and Fig. 5.11b, the overall profile is very similar between the cases. The main difference is a slight increase in average magnitude moving from 10 ft to 90 ft, though this is not significant enough to account for a 300% pressure decrease.

At this point, it was clear that a Bernoulli approach was not adequate to capture the physics that exist in the local region and therefore the individual velocity components were plotted as shown in Figs. 5.12–5.14.

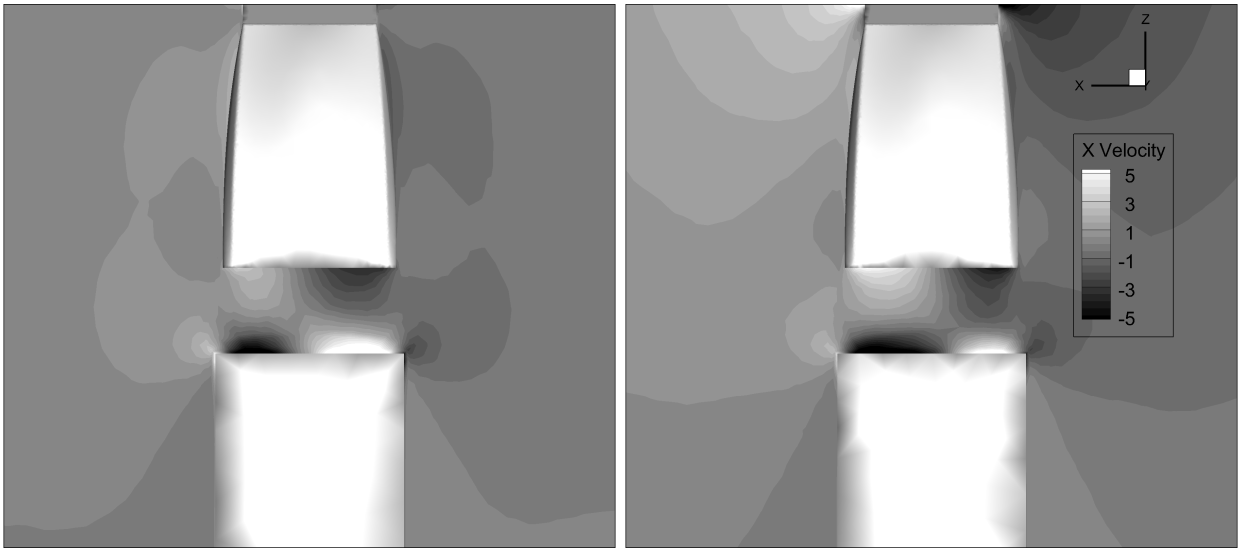

(a) Rear Vehicle – 10 ft
(b) Rear Vehicle – 90 ft

Figure 5.12: Two vehicle trailer front X velocity

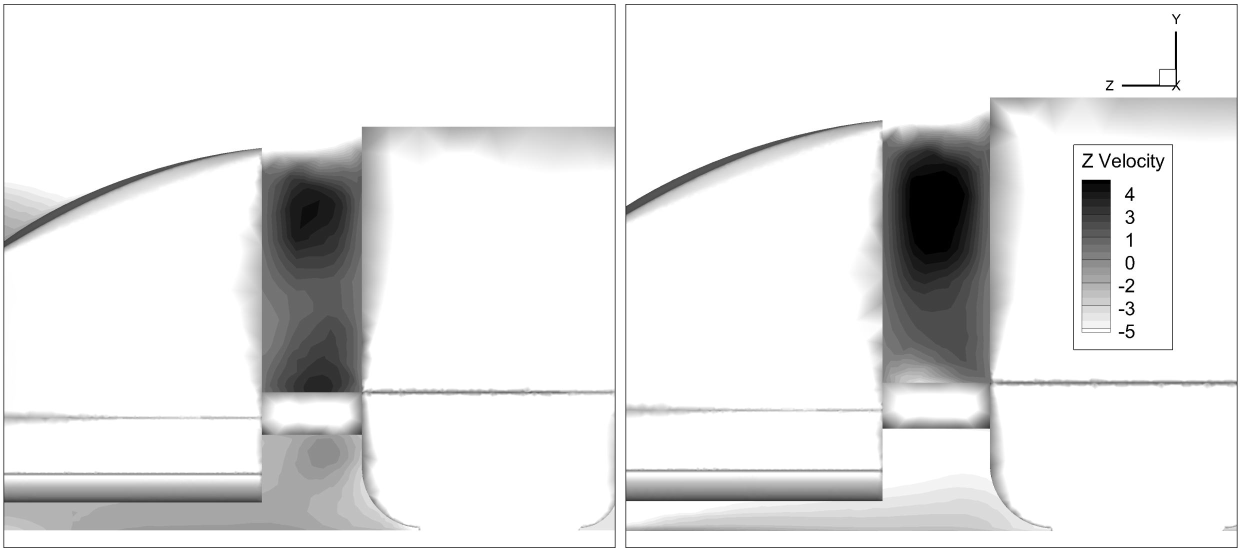

(a) Rear Vehicle – 10 ft
(b) Rear Vehicle – 90 ft

Figure 5.13: Two vehicle trailer front Z velocity

The X component of velocity provides little insight into the pressure differential between the cases. It only shows that the in the 10 ft simulation the right-hand side slightly dominates and the left-hand side is more prominent in the 90 ft. This is not significant as both simulations remain balanced and the average effect is identical.

The Z component, on the other hand, shows that there is a significant portion of the flow travelling against the freestream within the tractor-trailer gap, which could be resulting in the low pressure “pulling” effect on the trailer front surface.

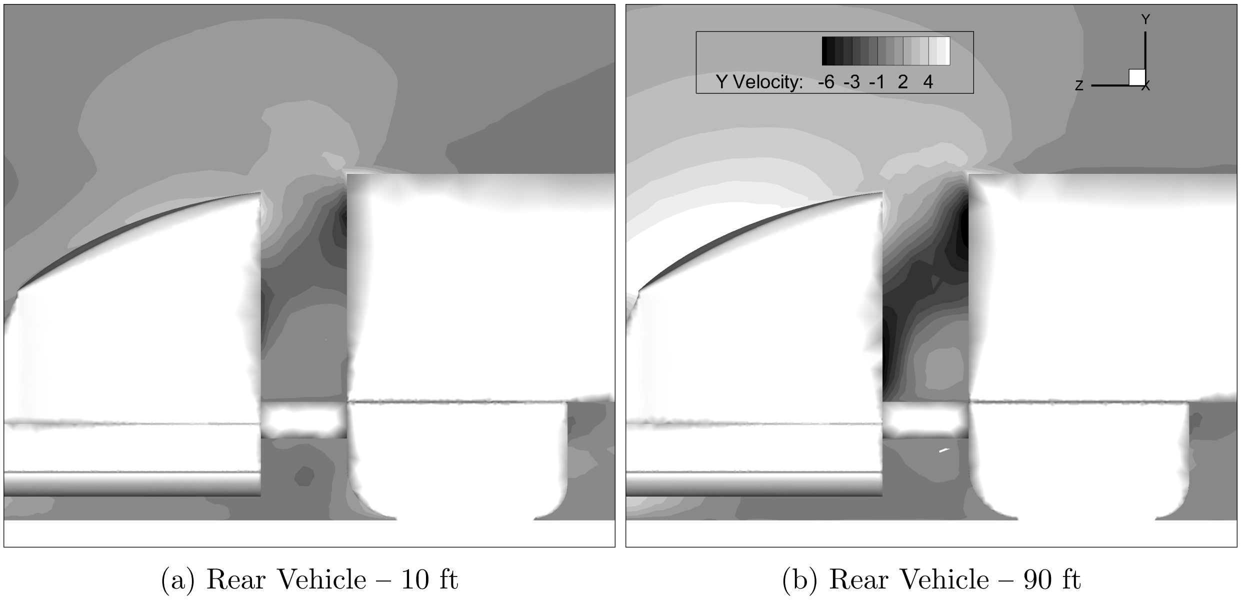

(a) Rear Vehicle – 10 ft

(b) Rear Vehicle – 90 ft

Figure 5.14: Two vehicle trailer front Y velocity

The Y velocity has the most varied distribution of the velocity components. Not only is there a significant variation in magnitude, the profile shape is wholly unexpected. It shows that the flow changes directions several times within the tractor-trailer cavity, indicating complex flow features that could be responsible for the large pressure variation.

Keeping this in mind, each component of vorticity was examined. Beginning with Y vorticity (rotation about the Y axis) and concluding with Z vorticity, Figures 5.16–5.17 depict the rotationality of the flow in multiple planes.

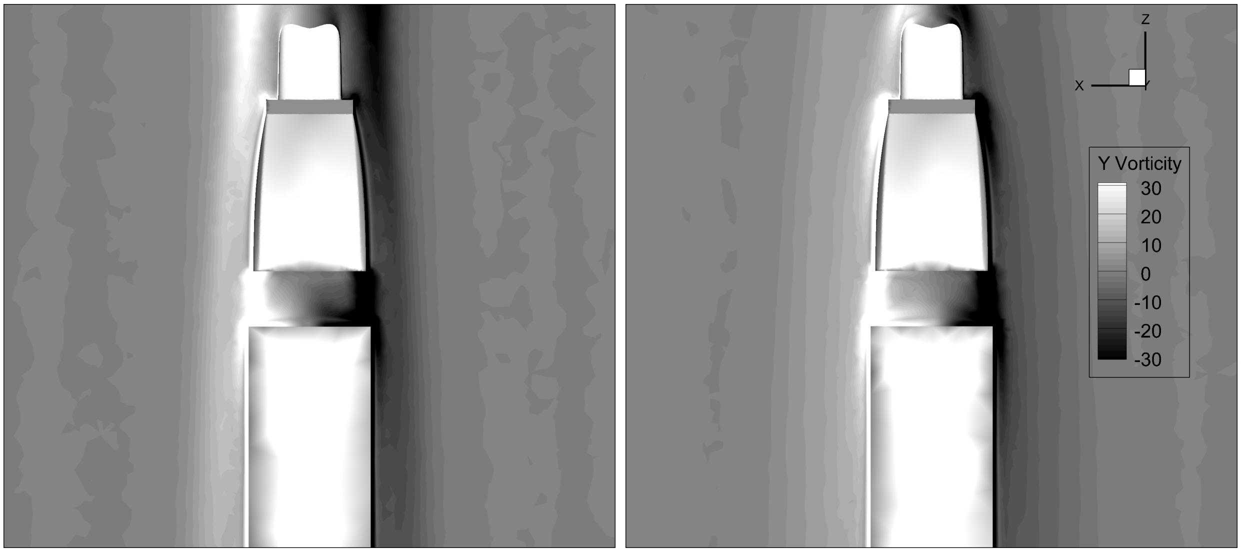

(a) Rear Vehicle – 10 ft (b) Rear Vehicle – 90 ft

Figure 5.15: Two vehicle trailer front Y vorticity

Figure 5.15 confirms an expected result: there are two counter-rotating vortices that are pulled into the tractor-trailer gap from the sides of the vehicle. These vortices are very well defined, at least in the Y rotational frame.

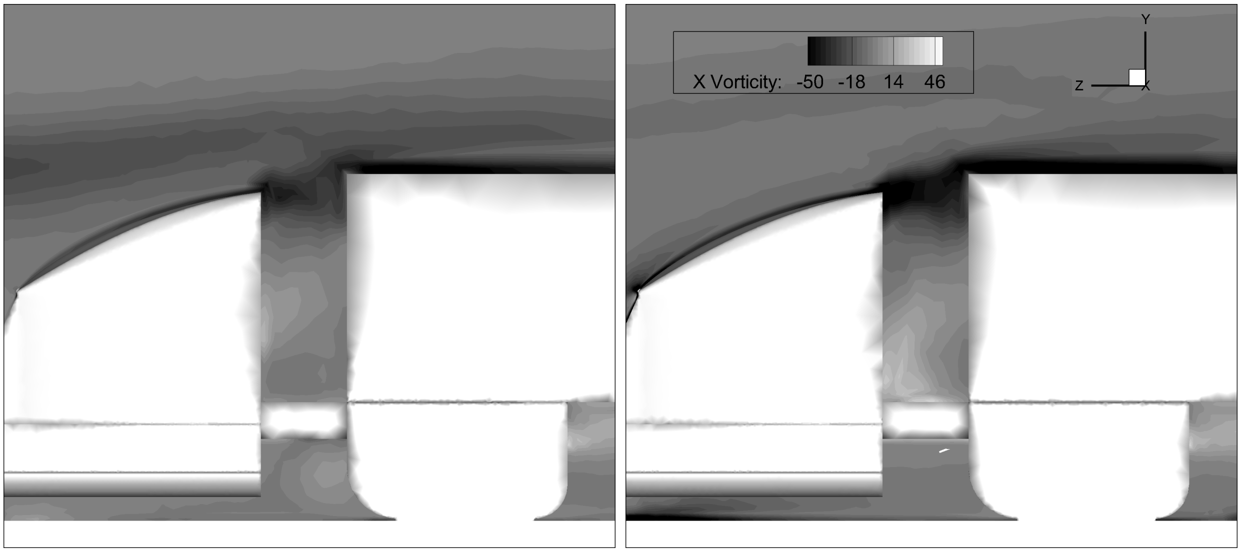

(a) Rear Vehicle – 10 ft (b) Rear Vehicle – 90 ft

Figure 5.16: Two vehicle trailer front X vorticity

Because the positive X direction is out of the page (as shown in Fig. 5.15), the side view presented in Fig. 5.16 shows that there is no counterclockwise X rotation in either case, that is the flow is not rotating against the freestream. This is significant because it eliminates the possibility of a counter rotating flow "pulling" on the trailer front surface, creating the pressure imbalance that exists between the 10 ft and 90 ft cases. A slight change magnitude is the primary difference between the flows.

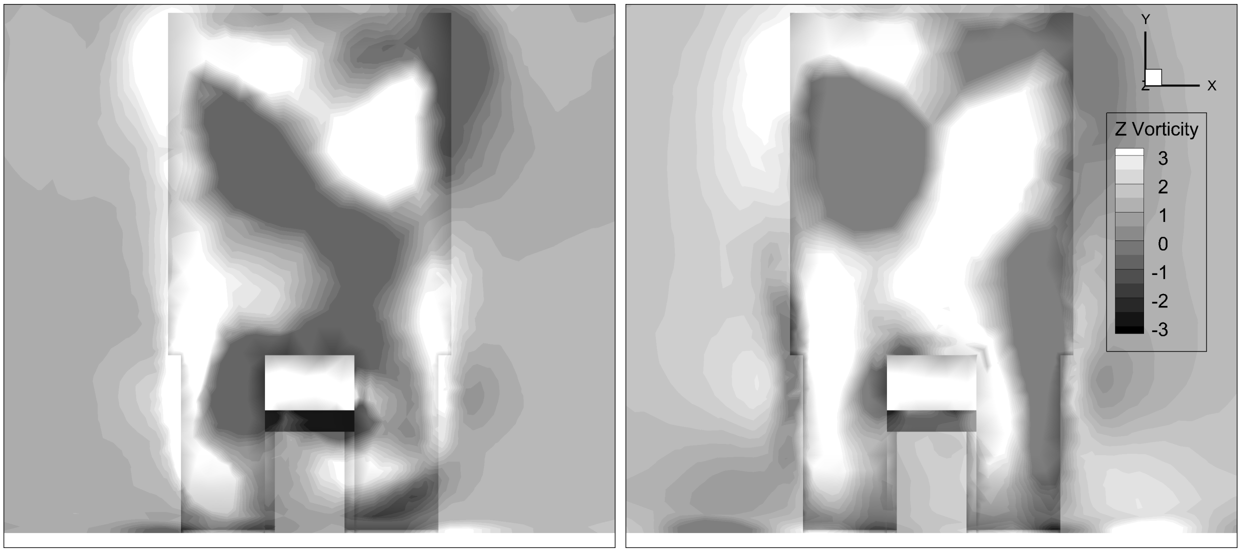

(a) Rear Vehicle – 10 ft

(b) Rear Vehicle – 90 ft

Figure 5.17: Two vehicle trailer front Z vorticity

The information displayed by the Z vorticity plot shown in Fig. 5.17 is somewhat hard to discern initially, aside from presenting a mirror image plot confirming inverse vortex dominance suggested by the X velocity of Fig. 5.12.

However, considering the right half of the 90 ft case provides understanding into the vortex structure. As with the X vorticity, positive Z spatially is out of the page, which indicates a counterclockwise rotation in the center and a clockwise motion on the upper outer edges. This reveals that the vortex Z rotation actually reverses directions as it nears the top surface of the trailer.

This is very telling when combined with the known information about the velocity vector, particularly the Y velocity component shown in Fig. 5.14. It states that the vortex is multi-directional: flow is pulled from the under-carriage into a tight vortex core and funneled upwards until it encounters the air flowing over the tractor, which effectively acts as a solid wall, forcing the flow to turn downward.

Only a small portion of the flow can turn and return to the freestream in the X direction for two reasons. Firstly, a large potion of the outer side flow is already being channeled into the gap to form the large vortices depicted by Fig. 5.15. Secondly, the side flow that is not impinging on the trailer or contributing to the vortices acts in a similar manner to the upper flow: a boundary that the now trapped flow cannot cross.

The only remaining direction for the flow to divert is down. The flow from the undercarriage reverses direction by increasing the rotation radius and joining the larger side vortex, which is also forced downwards. The flow then circulates downward, passing under the trailer, and continues into the wake. A streamline from this multi-directional vortex is shown below in Fig. 5.18 for the 10 ft case.

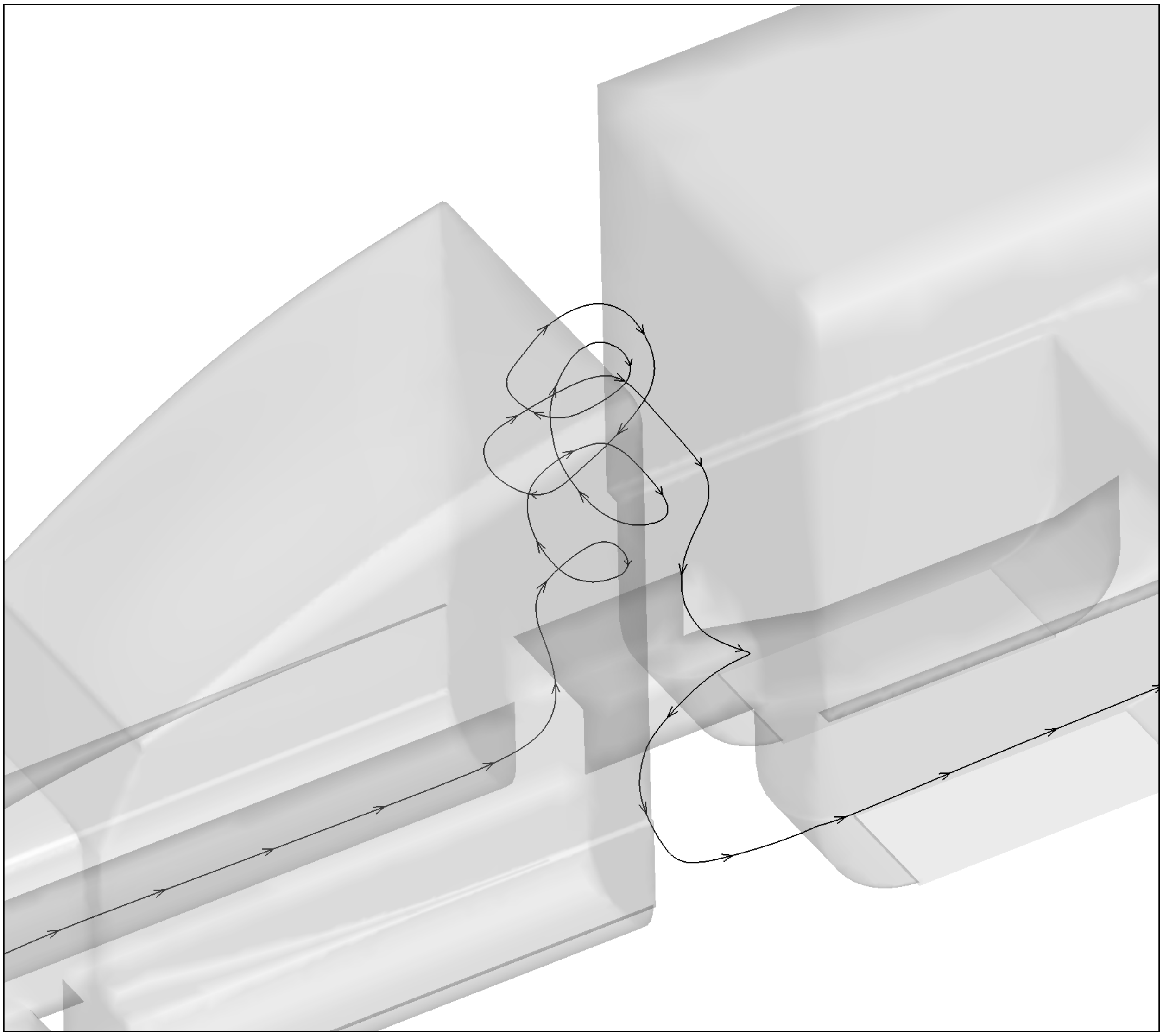

Figure 5.18: Two vehicle rear vehicle trailer front streamline – 10 ft

Though this is a significant finding, it still does not fully explain the large pressure discrepancy between the two test cases, thus more fundamental parameters are needed: the pressure distribution and the pressure gradient. The primary gradient of interest is the Z pressure gradient, which indicates pressure change in the stream-wise direction. These variables are graphed below in Fig. 5.19 and Fig. 5.20 respectively.

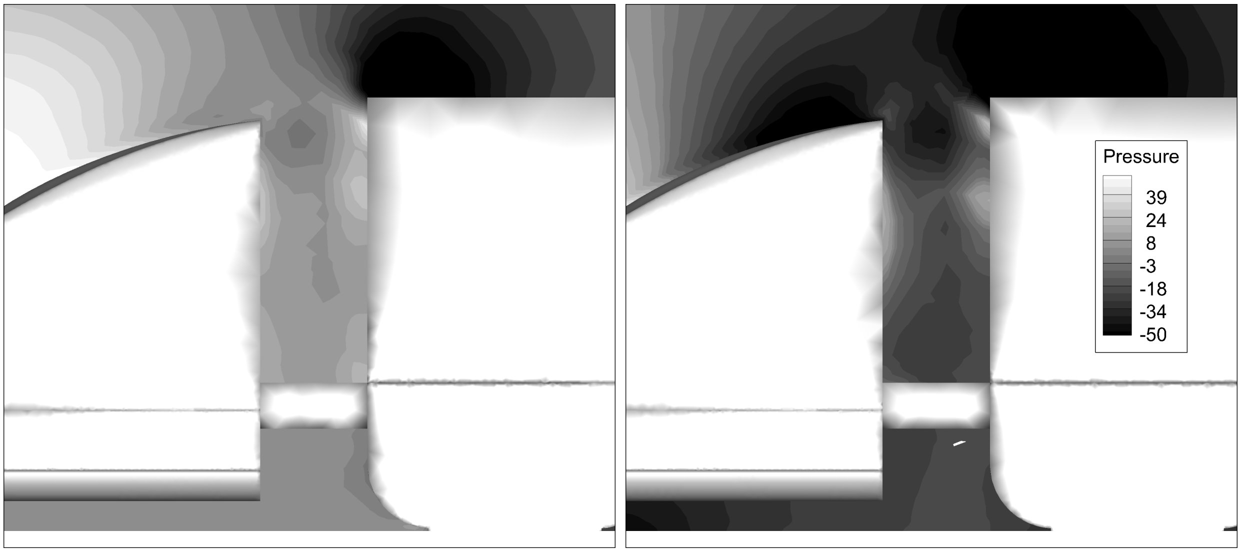

(a) Rear Vehicle – 10 ft (b) Rear Vehicle – 90 ft

Figure 5.19: Two vehicle trailer front pressure distribution

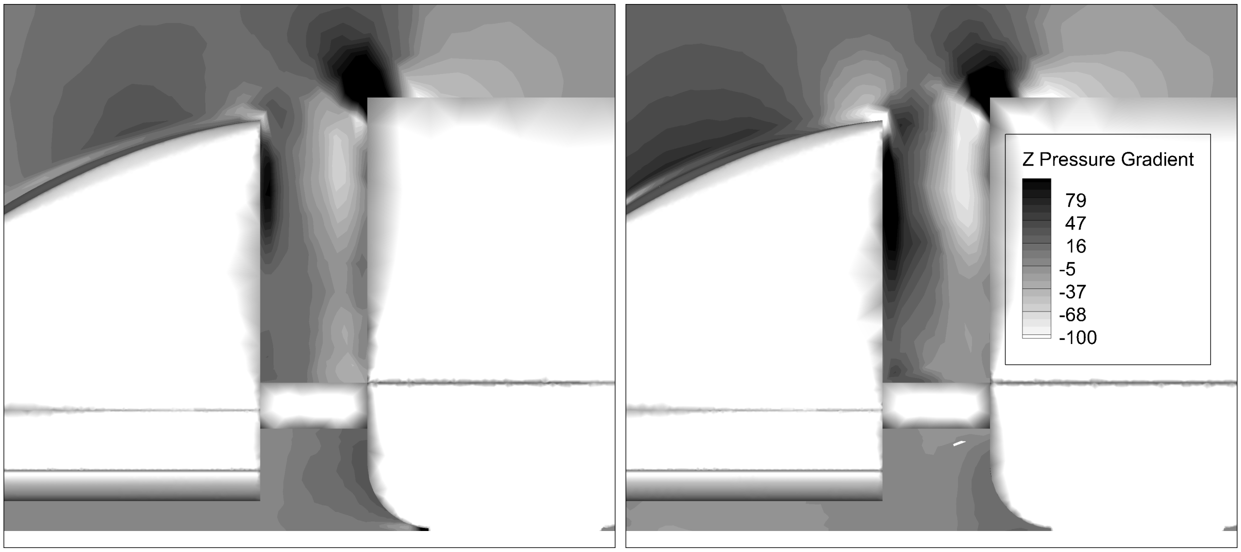

(a) Rear Vehicle – 10 ft (b) Rear Vehicle – 90 ft

Figure 5.20: Two vehicle trailer front Z pressure gradient

The profiles seen in Fig. 5.19 are starkly different: the 90 ft case has a significantly lower overall pressure than the 10 ft simulation. This was predicted from examining the surfaces pressures presented in Fig. 5.10 and the cause can be drawn qualitatively from a conservation of energy approach. The high freestream velocity of the re-established flow in the 90 ft simulation results in large directional velocity components and large vorticity (which is defined as the curl of velocity per Eq. (5.2)). Because a large portion of the flow energy is kinetic energy, the result is a lower static pressure.

The reverse is true for the 10 ft case, where the flow is still very disrupted from the front vehicle and has a much lower mean velocity. This translates to less flow kinetic energy and significantly higher static pressure.

What was unanticipated, however, are the pressure gradients shown in Fig. 5.20. The gradient in the 90 ft case is significantly larger, which, at first glance, does not seem to align with a lower pressure force on the surface of the larger separation distance cases. Logically, a larger change in pressure would result in a larger final pressure at the vehicle surface.

Thus it is useful to examine Crocco's theorem once again to determine and validate the cause of pressure gradient differential. Expressing the Cartesian Z component of Eq. (5.4) results in:

$$p_z = \rho(v_x\omega_y - v_y\omega_x) - \frac{1}{2}\frac{\partial}{\partial z}\left(v_x^2 + v_y^2 + v_z^2\right) \tag{5.5}$$

From the profiles discussed above, the main contributors in to differences in this equation are clear: y velocity v_y, y vorticity ω_y, and z velocity v_z, all of which are significantly larger in the 90 ft case. This indeed confirms the large gradient, but does not explain the unintuitive lower pressure.

Upon closer examination, there are two causes that the large gradient does not result in a large surface pressure. Firstly, the distance is short: only approximately 1 m from the rear surface of the tractor to the front surface of the trailer. Over short distances, even very large gradients can are limited in their effects.

Secondly, though the gradient is exaggerated in the 90 ft case, there are significant positive and negative regions. The consequence of this is a "hills and valleys"-type effect. Though the regions in the 90 ft case may be significantly deeper or higher than the 10 ft case, the average is roughly the same: small. Averaging across the 2.5 m height line, for instance, yields a high and low pressure gradient of 72 Pa/m and -15 Pa/m, but an average increase of only 14 Pa/m across the gap.

In conclusion, it can be stated that the lower mean flow velocity of the 10 ft case has two effects on the pressure: a high static pressure and a low pressure gradient in the cavity region. This causes a high static pressure on the surface because the gradient has little effect on the static pressure.

Conversely, the high mean flow velocity of the 90 ft case results in a low static pressure and a high pressure gradient. If given a larger separation between tractor and trailer, this high gradient might well change the pressure distribution on the surface to result in a larger force than on the 10 ft. However, because the distance and gradient average are small and the static pressure is much lower than that of the smaller vehicle separation cases, the adverse gradient is unable to have a significant effect on the pressure and the resulting force for the 90 ft simulation is 1/3 of its 10 ft counterpart.

If these consequences are considered with the single truck case, they can at first seem erroneous, as the single tractor-trailer front, the vehicle with the highest velocity, experiences the most drag, similar to that of the 10 ft separation case. This is the opposite of the results found above: the increased mean flow of the 90 ft trailer resulted in a lower force. While it is true that the static pressure in the vortex region is very low due to the high velocity, the gradient is also significantly larger than that of the 90 ft, resulting in a high pressure at the wall, even over the short distance between the tractor and trailer. This highlights the non-linearity of pressure-velocity relationship in rotational flows.

Figure 5.21 below illustrates the comparison between gradients. An off-center plane was chosen to fully illustrate the difference between the rear vehicle of the 90 ft and the single vehicle simulations.

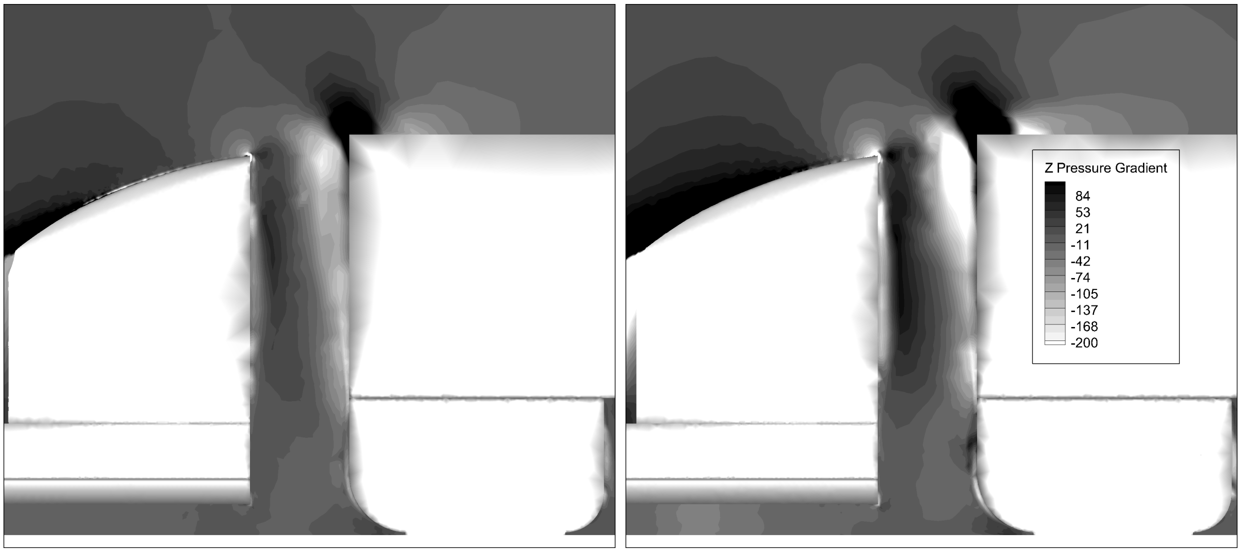

(a) Rear Vehicle – 90 ft (b) Single Vehicle

Figure 5.21: Two vehicle trailer front Z pressure gradient – single and 90 ft comparison

5.3 Three Vehicle Platoons

After the two identical vehicle models had been fully explored, the simulation geometry was expanded to three Peterbilt 579 tractor-trailers to investigate the aerodynamic effects of a third body on the platoon as a whole and to determine if the drag benefits experienced by the two vehicle configuration could be extended to a three vehicle configuration. The resulting model is shown in Fig. 5.22 as an isometric view for a separation distance of 20 ft between each vehicle.

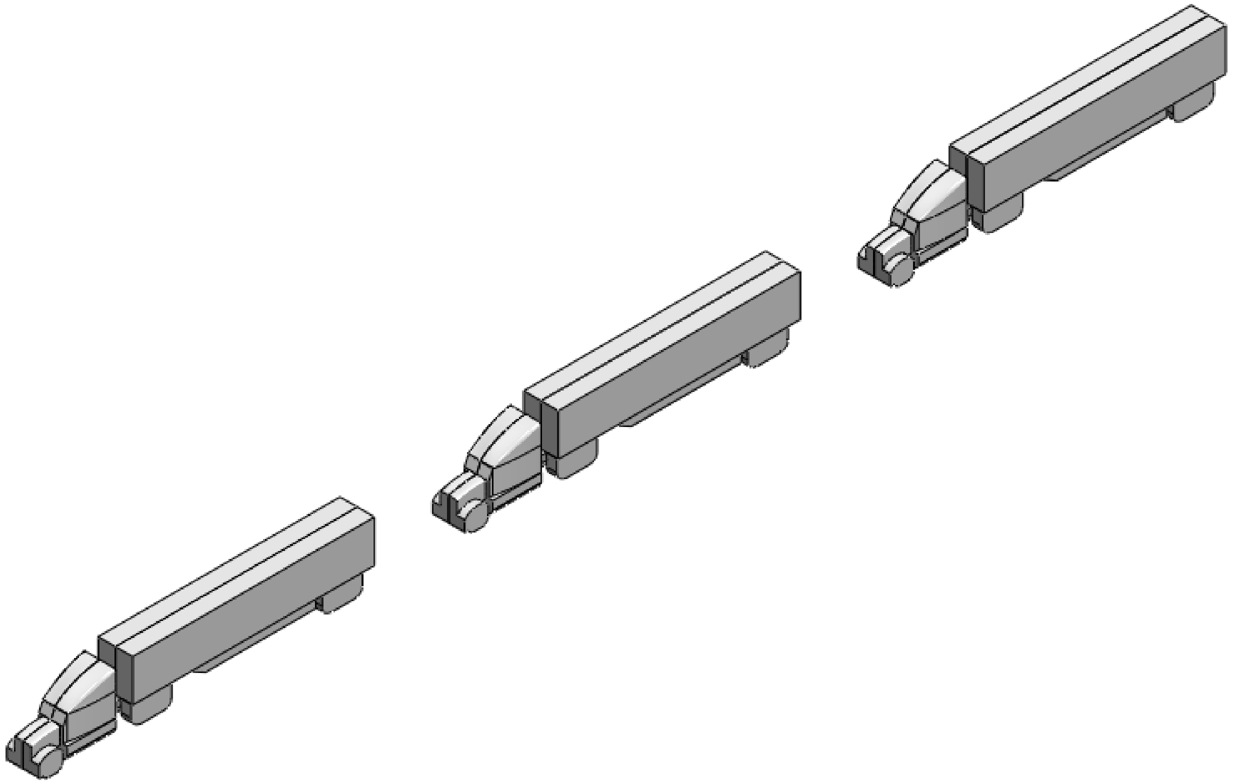

Figure 5.22: Three vehicle CAD model – 20 ft separation

Two primary cases were considered: homogeneous and heterogeneous separation distances. Homogeneous cases were simulations where separation distance was equal, e.g. if the distance between Vehicle 1 and Vehicle 2 was 40 ft, then the distance between Vehicle 2 and Vehicle 3 was also 40 ft.

Heterogeneous separation distance models, on the other hand, were cases where vehicle distances were not related. An example of a heterogeneous case tested is a distance of 20 ft between Vehicles 1 and 2 with a distance of 80 ft between Vehicles 2 and 3. These models were examined in order to determine if a link between nonadjacent vehicles existed, i.e. if Vehicle 1 and 2 spacing affected Vehicle 3. Due to the sheer number of combinations that arise when considering non-identical spacing, only a limited number of test cases were simulated.

5.3.1 Homogeneous Separation Distance

Seven equidistant cases were simulated ranging from 20 ft to 80 ft in increments of 10 ft. The resulting drag coefficients are shown as a percentage of single vehicle drag below in Fig. 5.23. The normalized drag coefficients for Vehicle 1 and 2 from the two vehicle simulations are also included for comparison.

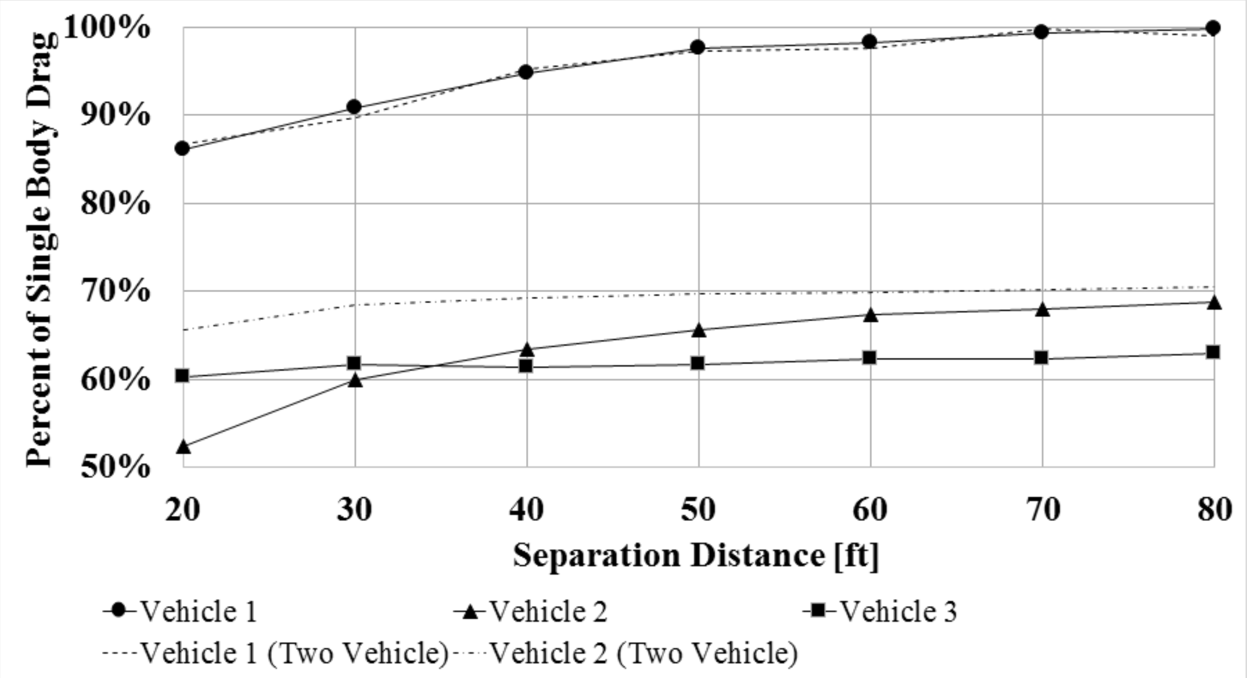

Figure 5.23: Three vehicle drag as a percent of single body drag

Examining the first vehicle shows near identical drag predictions to the two body simulations. This speaks to the independence of the first vehicle from all other vehicles except for the immediately following tractor-trailer. It states that the first body will always see the most drag and can only be assisted by a close following of the second vehicle. This is a common thread that has been found in all simulations and is expected from a low speed, incompressible flow with such a large solid body length scale.

Considering the second and third body drag at greater distances also provides anticipated results: the drag experienced by Vehicle 2 is very similar to the two body simulation and is a consequence of the lower mean velocity encountered by the tractor. The mean flow behind Vehicle 2 is even lower velocity and thus Vehicle 3 has still lower pressure force, as seen in Fig. 5.24.

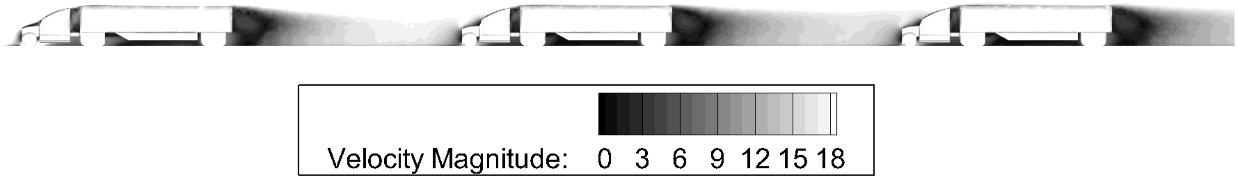

Figure 5.24: Three vehicle drag velocity magnitude – 80 ft

The drag decrease from Vehicle 1 to Vehicle 2, approxmately 30%, is much larger than the Vehicle 2 to Vehicle 3 reduction, roughly 7%. The reason for this is twofold; the first being that the velocity magnitude reduction from 10 ft in front of Vehicle 1 to 10 ft ahead of Vehicle 2 is nearly 50% (30 m/s to 17 m/s), whereas the velocity if only reduction by about 10% from Vehicle 2 to Vehicle 3 (17 m/s to 15 m/s). This in and of itself is a significant change but is compounded by a second factor: force scales with velocity squared. Mathematically, this translates to large changes, such as a 50% reduction, being amplified and small changes, e.g. 10%, being deemphasized.

The close distance results presented for the following bodies in Fig. 5.23 are initially perplexing, but prove to be sound when logically examined with knowledge previously acquired. The second vehicle has a lower pressure force than the following body. The cause of this relates back to the influence of each body: Vehicle 2 is receiving benefits on the frontal and rear surfaces from simultaneously leading and following, whereas Vehicle 3 only experiences a reduction in frontal tractor drag from following Vehicle 2.

The final aspect of Fig. 5.23 that warrants investigation is the third body drag, which appears to be nearly constant, regardless of separation distance. To probe into the cause of this consistent drag, the pressure force surface composition for Vehicle 3 was examined for the 20 ft and 80 ft separation cases, which is shown in Fig. 5.25.

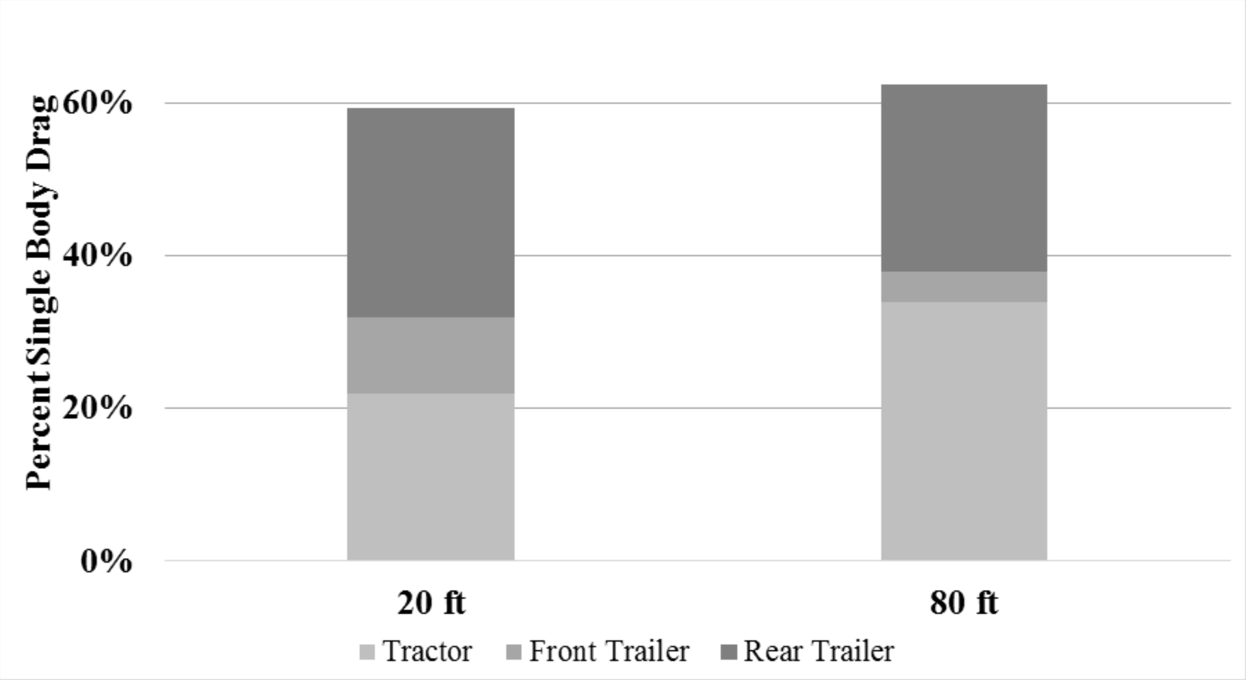

Figure 5.25: Third vehicle drag composition by surface

The rear trailer stays constant as expected, composing approximately 45% of the overall third vehicle drag, which is 60% of the single truck drag. The tractor drag also behaves as expected, increasing as distance increases. The key to understanding the reason for roughly constant drag lies in the multi-directional vortex phenomenon that appears between the tractor and the trailer. This flow feature causes large amounts of drag at low speeds and was discussed in Sec. 5.2.3. Whereas in the two vehicle simulation, the drag reduction on the tractor was more than enough to compensate for the increased drag on the trailer front, this is not the case for the third vehicle. Though the pressure force on the tractor is lower for the third vehicle than the second, the force magnitude on the trailer front surface is roughly the same, thus composing a larger percentage of drag and having a more significant effect. The large trailer front drag at small spacings thus overcomes the reduced tractor drag to affect a larger drag coefficient.

This introduces an important disparity that must be addressed: relative and absolute reduction. Thus far, only absolute changes have been addressed, all results discussed were the normalized by the single truck drag for comparison on an equal basis. Relative change, however is equally important to determine inter-vehicle trends. Two types of relative change were examined: a single vehicle drag change for multiple distance cases and drag change across multiple vehicles at a single distance.

To expound upon these classifications, a single-vehicle-multi-distance (SVMD) metric would be the change in frontal pressure drag for Vehicle 2 between 20 and 80 ft simulations. This could then be compared to the frontal drag change for Vehicle 3 between 20 and 80 ft. A multi-vehicle-single-distance (MVSD) example would be the rear drag change between Vehicle 1 and Vehicle 2 at a 20 ft spacing, which could likewise be compared to the rear surface difference between Vehicle 2 and 3.

Six separate comparisons were identified as significant and are listed below in Table 5.2 and Table 5.3. Three SVMD and three MVSD parameters were chosen to fully explain the surface drag trends, relative changes such as SVMD Vehicle 1 frontal drag were not examined as there was little change and nothing of importance to be gained from analysis.

Table 5.2: Single vehicle, 20 – 80 ft distance variation relative change

Vehicle	**Percent Reduction across Distance**
	Tractor
Vehicle 2	37.6%
Vehicle 3	35.2%
	Trailer Front
Vehicle 2	-137.4%
Vehicle 3	-146.7%
	Trailer Rear
Vehicle 1	43.6%
Vehicle 2	36.1%

Note that distance-varied trailer front surface drag decreases significantly for both Vehicle 2 and Vehicle 3; this is because of the known vortex formation that was analyzed thoroughly and discussed in Sec. 5.2.3.

Examining Table 5.2 shows an interesting trend: the relative drag decrease for each vehicle as separation distance increases are surprisingly similar, despite not being related. This indicates that the flow structures around each vehicle, while varying in magnitude, are otherwise very similar causing roughly the same amount of proportional drag.

Table 5.3: Multiple vehicle, single distance relative change

Surface	**Percent Force Reduction Between Vehicles**	
	Vehicle 1 → Vehicle 2	**Vehicle 2 → Vehicle 3**
	20 ft Separation	
Tractor	55.2%	8.2%
Trailer Front	24.4%	5.1%
Trailer Rear	9.7%	-68.8%
	80 ft Separation	
Tractor	29.0%	11.6%
Trailer Front	68.1%	8.7%
Trailer Rear	20.2%	3.6%

Analyzing the tractor surface region shows that Vehicle 2 is very sensitive to the spacing: the mean velocity behind Vehicle 1 increases to a significant percent of the freestream value, which is shown by contrasting the 55% drag reduction at 20 ft with the 29% at 80 ft. Vehicle 3 on the other, sees very similar tractor drag reduction from Vehicle 2 at 20 and 80 ft spacings, suggesting that Vehicle 2 further disrupts the flow and the low speed velocity is unable to recover significantly in the additional 60 ft of spacing. This proposes that additional platoon vehicles can experience similar drag benefits at farther distances, but also that the total benefit received is asymptotically limited.

Continuing with the trailer front shows that at low speed deltas the drag changes little, such as the velocity difference between Vehicle 2 and 3, but at large speed differences changes very rapidly, such as the deviation between Vehicle 1 and 2. This implies a highly nonlinear behavior, which is expected due to the known presence of large amounts of vorticity results from the application of Crocco's theorem.

On the third surface, the trailer rear, the reason for the reduced Vehicle 2 drag at close spacing is confirmed: Vehicle 3 actually sees an increase in drag from Vehicle 2 at a 20 ft separation. At the 80 ft spacing, the drag is very similar on Vehicle 2 and 3 and stronger on Vehicle 1. This again indicates that there is a larger mean flow reduction between Vehicle 1 and 2 and a much more limited reduction between Vehicle 2 and 3.

5.3.2 Heterogeneous Separation Distance

Because of the limited nature of the inquiry regarding non-homogeneous separation distances only two cases were analyzed. The first model was a 20 ft-80 ft separation between Vehicle 1 and 2 and Vehicle 2 and 3, respectively. The second test case, using the same notation was an 80 ft-20 ft simulation. The resultant drag coefficients are shown below in Fig. 5.26, again as a percentage of single truck drag.

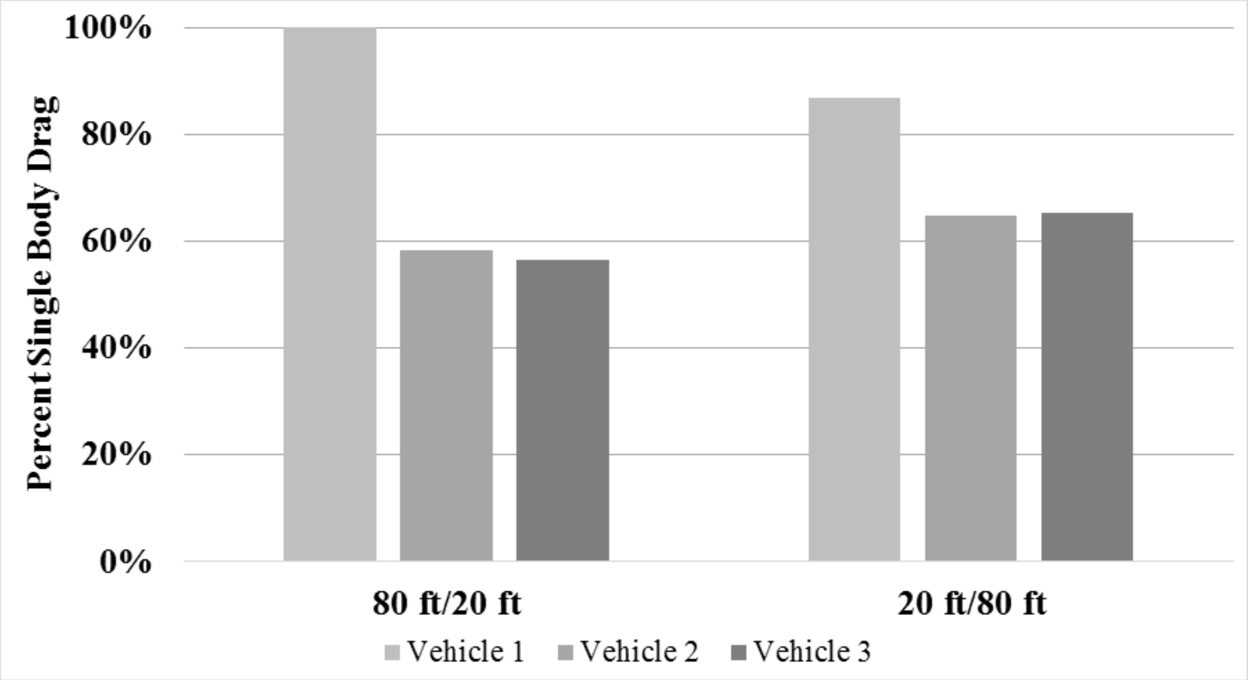

Figure 5.26: Three vehicle drag

Figure 5.26 depicts the exact behavior expected for Vehicle 1 and Vehicle 3. In the 80/20 case, Vehicle 1 experiences no benefit as Vehicle 2 is distant while Vehicle 3 experiences a large benefit because it is in the wake of Vehicle 2. For the 20/80 simulation, Vehicle 1 sees drag reduction because Vehicle 2 is interfering with wake formation. The third tractor-trailer sees the opposite, an increase in drag, when moving from the 80/20 to the 20/80 case, which is also as expected: Vehicle 3 has moved out of the Vehicle 2's wake and into its slipstream.

In order to gain more quantitative insight into the drag force on Vehicles 1 and 3, the drag coefficients from the 20 ft and 80 ft homogeneous separation distance were compared to the drag coefficients from Fig. 5.26. The results are graphed in Fig. 5.27 along with the percentage change in each prediction.

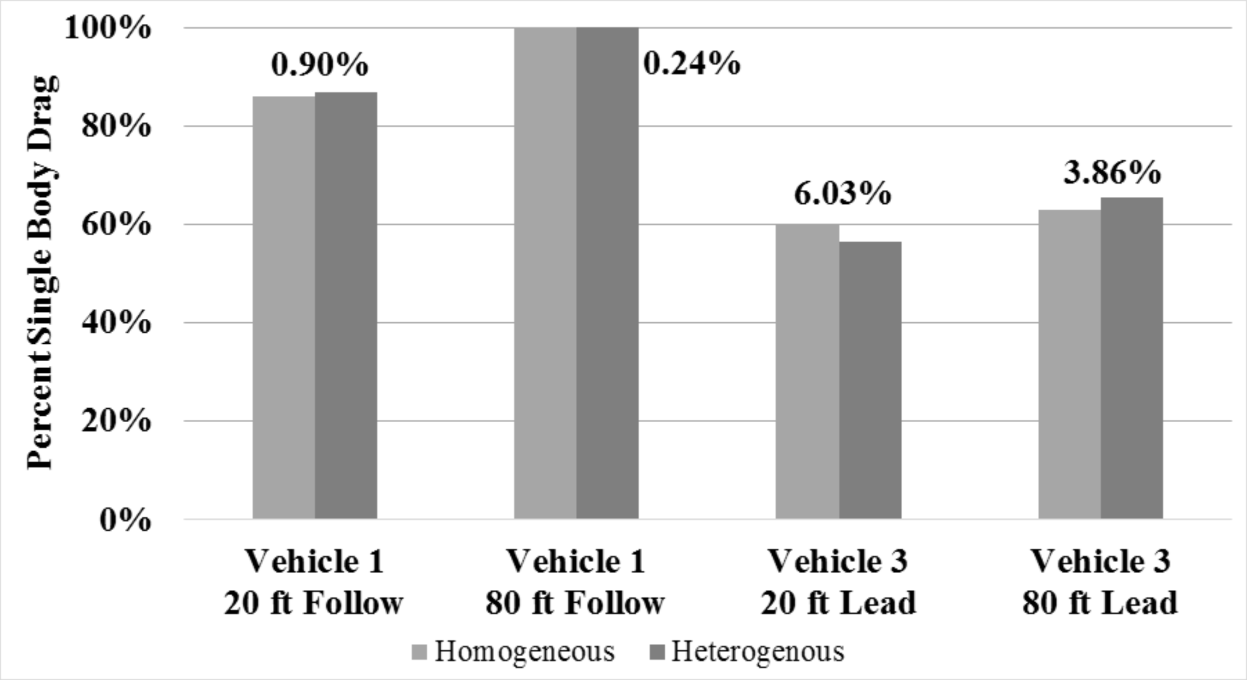

Figure 5.27: Vehicle 1 and Vehicle 2 equidistant and non-equidistant drag comparison

The variation in drag prediction for Vehicle 1 was less than one percent in both cases, effectively proving that Vehicle 1 is independent of Vehicle 2 and 3 spacing. The drag force fluctuation on Vehicle 3 is slightly increased and suggests there is a low dependence on anterior vehicle spacing beyond gridding differences.

This makes it clear what was suspected initially: a vehicle is independent of trailing bodies beyond the adjacent in the platoon and is only weakly dependent on preceding vehicles beyond the immediate neighbor. This is congruent with what is known about low speed, incompressible flow and has implications for larger platoons.

Vehicle 1 and Vehicle 3 could be compared directly to the equidistant 20 ft and 80 ft simulations, as there are no additional bodies affecting the pressure force they experience. Vehicle 2, however, cannot be directly compared to either of the relevant homogeneous cases because it is a hybrid of the two cases: either 80 ft from the front and 20 ft from the rear vehicle or vice versa. Thus, one must again resort to surface drag analysis to compare the heterogeneous and homogeneous cases.

Examining 20 ft spacing from Vehicle 2 requires using the front surfaces, the tractor and trailer front, from the 20 ft / 80 ft case and the trailer rear surface from the 80 ft / 20 ft simulation. Conversely, examining an 80 ft spacing requires the front surfaces from the 80/20 and the rear from the 20/80. Figure 5.28 below shows the results of comparing these partial cases.

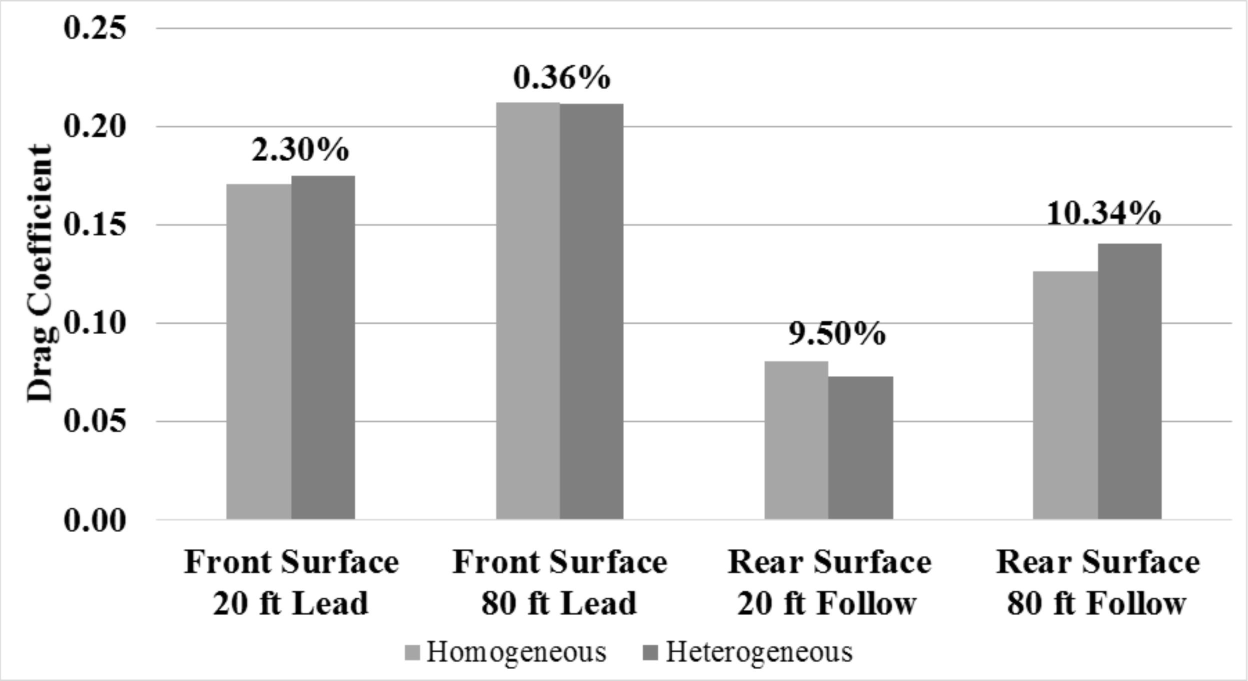

Figure 5.28: Vehicle 2 equidistant and non-equidistant surface drag comparison

As seen before, there is virtually no frontal influence on the front surface of Vehicle 2 from Vehicle 3 at any spacing. The difference in prediction can be accounted for via numerical error and gridding differences.

The rear surface of Vehicle 2, however, does see a noticeably different drag depending on the spacing of Vehicle 1. The drag prediction for the rear surface decreases as Vehicle 1 moves farther away; both the 20 ft and 80 ft following vehicle cases saw more drag when Vehicle 1 was closer rather than farther. This is the same trend seen in Fig. 5.27, albeit exaggerated. Though the differences are slight, this phenomenon can be related back to

Crocco's theorem. The Z component of the pressure gradient is shown below in Fig. 5.29 to illustrate this fact. Vehicle 3 is 20 ft behind Vehicle 2 in both of the distributions.

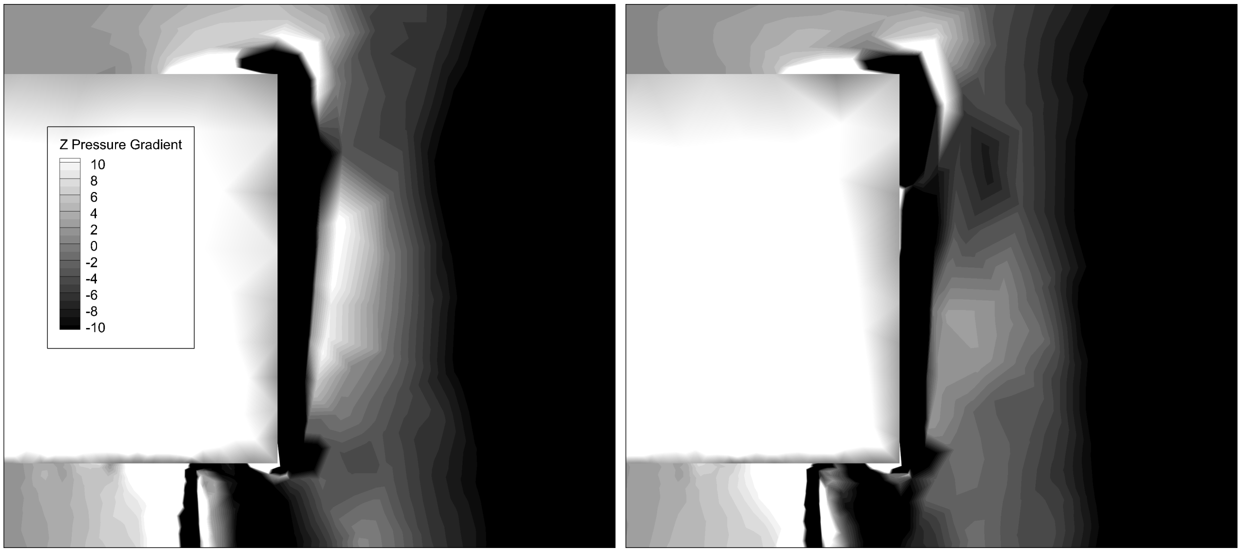

(a) Vehicle 1 Distance: 20 ft (b) Vehicle 1 Distance: 80 ft

Figure 5.29: Vehicle 2 trailer rear Z pressure gradient comparison

Figure 5.29a has increased drag over Fig. 5.29b because though they both have severe decreases in pressure gradient near the surface, there is a higher magnitude gradient immediately outside this region in the 20 ft case. Because the near-wall gradient profiles are similar, this high change region essentially creates a higher starting pressure as one approaches the wall, resulting in a high drag force at the surface. As seen from Eq. (5.5) this higher gradient is the result of the high vorticity and in the region immediately behind Vehicle 2. The velocity in the Vehicle 2 rear trailer region is also marginally lower in the 20 ft simulation than the 80 ft, due to the 20 ft flow being highly disrupted when encountered by Vehicle 2.

5.4 Multiple Geometry Platoons

The final branch of analysis performed for this research was variation of tractor geometry. The secondary single vehicle cases examined in Chapter 4 were placed into the two vehicle model, meshed, and simulated within Fluent.

For each of the test cases only the rear vehicle was varied because the lead tractor drag is largely independent of the following vehicle, as seen in Sec. 5.2. This leads to the conclusion that changing the lead vehicle tractor would have no effect on the overall drag of that vehicle as the lead tractor cannot be affected by any vehicle in the platoon.

5.4.1 Peterbilt 379

The two body model for the Peterbilt 579–Peterbilt 379 is shown below in Fig. 5.30 at a distance of 20 ft. Using this model, four test distances were simulated, from twenty to eighty feet in increments of twenty.

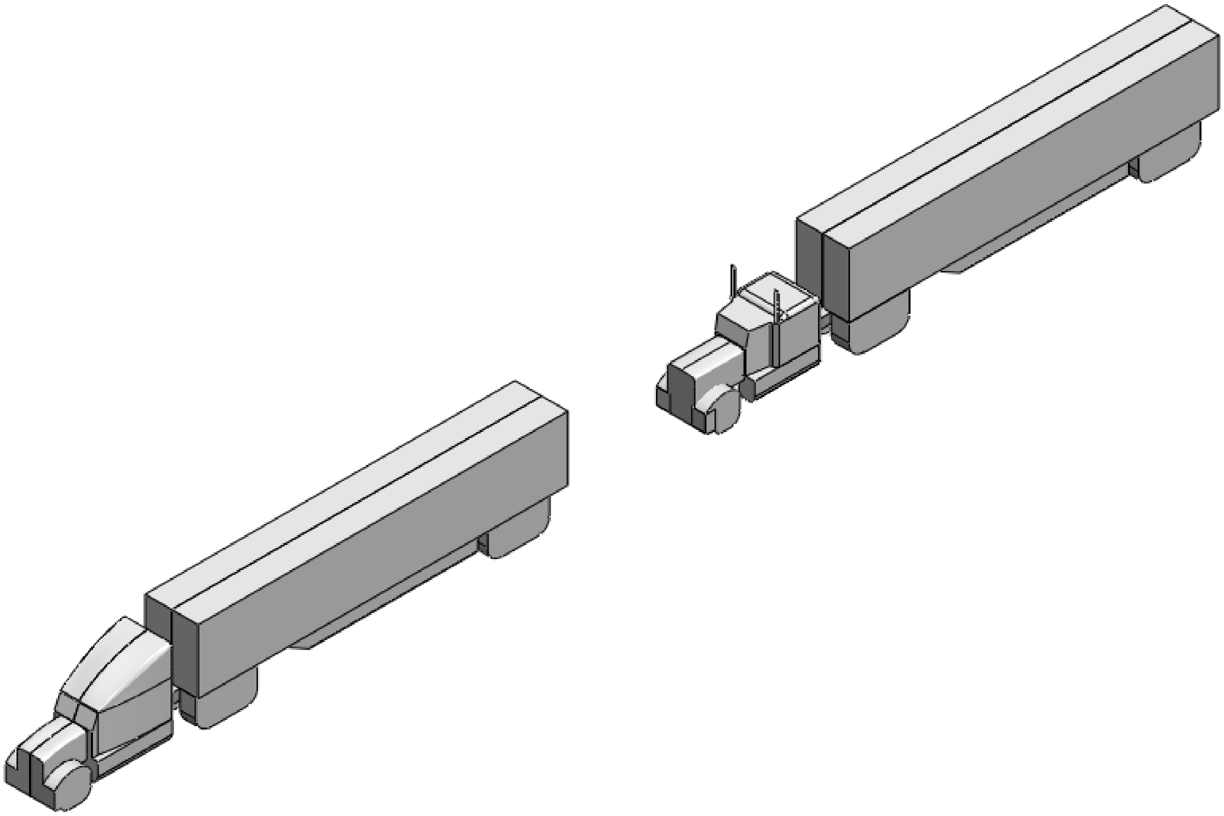

Figure 5.30: P579 / P379 CAD model – 20 ft separation

The drag results are shown below in Fig. 5.31. Because each vehicle has a slightly different projected area, using a drag coefficient when comparing multiple vehicles is inconvenient and misleading because the nondimensionalization coefficients are not identical. This loses the generality of scale independence, but it is necessary to correctly present the information. The freestream dynamic pressure was constant in each case ($\rho_\infty = 1.225$ kg/m^3, $v_\infty = 30$ m/s) and the units of force are Newtons. (N)

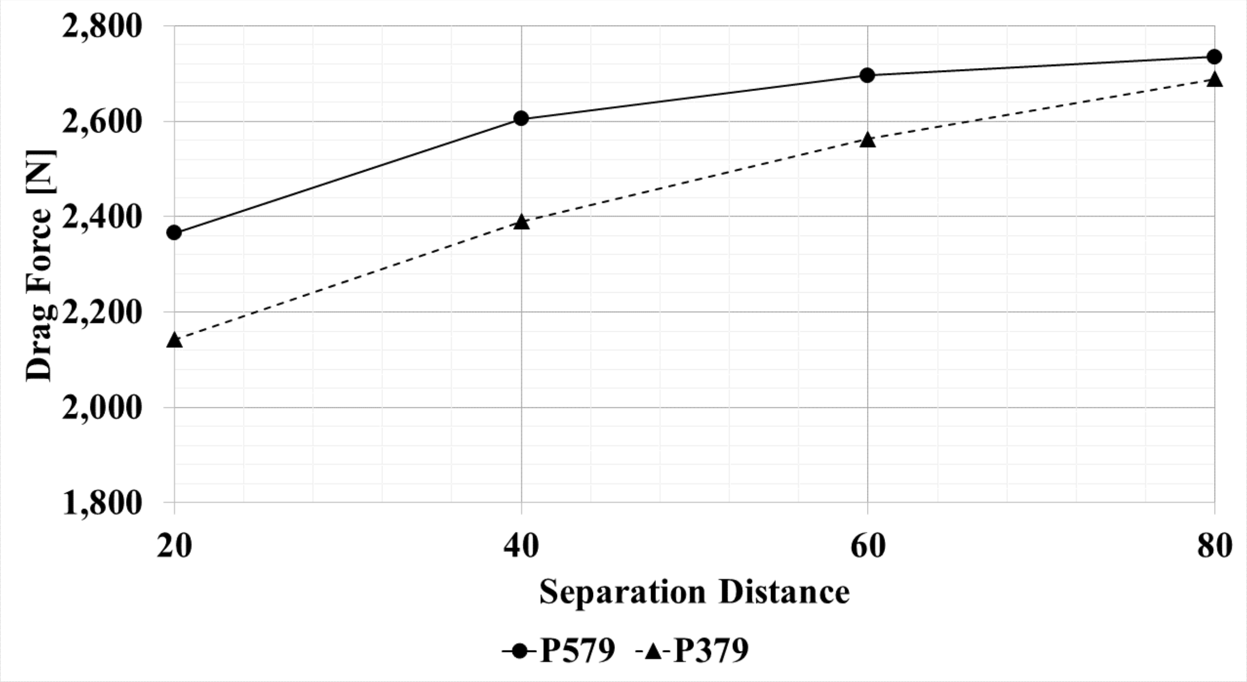

Figure 5.31: P579 / P379 Drag

It can be seen that the Peterbilt 379 experiences a very large reduction in drag. In fact, the following P379 has less drag than the Peterbilt 579 whereas the single P379 saw nearly double drag force. The exact percentage reduction for each vehicle from the corresponding single body was calculated and is shown below in Table 5.4.

Table 5.4: Peterbilt 379 drag

Separation Distance	**Percent of Corresponding Single Vehicle Drag**	
	P579	P379
20 ft	85.8%	45.7%
40 ft	94.5%	51.0%
60 ft	97.8%	54.7%
80 ft	99.2%	57.4%

It is clear from Table 5.4 that the Peterbilt 379 experiences reductions in drag, even at 80 ft. Because aerodynamic drag accounts for such a large portion of fuel consumption, it would be extremely beneficial for a P379 to platoon with other heavy vehicles as the follower, but less advantageous if the P379 was the lead vehicle.

As with the other multi-vehicle simulations, the velocity profile and pressure distribution was plotted for multiple distances to gain a qualitative understanding of the flow field. The resulting plots are shown below in Fig. 5.32 for the 40 ft case.

(a) Velocity Magnitude

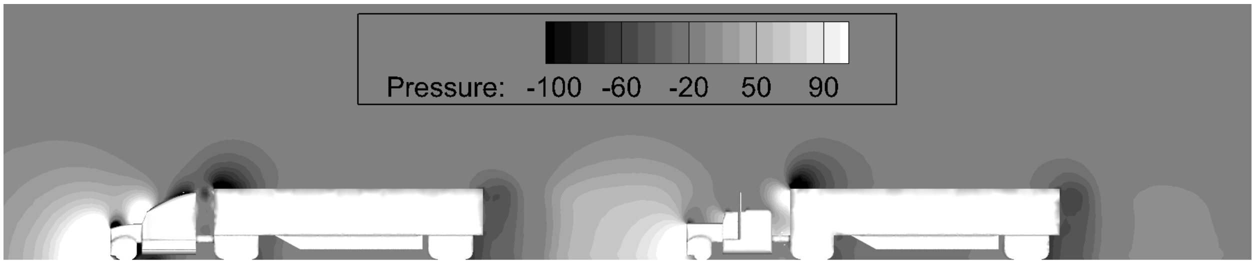

(b) Pressure field

Figure 5.32: P579 / P379 profiles – 40 ft separation

Two observations can be made immediately upon review of Fig. 5.32; firstly, the trailer rear on each vehicle is very similar in both wake structure and pressure disturbance. Secondly, the high drag areas on the Peterbilt 379, the hood and the trailer front, are still the areas that generate the most drag, though the magnitude is much lower than in the single vehicle case. These behaviors are expected, the slipstream behind the front vehicle does not fundamentally change drag profile of the following body but rather greatly reduces the magnitude of the drag generated via a reduced mean flow velocity.

5.4.2 Mercedes-Benz ACTROS

After completion of the Peterbilt 379 simulations, the Peterbilt 579–Mercedes-Benz ACTROS model shown in Fig. 5.33 was developed. The distance shown by Fig. 5.33 is a separation of 20 ft. The same separation distances were used in the MBA simulations as in the P379 simulations: 20, 40, 60, and 80 ft.

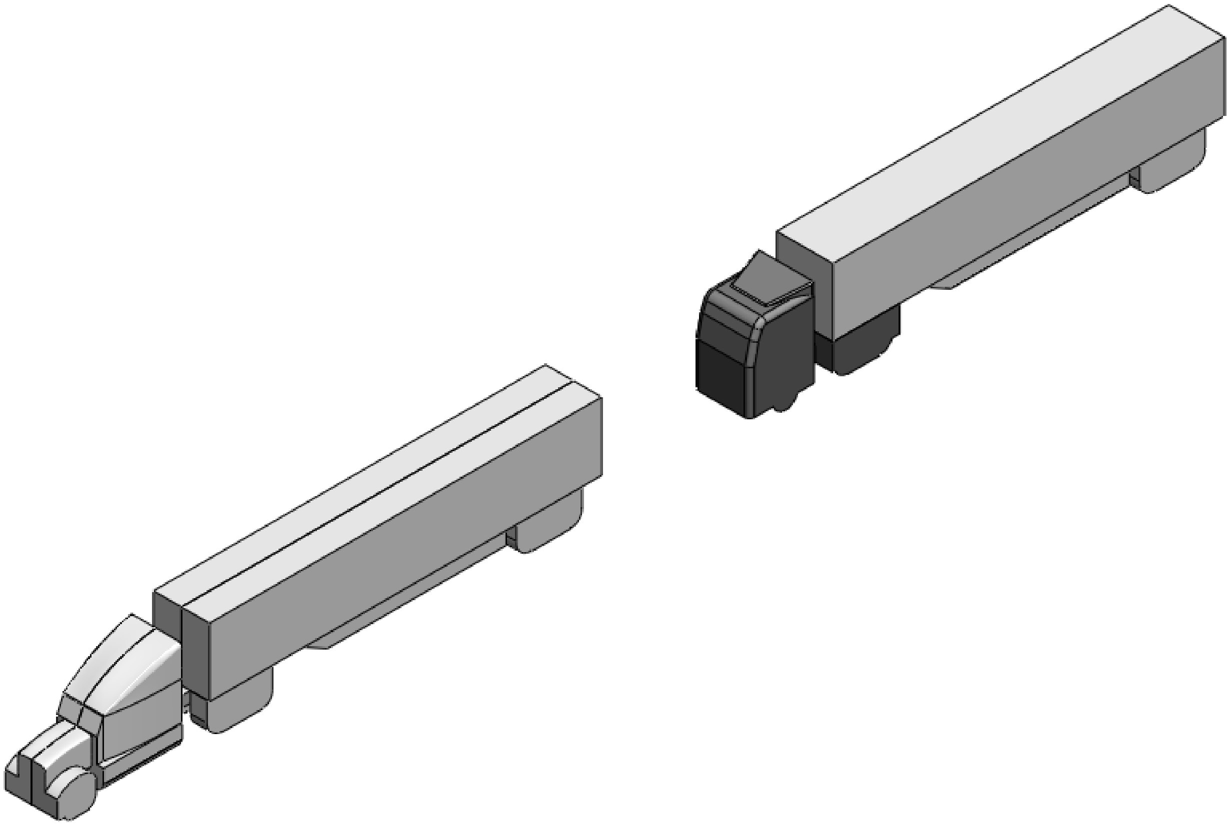

Figure 5.33: P579 / MBA CAD model – 20 ft separation

Again, using a nondimensionalized force would misrepresent the simulation results, therefore the data presented below in Fig. 5.34 is in terms of Newtons.

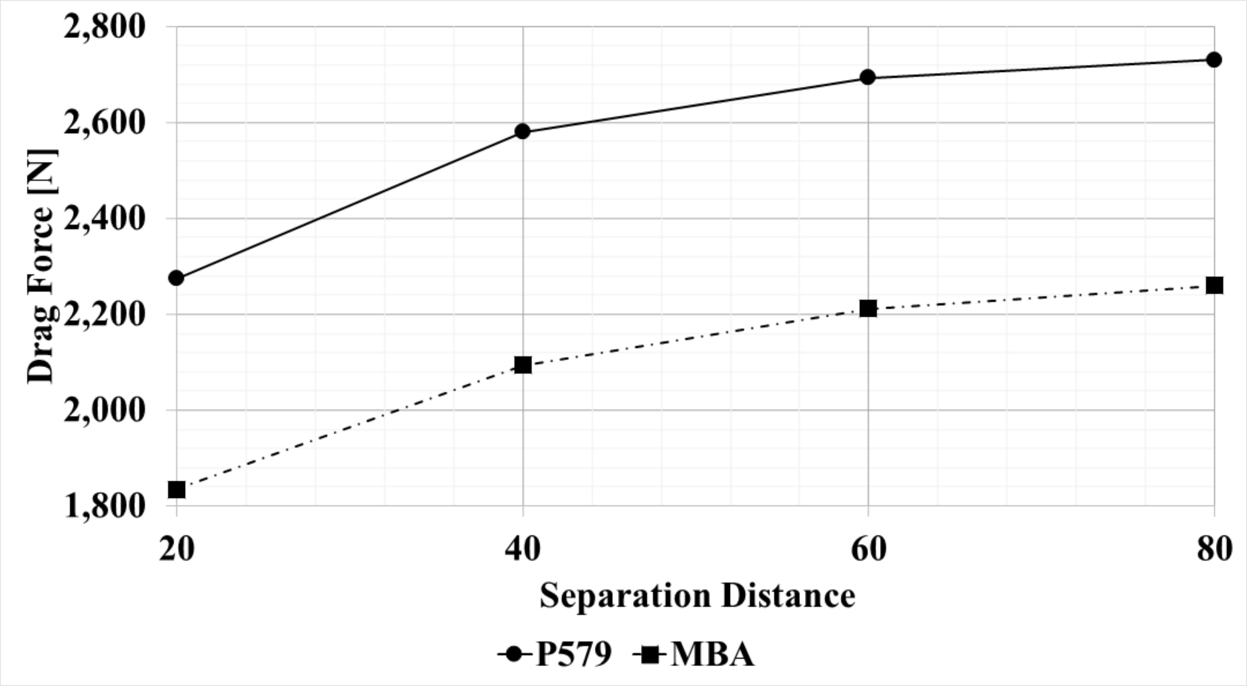

Figure 5.34: P579 / MBA Drag

As with the Peterbilt 379 simulations, a sharp reduction is shown in drag for the rear vehicle, the MBA. The drag force, which was originally close to the Peterbilt 579, has fallen well below the single vehicle simulation drag. The percentage reduction from the single MBA drag force is shown below in Table 5.5 along with the percentage reduction predicted for the lead vehicle, the P579.

Table 5.5: MBA drag

Separation Distance	**Percent of Corresponding Single Vehicle Drag**	
	P579	MBA
20 ft	82.5%	68.1%
40 ft	93.6%	77.7%
60 ft	97.7%	82.1%
80 ft	99.1%	83.9%

Combining the information presented by Fig. 5.33 and Table 5.5, it is clear the Mercedes-Benz ACTROS also sees a significant drag reduction from the single vehicle case, though not as much as the P379 geometry. This comparison is further expounded upon in Sec. 5.4.3.

Again, a qualitative understanding of the flow is never amiss, thus the state variables were plotted in the region surrounding the vehicles. The profiles shown in Fig. 5.35 are for the 40 ft separation case.

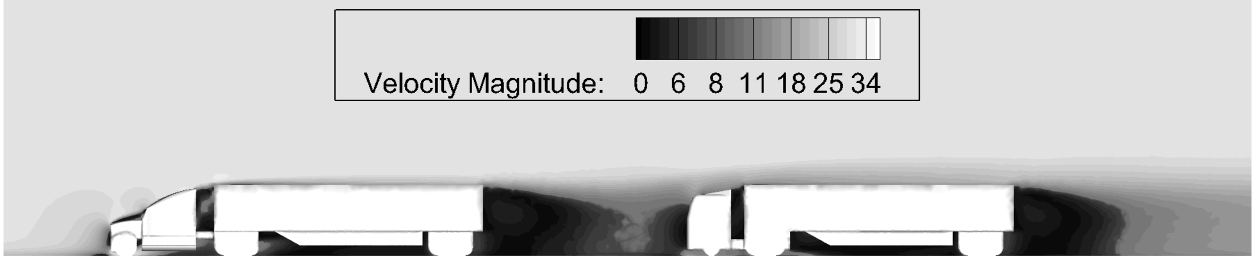

(a) Velocity Magnitude

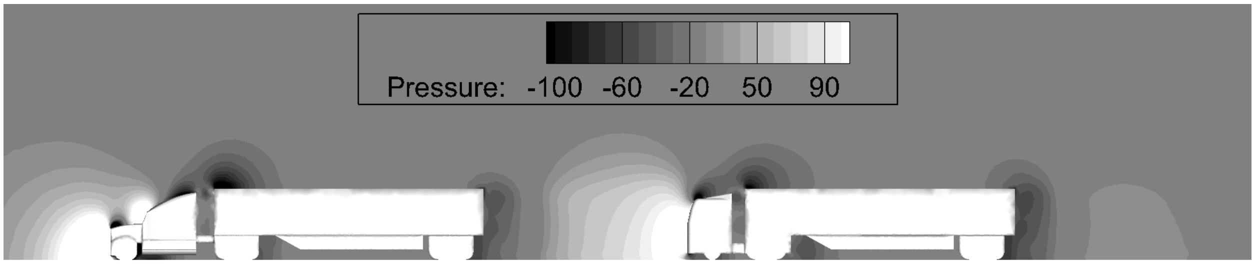

(b) Pressure field

Figure 5.35: P579 / MBA profiles – 40 ft separation

Trends close to those of the Peterbilt 379 are seen in Fig. 5.35. The tractors experience the same pressure distribution as the single vehicle case at a lower magnitude and the pressure field around the rear trailer is very similar. A key difference is the amount of wake interference the lead vehicle sees. The MBA appears to interfere more strongly than the Peterbilt 379, despite having a less invasive geometry.

5.4.3 Geometry Variation Result Comparison

Having now completed 4 simulation distances for 3 different multiple geometry cases, it was possible to begin to contrast and compare the results.

Drag forces in this section are presented as percentages of the single vehicle drag experienced for the corresponding geometry. For example: in the 20 ft P579 / MBA simulation, the frontal Peterbilt 579 drag is normalized by the single P579 drag and the rear vehicle, the MBA, is normalized by the single Mercedes-Benz ACTROS force. Drag is displayed in this manner to generate a relative basis to understand savings across vehicles.

Firstly, the 20 ft and 80 ft separation simulations were compared in a qualitative manner via the velocity and pressure distributions. Figure 5.36 depicts the velocity field between each vehicle and Fig. 5.37 illustrates the pressure profile. Because the inter-vehicle region was the primary region of difference, it is shown for each case as opposed to the entire near-vehicle domain.

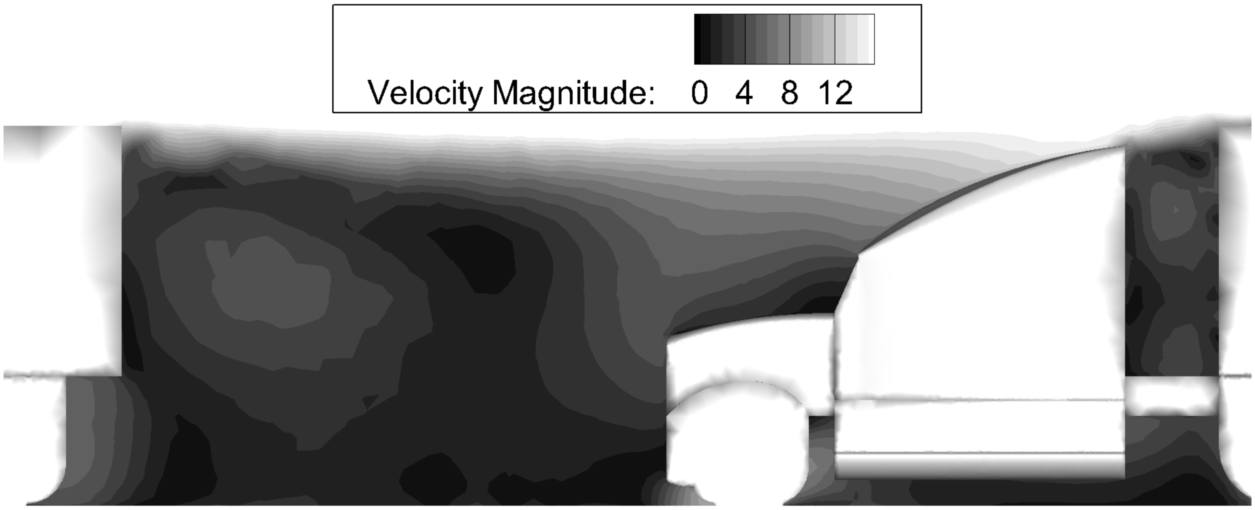

(a) Peterbilt 579

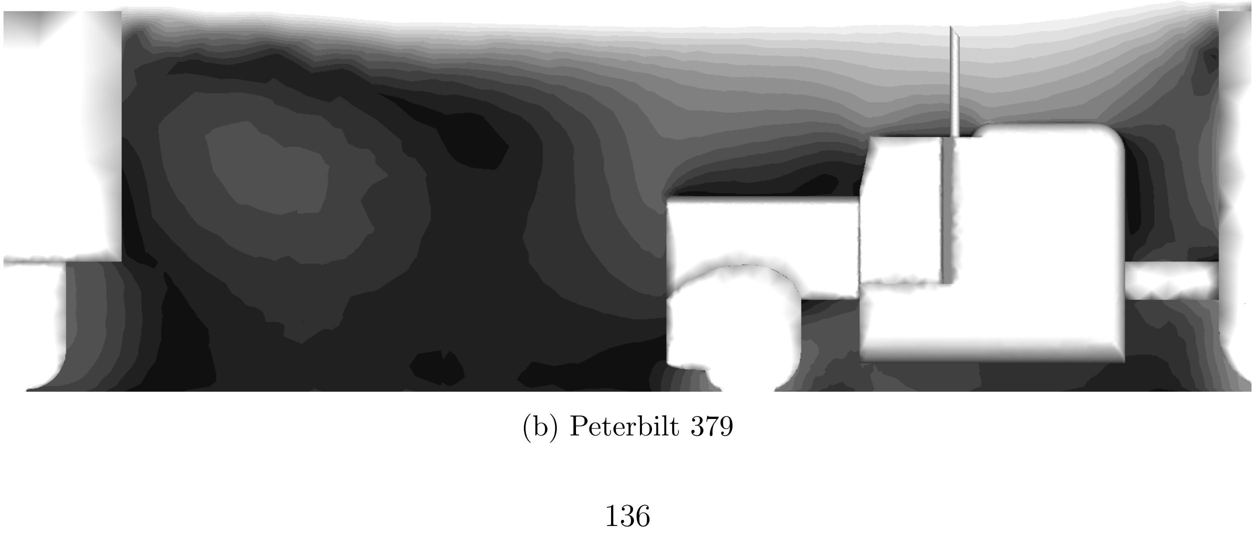

(b) Peterbilt 379

(c) Mercedes-Benz ACTROS

Figure 5.36: Velocity profiles – 20 ft separation

The first detail of note in the figure above is the wake formation behind Vehicle 1. Between Fig. 5.37a and Fig. 5.37b the wake is nearly indistinguishable. The wake in Fig. 5.37c, however, is very dissimilar. The flat geometry of the MBA causes a much larger propagation upstream than the geometric profiles of either the P579 or P379, resulting in a lower velocity and smaller wake. This larger footprint appears to translate to reduced drag on the lead vehicle.

Another consequence of geometry can be seen by comparing Fig. 5.37a and Fig. 5.37c to Fig. 5.37b. While the Peterbilt 579 and the Mercedes-Benz ACTROS channel most of the flow over the trailer, the flow over the Peterbilt 379 continues to coalesce until it encounters the trailer front. This is an adverse effect for the P379 as the flow continues to accelerate until it encounters the orthogonal solid wall of the trailer, likely translating into a relative increase in drag. (though still reduced from the single vehicle value)

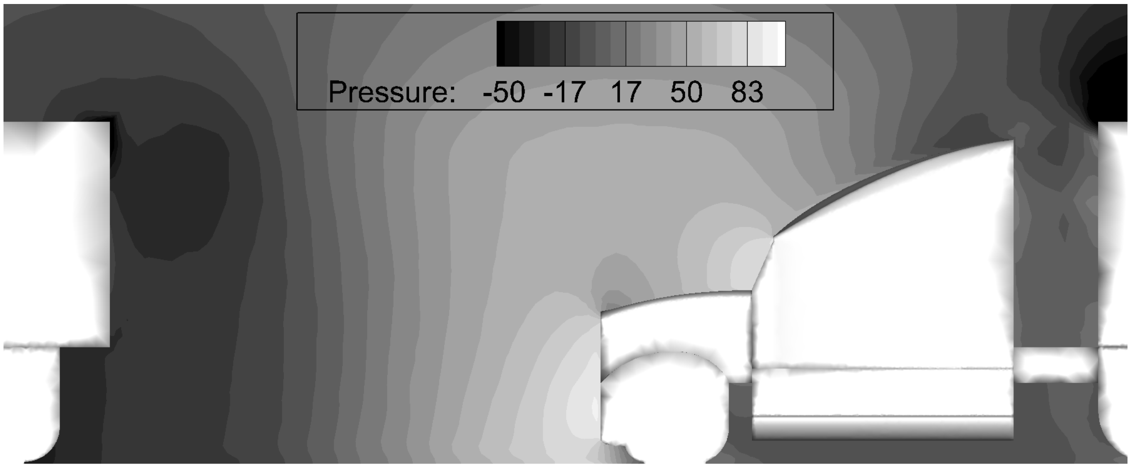

(a) Peterbilt 579

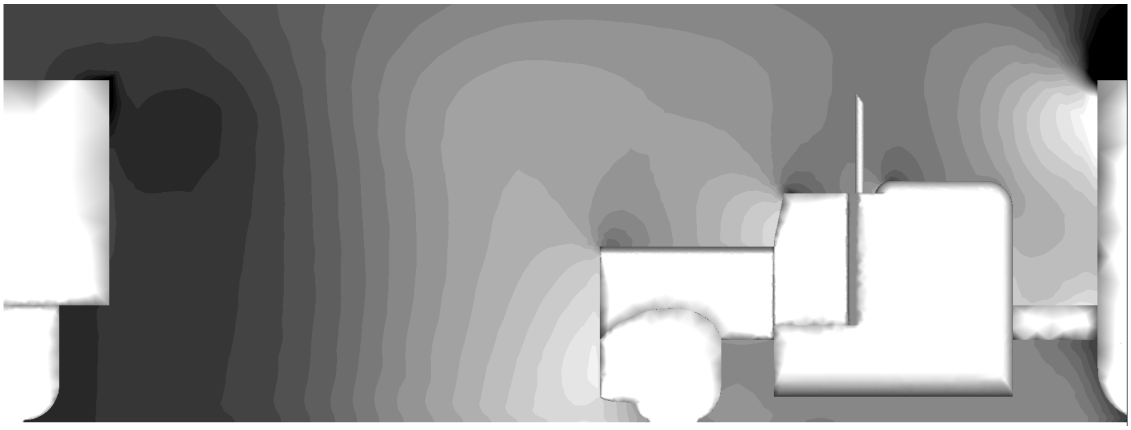

(b) Peterbilt 379

(c) Mercedes-Benz ACTROS

Figure 5.37: Pressure profiles – 20 ft separation

Examining Fig. 5.37b strengthens the point made above: the pressure force on the upper trailer is the largest by a noticeable amount. This stresses how much drag reduction the over-cab hood provides for the P579.

The consequence of the large upstream perturbation is also seen in Fig. 5.37c, a large high pressure region is formed immediately in front of the vehicle tractor. This makes the MBA vehicle very sensitive to changes in mean flow because the pressure drag is highly concentrated at the front of the tractor.

After the 20 ft simulation had been examined, identical analysis was performed for the 80 ft spacing case. The velocity magnitudes for each case are shown in Fig. 5.38 and the pressure in Fig. 5.39.

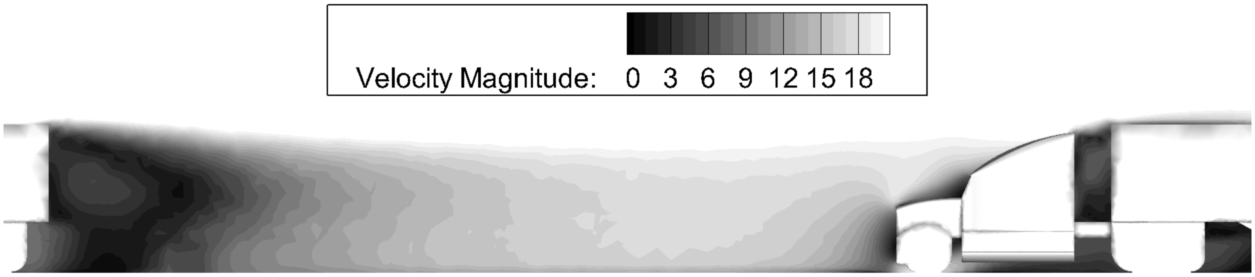

(a) Peterbilt 579

(b) Peterbilt 379

(c) Mercedes-Benz ACTROS

Figure 5.38: Velocity profiles – 80 ft separation

It can be seen from the profiles above that there is very little wake interaction at 80 ft as all vehicles are well within the slipstream region of the lead vehicle disturbance. This more closely simulates a reduced freestream velocity because the flow is more directed. Thus the 80 ft cases provide a better indication of the velocity profile around the Vehicle 2 tractor in all cases allowing a visual comparison of flow.

As with the 20 ft simulation, Fig. 5.38a and Fig. 5.38b have very similar tractor velocity profiles due to the frontal tractor similarities. The flow significantly changes, however, as one approaches the end of the tractor. Firstly, the profiles demonstrate that the rounded hood of the Peterbilt 579 assists in reduction of recirculation in front of the windshield region. Secondly, the presence of the modern aerodynamic hood on the P579 slopes the flow over the vehicle and greatly diminishes the trailer front drag, which was known from the single vehicle analysis.

Shown in Fig. 5.38c, the starkly different geometry of the MBA is a large obstacle for the flow. The consequence of the flat-nosed profile is a reduced freestream velocity upstream from the vehicle, significantly greater than the Peterbilt 579 or Peterbilt 379 disturbance in both distance and magnitude.

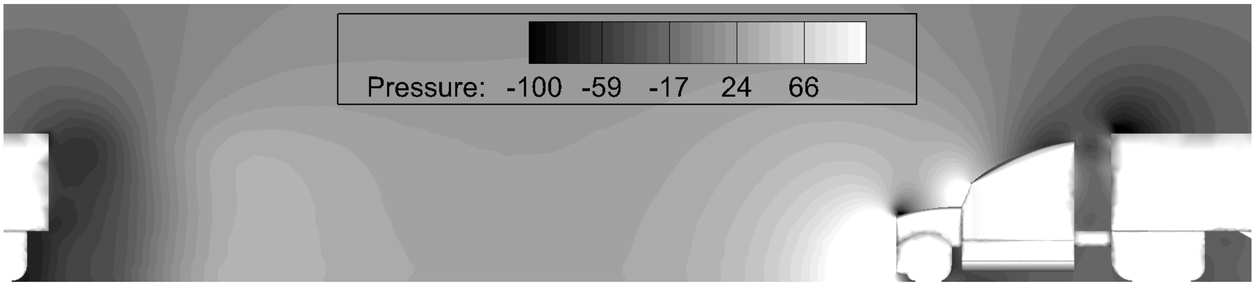

(a) Peterbilt 579

(b) Peterbilt 379

(c) Mercedes-Benz ACTROS

Figure 5.39: Pressure profiles – 80 ft separation

Included for completeness, the pressure plots shown in Fig. 5.39 show primarily what is expected: a virtually identically pressure distribution on the trailer rear of Vehicle 1 and sharp regions of increase on the transverse faces of Vehicle 2, depending on the geometry of the model. The large pressure region on the trailer of the P379 in Fig. 5.39b is much more pronounced in the 80 ft simulation because the mean flow encountered is larger velocity than in the 20 ft case.

After conclusions had been drawn about the vehicle interactions on a qualitative level, the drag coefficient for the lead vehicle was charted against tractor-trailer spacing as a percentage of single P579 drag. The results are shown below in Fig. 5.40.

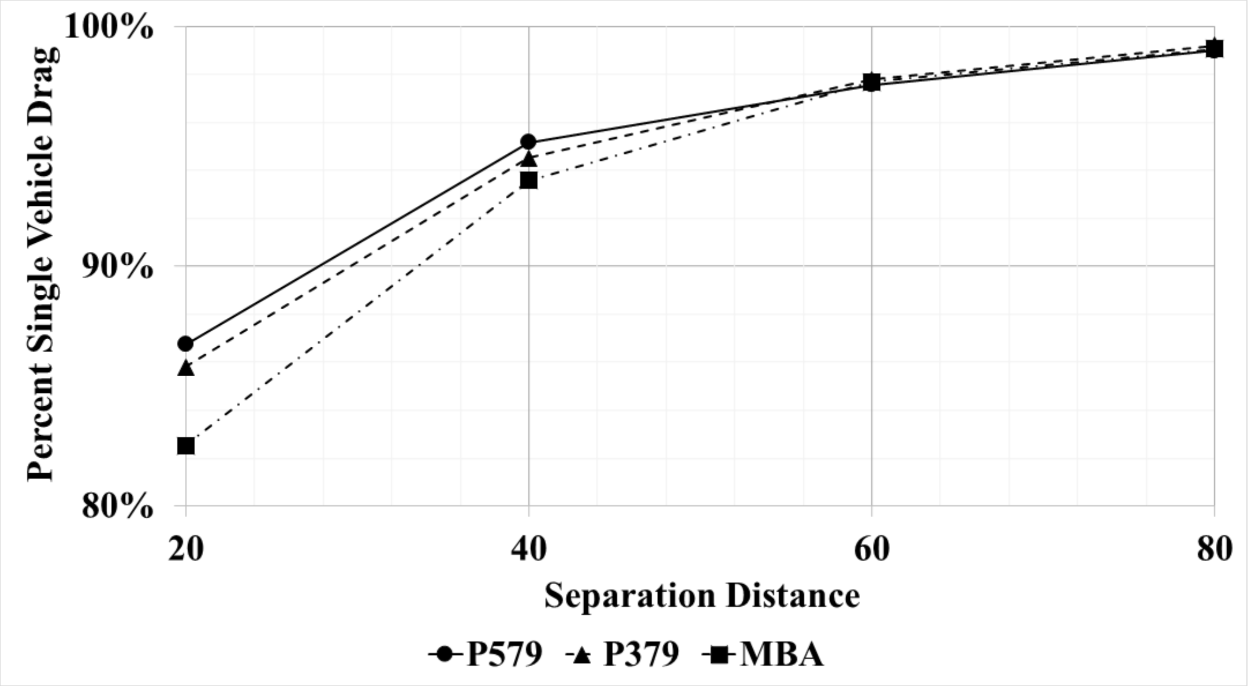

Figure 5.40: Lead vehicle drag reduction for varying follow vehicle geometry

Examining Fig. 5.40 provides understanding of the effects of geometry on the wake. Beyond 60 ft, all followers have the same effect on the lead vehicle: little. As Vehicle 2 approaches Vehicle 1, an interesting trend appears. Though the drag difference between the P579 and P379 follower is too insignificant to draw a strong conclusion, the lead vehicle drag decreases noticeably in the MBA case.

This confirms the hypothesis that the larger upstream footprint of the MBA does indeed result in decreased drag for the lead vehicle. Though the geometry is less imposing, the aerodynamic signature is actually more intrusive, extending farther into the flow. This result is unintuitive and is the opposite of the speculation initially posed.

Finally, the drag reduction for each follow vehicle was normalized by the corresponding single vehicle drag and graphed in Fig. 5.41.

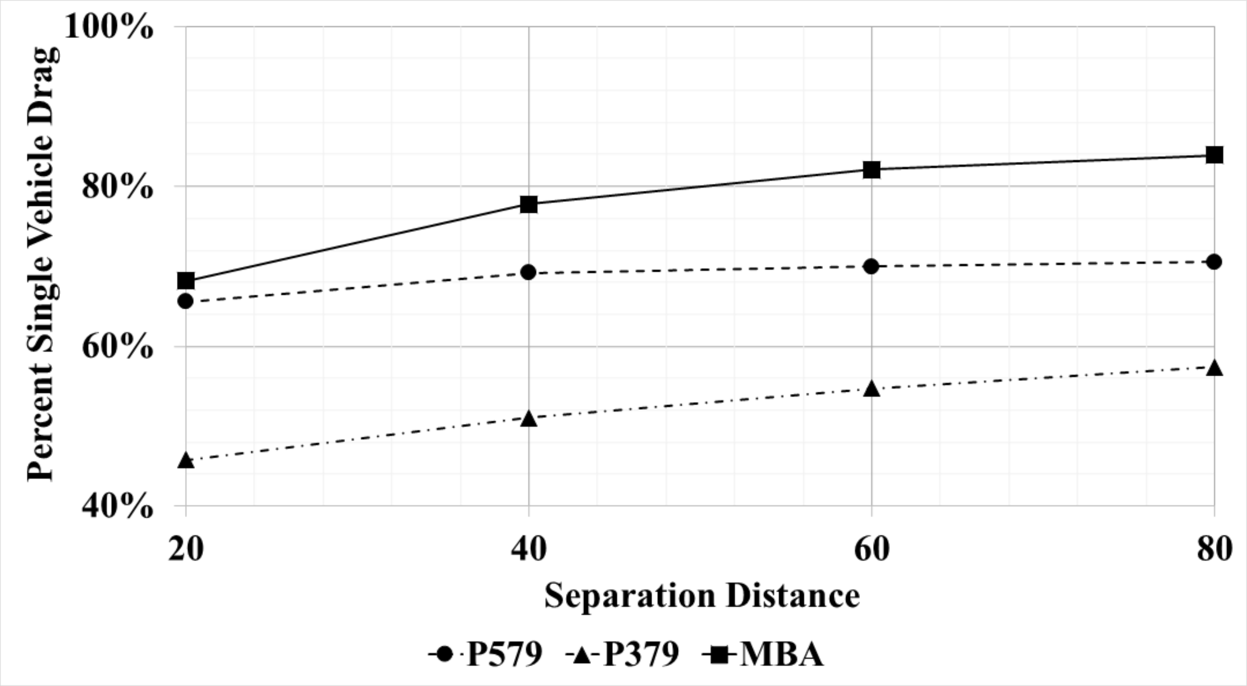

Figure 5.41: Rear vehicle drag reduction for varying follow vehicle geometry

The results shown in Fig. 5.41 are of the most interest and provide the most insight into the geometry-drag correlation in regards to platooning. Comparing the more modern geometries first, the Peterbilt 579 experienced a more constant and greater benefit than the MBA. While it still saw significant drag savings, the Mercedes-Benz ACTROS saw the least benefit of any geometry. However, as the 10 ft simulation discussed in Sec. 5.2.1 shows, the drag decrease becomes much more pronounced at closer distances. This nonlinear trend, where the tractor of Vehicle 2 is fully immersed in the wake of Vehicle 1, suggests that the MBA, which is highly distance dependent, would see even greater savings at closer spacings and likely see less drag the P579.

The reason for the quick taper of the ACTROS vehicle can be seen by comparing Fig. 5.39c and Fig. 5.37c. As the distance increases the mean flow velocity grow, which in turn very rapidly increases pressure in the concentrated stagnation region at the tractor nose.

Though the MBA sees a drag reduction at every distance, unlike the Ahmed body, comparisons can still be drawn between them due to their very bluff designs. Despite having comparable single body drag, the Mercedes-Benz vehicle sees less benefit than its Peterbilt counterpart because of its blunt, flat-nose design except at extremely close distances. This was also seen with the Ahmed body where drag was reduced significantly at very small separations.

The least aerodynamic vehicle, the Peterbilt 379, receives by far the most benefit. Even at 80 ft, where the ACTROS is over 80% of original drag, the P379 is still less than 60% of the normalization value. The fact that the P379 sees the most benefit highlights, once again, the nonlinearity of the Navier-Stokes equations. Because aerodynamic force is a function of the square of velocity, even a small change can reduce the magnitude of a large force by a significant amount, as can be seen in Fig. 5.41 and gathered from the profiles presented in Fig. 5.37b and Fig. 5.39b.

These results indicate that it is desirable, if possible, for the most aerodynamic vehicle to lead the platoon and the least aerodynamic to be the trailing vehicle as it will experience the most benefit. At sufficiently close distances, this will cause both vehicles to experience reduced drag and generate the most overall savings.

Chapter 6

Conclusion

This final chapter summarizes the research performed herein and restates important conclusions reached. Applications of this research to real world environments, along with non-aerodynamic considerations are also discussed. Finally, recommended future work and branches of continuation are discussed.

6.1 Model Validation

The first task performed was model validation. This was successfully accomplished using the simplified car body, known as the Ahmed body. which is a generic, well-tested bluff body,

The simulation-predicted drag coefficient was compared to wind tunnel data generated by Ahmed [13] and was found to be accurate to within 5% of the wind tunnel data for the baseline model. Furthermore, the simulation was found to exhibit convergent behavior to the wind tunnel value when the number of elements in the mesh was increased.

The multi-body simulations for the Ahmed body were also compared to wind tunnel data published by Pagliarella [18] for validation purposes. Because the model used by Pagliarella had a rear slant of twenty-five degrees, a direct quantitative comparison could not be made. The trends seen in [18], however, were captured extremely well, with only a linear offset bewtween the two solutions at close distances.

6.2 Two Vehicle Simulation

Once the simulation model had been validated, a single vehicle model was developed and tested to generate a baseline drag to compare against multi-vehicle simulations. At this point, a second vehicle was added and the simulation was ran at multiple distances to examine the drag-vehicle spacing relationship for tractor-trailer vehicles.

Upon analysis of the simulation data it was found that three distinct regions exist when considering drag force variation: a wake region, a slipstream region, and a freestream region. The wake region was marked by Vehicle 1 wake interference from Vehicle 2 and consisted of two sub-regions. The first, the inner wake, saw rapidly increasing drag forces on both vehicles as they separated from each other. Any separation less than 40 ft was considered to be in this region. The outer wake region was between 40 and 70 ft and saw a less pronounced decrease in drag. Vehicle 2 was approaching the asymptotic slipstream value and saw little change, while Vehicle 1 was inching towards the single body drag coefficient. Beyond this region, Vehicle 1 saw no benefit.

The slipstream, the second region of interest, provided a near constant drag for Vehicle 2, which was between 65 and 75% of the single tractor-trailer value. This region existed between 70 ft and 350 ft. Vehicle 2 continued to see a reduced drag force until the end of the Vehicle 1 disturbance, at which point there is a sharp, rapid increase in force as the normalized drag approaches one. This region was termed the freestream region and is equivalent to simulating to independent vehicles.

During the simulation, it was discovered that the RKE turbulence model failed to predict accurate drag coefficients at distances beyond 350 ft, which coincides with the termination of the Vehicle 1 slipstream. This is because the RKE model poorly handles low turbulent kinetic energy (TKE) regions, that is it cannot properly dissipate turbulent energy. This results in the RKE model being unable to transition a turbulent flow to a laminar state. The DES model was required to capture this relaminarization and determine where Vehicle 2 stopped experiencing benefits.

An unexpected result that was revealed upon examination of the surfaces for each vehicle was an increase in trailer front pressure drag on Vehicle 2 as the gap between bodies was narrowed. Using Crocco's theorem, vorticity, and pressure gradient analysis, it was determined that this was a result of the decreased mean flow velocity and was indeed a valid result. In the end, however, this inverse proportionality between front trailer drag and vehicle distance was not enough to negate the immense benefits experienced by the tractor of Vehicle 2 and the overall result was reduced drag.

It can thus be concluded that when platooning, vehicles should strive to be as close as possible. In essence, it is highly desirable for the following body to be in the inner wake region of the lead body. This provides not only significant drag reduction for Vehicle 2, but also notable savings for Vehicle 1.

6.3 Three Vehicle Simulation

Once the two body simulations had been fully explored, a third identical vehicle was added to the geometry configuration and tested.

The most apparent conclusion was that the middle vehicle, Vehicle 2, experienced more benefit than Vehicle 3 at close distances. This is because Vehicle 2 receives benefits from both Vehicle 1 and 3, whereas the rearmost body only sees frontal drag reduction through reduced mean flow speed. This can be generalized by the statement that interior vehicles experience the most benefit and therefore larger platoons provide more overall savings on a per vehicle basis than smaller platoons.

The “region of influence” concept was also expounded upon. It was shown through use of homogeneous and heterogeneous distance configurations that each vehicle was nearly independent of vehicles beyond the immediately preceding and following bodies. In fact, as shown with the Ahmed simulation, the majority of the influence of a body does not extend past the closest portion of its neighbor vehicle, be it front or rear. These conclusions were especially true for upstream bodies, which was expected. Downstream regions saw slight variations due to upstream body spacing, but not enough to tangibly make a conclusive statement or warrant full investigation.

6.4 Multiple Geometry Simulation

Finally, the third body was removed and the second replaced with a varied geometry model. This new configuration was simulated at multiple distances to determine the effect of tractor geometry on overall platoon savings.

It was first observed that in the inner wake region, tractor geometry had a noticeable effect on lead body drag reduction. The blunt shape of the Mercedes-Benz ACTROS provided a larger upstream disturbance, contributing more to wake interference than either the P579 or the P379. It should be noted that though this effect on the lead body rear surface pressure was noticeable, it was drastically improved.

The rear body provided more insight into the effect of geometry on platoon drag. It was discovered that the Peterbilt 379, the model which experienced the most drag, saw the most benefit. The almost 60% force reduction of the P379 at 20 ft spacing was largely a result of a decrease in trailer front drag, the lower mean flow velocity resulted in much less force on what is essentially a solid lateral wall. The very large percent drag reduction seen by the P379 brought the actual force experienced down to levels similar to that of the Peterbilt 579, which saw the second most benefit and a gentle decrease in drag across the interval examined.

Finally, the MBA had the least percent savings of any model. This was a result of the flat-nose style which concentrated the stagnation region. This afforded more reduction at closer distances, but less near the end of the wake region. The decrease in drag continued to become exaggerated as the distance between vehicles narrowed, but the MBA never overtook the P579 in savings.

These conclusions lead to the determination that it is always the most beneficial to have the least aerodynamic vehicle be in a following position in order to experience the most drag and fuel savings.

6.5 Applications to Highway Environments

As discussed in the introduction to this work, the primary motivation for the drag reduction achieved through platooning is fuel savings. Because drag is the number one contributor to resistive force at highway speeds by a factor of 2, improving the aerodynamics of a vehicle generates the most fuel savings of any loss generating mechanism.

The drag savings offered by platooning have been shown to be significant, particularly at close following distances. These savings provide a large benefit to miles per gallon achieved by a vehicle, which decreases operating cost. Moreover, platooning is an inexpensive method that is guaranteed to generate immediate cost savings with implementation of the CACC system.

While close distances are ideal, the work performed herein showed that even at large distances, such as two or three body lengths, the follow vehicle still sees significant drag savings. This translates directly to improved fuel economy. A 30% reduction in drag at a following distance of 200 ft provides evidence that even at large spacings, long haul companies can benefit from platooning.

The recommendations and conclusions in the research were made from a purely aerodynamic perspective. And though these methods will provide the most drag benefit, there are other considerations that must be made when determined the appropriate platoon configuration. For example, a fleet owner would likely not be willing to platoon with a competitor if the owner's vehicle was required to be the lead vehicle. This is because though there is a net savings, the competitor vehicle sees the most reduction and fuel savings.

When considering large platoons, highway congestion concerns arise. Though it was found that groups of several vehicles receive the most benefit, this may not be feasible from a traffic pattern perspective as it may impede passenger vehicles or obstruct highway exits. Also, the conclusion to have the most aerodynamic vehicle in the follow position may give rise to safety issues. This is because the least aerodynamic vehicle is often the oldest, which may indicate the least effective braking systems. If the lead vehicle can brake more quickly than the follow, a collision is more likely to occur. These considerations and many more must all be reviewed when deliberated which configuration provides not only optimal fuel economy, but also maximum driver and roadway safety.

6.6 Future Work

For future work this author proposes four primary areas of exploration: comparison to experimental data, full transition to the DES model, investigation of the slipstream, and simulation of platoons larger than three vehicles. The first topic, comparison to experimental data, is the most important recommendation because it will provide validation for the tractor-trailer models considered throughout this study. This will allow the results predicted to be used with a measure of confidence that would otherwise be unwarranted.

Secondly, a full transition to the Detached Eddy Simulation model is recommended for multiple reasons. Foremost, a RANS model is incapable of capturing relaminarization and thus a model that is based on LES is required to simulate large separation distances. Another strong reason for transition to the DES model is the development of time averaged profiles, which will reveal any transient structures in the domain.

The third area of research recommended is examination of the slipstream region and the slipstream-freestream transition. Key questions that arise are the reason for near constant drag in the slipstream and the rapid transition that occurs near the termination of the wake. This result is perhaps the most unexpected, as it was initially hypothesized that the drag would increase asymptotically until it reached the single vehicle drag, instead of plateauing in the slipstream region.

The final issue recommended for additional discourse is the simulation of platoons larger than the ones examined herein. Most notably, a four vehicle platoon would likely to be sufficient to elaborate on the interactions of nonadjacent vehicles and confirm or deny the interior vehicle suggests posited here.

Bibliography

[1] SelectUSA, “The Logistics and Transportation Industry in the United States.” [Online]. Available: http://selectusa.commerce.gov/industry-snapshots/logistics-and-transportation-industry-united-states

[2] Environmental Protection Agency, “Regulatory Announcement: Paving the Way Toward Cleaner, More Efficient Trucks.” [Online]. Available: http://www.epa.gov/otaq/climate/documents/420f11032.pdf

[3] Owner-Operator Independent Drivers Association, “Figuring Cost Per Mile, Owner-Operator Independent Drivers Association,” 2015. [Online]. Available: http://www.ooida.com/EducationTools/Tools/costpermile.asp

[4] Federal Motor Carrier Safety Administration, “FMCSA Regulations,” 2015. [Online]. Available: http://www.fmcsa.dot.gov/

[5] Oak Ridge National Laboratory, “2013 Vehicle Technologies Report,” p. Chapter 3, 2013. [Online]. Available: http://cta.ornl.gov/vtmarketreport/pdf/chapter3_heavy_trucks.pdf

[6] Trucking Freight and Logistics News, “Top 100 For-hire Carriers,” 2014. [Online]. Available: http://www.ttnews.com/top100/for-hire/

[7] ATDyanmics, “Aerodynamics 101,” 2015. [Online]. Available: http://www.atdynamics.com/resources/aerodynamics-101/

[8] Aerotails LTD., “Aerotails Fuel Saving Products.” [Online]. Available: http://www.aerotails.com/

[9] D. V. Mcgehee, E. N. Mazzae, and G. H. S. Baldwin, “Driver reaction time in crash avoidance research: validation of a driving simulator study on a test track,” 1998.

[10] U.S. Department of Transportation, “Title 23 Code of Federal Regulations Part 658.17,” pp. 308–309, 2011.

[11] D. Bevly, “Heavy Truck Cooperative Adaptive Cruise Control: Evaluation, Testing, and Stakeholder Engagement for Near Term Deployment,” 2013.

[12] Federal Highway Administration, “Federal Highway Administration No . DTFH61-13-R-00011 Exploratory Advanced Research Program ,” 2013.

[13] S. Ahmed, G. Ramm, and G. Faltin, "Some Salient Features Of The Time-Averaged Ground Vehicle Wake," Tech. Rep., Feb. 1984. [Online]. Available: http://www.sae.org/technical/papers/840300

[14] P. Hong, B. Marcu, F. Browand, and A. Tucker, "SAE TECHNICAL Drag Forces Experienced by Two , Full-Scale Vehicles at Close Spacing," no. 724, 1998.

[15] C. Bonnet and H. Fritz, "Fuel Consumption Reduction in a Platoon : Experimental Results with Two Electronically Coupled Trucks at Close Spacing," no. 724, 2014.

[16] P. Adarsh, A. G. Cherian, and D. R. Kumar, "NUMERICAL INVESTIGATION OF DRAG ON A TRAILING," no. 2010, pp. 81–86, 2014.

[17] A. L. Chen, O. Savas, and K. Hedrick, "Transient Vehicle Aerodynamics in Four-Car Platoons," 1997.

[18] R. M. Pagliarella, S. Watkins, and A. Tempia, "Aerodynamic Performance of Vehicles in Platoons : The Influence of Backlight Angles Reprinted From : Vehicle Aerodynamics 2007," vol. 2007, no. 724, 2014.

[19] Dassault Systemes, "SOLIDWORKS." [Online]. Available: http://www.solidworks.com/

[20] ANSYS Inc, "FLUENT Theory Guide." [Online]. Available: http://www.arc.vt.edu/ansys_help/flu_th/flu_th.html

[21] ——, "ANSYS Fluent." [Online]. Available: http://www.ansys.com/Products/Simulation+Technology/Fluid+Dynamics/Fluid+Dynamics+Products/ANSYS+Fluent

[22] ——, "ANSYS Meshing Software." [Online]. Available: http://www.ansys.com/Products/Workflow+Technology/ANSYS+Workbench+Platform/ANSYS+Meshing

[23] R. J. LeVeque, Finite Volume Methods for Hyperbolic Problems. Cambridge University Press, 2002. [Online]. Available: http://books.google.com/books/about/Finite_Volume_Methods_for_Hyperbolic_Pro.html?id=QazcnD7GUoUC\&pgis=1

[24] R. D. Falgout, "An Introduction to Algebraic Multigrid," 2006.

[25] W. P. Jones and B. E. Launder, "The Prediction of Laminatization with a Two-Equation Model of Turbulence," Journal of Heat and Mass Transfer, vol. 15, pp. 301–314, 1972.

[26] J. Boussinesq, "Essai sur la théorie des eaux courantes," in Mémoires présentés par divers savants à l'Académie des Sciences, 1877.

[27] B. Launder and D. Spalding, "The numerical computation of turbulent flows," Computer Methods in Applied Mechanics and Engineering, vol. 3, no. 2, pp. 269–289, Mar. 1974. [Online]. Available: http://www.researchgate.net/publication/222171646_The_numerical_computation_of_turbulent_flows

[28] S. Kim and D. Choudhury, "A near-wall treatment using wall functions sensitized to pressure gradient," Separated and complex flows- 1995, 1995. [Online]. Available: https://scholar.google.com/scholar?cluster=18277189235158102914\&hl=en\&oi=scholarr\#0

[29] J. SMAGORINSKY, "GENERAL CIRCULATION EXPERIMENTS WITH THE PRIMITIVE EQUATIONS," Monthly Weather Review, vol. 91, no. 3, pp. 99–164, Mar. 1963. [Online]. Available: http://journals.ametsoc.org/doi/abs/10.1175/1520-0493(1963)091⟨0099:GCEWTP⟩2.3.CO;2

[30] A. Leonard, Turbulent Diffusion in Environmental Pollution, ser. Advances in Geophysics. Elsevier, 1975, vol. 18. [Online]. Available: http://www.sciencedirect.com/science/article/pii/S0065268708604641

[31] I. B. Celik, "Introductory Turbulence Modeling," no. December, 1999.

[32] P. R. Spalart, ""Comments on the feasibility of LES for wing and on a hybrid RANS/LES approach," in Proceedings of the First AFOSR International Conference on DNS/LES, 1997.

[33] C. Hinterberger, M. García-Villalba, and W. Rodi, "Large Eddy Simulation of flow around the Ahmed body," in Lecture Notes in Applied and Computational Mechanics / The Aerodynamics of Heavy Vehicles: Trucks, Buses, and Trains, 2004.

[34] SharcNET, "Skewness Lecture." [Online]. Available: https://www.sharcnet.ca/Software/Fluent14/help/wb_msh/msh_skewness.html

[35] M. Lanfrit, "Best practice guidelines for handling Automotive External Aerodynamics with FLUENT," vol. 2, pp. 1–14, 2005.

[36] M. Vallero, "DETACHED-EDDY SIMULATION OVER A REFERENCE AHMED CAR MODEL."

[37] S. Kapadia, S. Roy, and K. Wurtzler, "AIAA-2003-0857 Detached Eddy Simulation Over a Reference Ahmed Car Model 41st Aerospace Sciences Meeting and Exhibit," no. January, 2003.

[38] N. Luminari, "PRACE Summer of High Performance Computing Student Project," 2015. [Online]. Available: https://summerofhpc.prace-ri.eu/project-reports-2014-nicola/

[39] Peterbilt, "Peterbilt Motors Company Model 579 Picture." [Online]. Available: http://www.peterbilt.com/products/on-highway/579/

[40] ——, "2001 Peterbilt 379 Picture." [Online]. Available: http://www.wallpaperup.com/228490/2001_Peterbilt_379.html

[41] Mercedes-Benz, "Mercedes-Benz ACTROS Picture." [Online]. Available: http://mercedes-benz-blog.blogspot.com/2011/07/new-mercedes-benz-actros-exterior-and.html

[42] GrabCAD, "GrabCAD." [Online]. Available: http://grabcad.com/

[43] B. Wasistho and K. D. Squires, "Prediction of turbulent separation over a backward-facing smooth ramp," Journal of Turbulence, vol. 6, p. N1, 2005.

[44] J. Jiang and X. Wang, "Validation of Large Eddy Simulation in a Relaminarizing Boundary Layer Flow," vol. 4, no. March, pp. 11–19, 2012.

[45] A. H. Shapiro, "Film Notes for Vorticity," pp. 1–12, 1969.